Simulations of Steady Streaming Flows and the Time-Averaged Motion of Inertial Particles

Tyler Andrew House

A dissertation submitted in partial fulfillment of the
requirements for the degree of

Doctor of Philosophy

University of Washington
2013

Reading Committee:
Daniel T. Schwartz
Danilo C. Pozzo
Stuart B. Adler

Program Authorized to Offer Degree:
Department of Chemical Engineering

Abstract

Simulations of Steady Streaming Flows and the Time-Averaged Motion of Inertial Particles

Tyler Andrew House

Chair of the Supervisory Committee:
Chair and Boeing-Sutter Professor Daniel T. Schwartz
Department of Chemical Engineering

Applications of microfluidic systems often involve microparticle or cell trapping. Hydrodynamic tweezers are an emerging technology that utilizes an oscillating primary flow to induce microscale steady streaming eddy flows in the vicinity of engineered obstructions. Particles with sufficient inertia, as described by the particle Stokes number (St), are collected near the center of eddies, while particles with negligible inertia tend to follow the fluid motion. Device fabrication and testing has generally led our understanding of trapping physics in hydrodynamic tweezers. Here, we describe a major advance in our understanding of the physics of particle trapping in these devices. We explore the weak inertia regime ($St \ll 1$) for particle motion using the well-known Maxey-Riley equation. To accelerate our computation of particle trajectories and fluid motion, we employ a leading-order analytical approximation for the time-periodic motion and superimpose a second-order steady motion. The time-averaged formalism of Stokes drift calculations (originally for non-inertial tracer particles) is extended to a weakly inertial particle to account for the relative velocity between fluid and particle. The resulting analytical formulation is combined with flow field simulations to reveal key physics and parameters that influence particle trapping. We demonstrate the versatility of our fast analytic-numeric flow field computations via a comparison with 12 device geometries, including circular, triangular, and rectangular wall protrusions, wall cavities, and mid-channel features, as well as high symmetry arrays of cylinders. Instantaneous particle trajectories show that inertial deviations scale as $(\eta - 1)\cdot St$ when tracking the fast motion over a single fluid oscillation period, where η is the ratio of fluid-to-particle densities. Time-averaged inertial Stokes drift analysis shows that leading order inertial effects in the mean motion of a particle scales as $\eta \cdot St$. The difference in scaling between the instantaneous and time-averaged motion means that a neutrally buoyant inertial particle ($\eta = 1$) follows the fast motion in a manner identical to a non-inertial tracer (to leading order) independent of St, whereas the time averaged velocity remains dependent on St. We use this analysis to predict trapping locations, i.e., the spatial locations where the mean particle velocity goes to zero. Our analytic-numeric approach has advanced the computational tools for hydrodynamic tweezers design by laying the groundwork needed to link device geometry and operation (flow frequency and amplitude) to the physics linked to trapping strength and particle shear stress.

ACKNOWLEDGMENTS

I'd like to thank my adviser, Professor Daniel T. Schwartz, who has guided and taught me so much, and my many colleagues, professors, and teachers who have helped me become worthy of the title "Doctor." I would also like to thank funding sources that made this research possible: an NSF "Bioresource-based Energy for Sustainable Societies" IGERT Fellowship (NSF grant DGE-0654252), an NSF Graduate Research Fellowship, an ARCS Foundation Fellowship provided by Anne & Michael Zubko of the Seattle Chapter, an NSF IGERT Early Bird Award in Nanotechnology, and the Boeing-Sutter Endowment. Fabrication was performed at the University of Washington Nanotechnology User Facility, a node on the National Nanotechnology Infrastructure Network.

Dedicated to my brother, Shane,

my parents, Steve and Dianne,

and all of my friends and family,

who supported and encouraged me with their best wishes.

TABLE OF CONTENTS

LIST OF FIGURES

CHAPTER 1 || INTRODUCTION

Microfluidic manipulation and trapping of cells and particles

Microfluidics, or the study of systems and devices that function on small volumes of fluids (μL or less), has long been researched as a promising method for synthesis, analysis, and manipulation of particles and fluids [1]–[6]. Microscale fluid dynamics tend to be dominated by viscous fluid forces rather than inertia, yielding low fluid Reynolds numbers and laminar flows [7], [8]. Advancements in basic physical understanding and modeling of microfluidic flows, ink-jet printing, microfabrication, and microelectromechanical systems (MEMS) technologies sped development of microfluidic functional units [1], [2] such as pumps [9], valves [10], sensors [11]–[13], and mixers [14], [15]. When these elements are combined into more complex systems, commonly known as miniaturized total chemical analysis (μTAS) or lab-on-a-chip systems, they can perform a wide range of familiar and useful lab processes and analyses [2]–[6], [16]–[18]. While research into microfluidic systems can now be thought of as an established area of scholarship, the scientific results and technological applications of systems based on microfluidics still has tremendous scope for greater impact [1].

One of the major opportunities for microfluidic systems are large arrays of sensors, high-throughput screening, and single-cell analysis applications that can improve health and tap into the attendant health care business opportunities; robust technology requires a continuous

advancement of underlying physics and biology [1], [16]. Many of these application areas require microfluidic particle and cell trapping and manipulation methods. The techniques and devices under development for trapping and manipulating can be broadly categorized by the forces they apply to particles: optical, magnetic, electrical, and hydrodynamic [18]–[23]. Optical tweezers, for instance, are a well-developed suite of techniques that use the spatial variation of focused laser light to push capture and manipulate particles and molecules with precision. The technique is well-suited for force measurements up to O(100 pN) and widely used to trap sub-micron particles [24]. For example, they are useful for confining biomolecules, sensing biophysical processes, and can be used as individual traps or in arrays [20], [24]–[26]. Magnetic trapping methods rely on the tailoring of magnetic fields to manipulate magnetic particles and magnetic fluids. For example, magnetic activated cell sorting (MACS) has been demonstrated for large scale particle separations but has remained limited as a wide-scale method due to the need to attach magnetic ligands to cells [19]. The use of electric fields to manipulate particles and cells can take several different forms. Electrophoresis of charged particles occurs in a dc electric field, and dielectrophoresis of neutral (but polarizable) particles in alternating and non-uniform electric fields can exert forces that are useful in cell manipulation devices [16], [20], [27], [28]. Manipulation of cells and particles by hydrodynamic and acoustic forces offer still more techniques, some depending entirely on design geometry, while others require minimal additional fabrication or external fields. More general detail about each method can be found in reviews by Nilsson, et al (2009) and Gao, et al. (2013) [19], [20]. Here we focus on the distinguishing physics that underpin the hydrodynamic trapping we call “hydrodynamic tweezers.”

Many hydrodynamic cell and particle manipulation methods are known: mechanical filtering and trapping, flow focusing, curved channel secondary flows, inertial particle migration, detached flow microvortices, dead end side channels, microwell arrays, among several others (see [8], [16], [19], [20], [29]). Hydrodynamic tweezers are an emerging particle trapping technology that we pioneered which utilize an oscillating primary flow to induce streaming flow around obstructions. The steady streaming flow structure consists of a fast oscillating flow that induces counter-rotating steady eddies around obstructions in the flow field. Several groups have observed streaming around bubbles trapped in microfluidic channels (often called cavitation microstreaming) [30]–[32]. With hydrodynamic tweezers, particles with sufficient inertia (whether buoyant or denser than surrounding fluid) are collected near the center of eddies, while particles with negligible inertia tend to follow the fluid motion and trace the flow streamlines [33]. Large arrays of tunable traps may be fabricated enabling both single cell trapping, and cell-cell interactions [34]. Experimental work has generally led our understanding of trapping physics in hydrodynamic tweezers [33]–[38]. Chen (2006) created a phenomenological model for trapping of inertial particles and compared simulation with experiments, but the physical origin of forces used was not clearly articulated [39].

The current lack of a self-consistent physics-based analysis of inertial particle motion in steady streaming flows, leaves open the possibility of new insights from a more thorough analysis. This thesis provides an overview of the history and theoretical analysis of steady streaming flows. A primer on the important differences between the Eulerian and Lagrangian frames of reference is given along with the approximation method to compute Stokes drift. A brief overview of inertial particle dynamics is also discussed in the context of the widely-used Maxey-Riley equation for the motion of a particle with small but finite inertia.

Basics of steady streaming flows

Steady streaming flows have been studied with analytical, numerical, and experimental methods for many decades. The steady streaming flow structure has a series of secondary eddies superimposed on the primary harmonically oscillating flow that drives the system. Acoustically driven microstreaming flows have gathered recent attention in the context of microfluidic devices [23], [40] owing to their ability to aid in mixing [41], cause vesicle lysis [30], carry-out well-mixed batch reactions [36], and separate and trap micro-objects such as particles and cells [32], [33], [37], [42]–[44]. Time-averaged viscous steady streaming occurs when an incompressible fluid is oscillated at frequency ω at a low velocity amplitude $U_0 = \omega s$ past obstructions of appropriate characteristic dimension a. Here, s is the amplitude of the fluid oscillation such that $\varepsilon = s/a \ll 1$, and the streaming Reynolds number $Re_s = \varepsilon^2 \omega a^2/\nu$ is small or comparable to unity [45], [46]. After Lord Rayleigh first described acoustic streaming in 1877 [47], Schlichting gave the first modern analytical treatment of steady streaming, ascribing the flow structure to convection of stresses outward from the no-slip condition at the surface through a boundary layer (known as the Stokes layer) of thickness $\delta_{AC} \sim O(\sqrt{\nu/\omega})$, where ν is the kinematic viscosity [48]. The Stokes layer in steady streaming flows is small compared with the obstruction generating fluidic stress, so $\delta_{AC} < a$. Acoustic streaming is often used as an umbrella term for all streaming resulting from acoustic disturbances, but as Riley (2001) noted, steady viscous streaming flows exist independently of compressibility and are thus distinguished from acoustic streaming which implies compressibility in the fluid due to the higher body force exerted by the velocity amplitude [45]. Based on previous experimental work, steady streaming flows of this character retain many of the key traits of a 2D flow when used in a microdevice, though 3D flow characteristics are present near the walls [38].

Research around the mid-century focused heavily on analytical solutions for the 2D case of an infinitely long cylinder oscillating in a fluid [49]–[55]. These studies provided a description of the complex flow structure and its dependence on frequency. Holtsmark, et al. (1954) provided a solution that matched closely with their experiments, and properly described interior and counter-rotating outer eddy systems; see Figure 1 below, where an experimental photograph of the eddy structure is shown. [50].

Figure 1. Photograph showing the inner and part of the outer vortex systems near a circular cylinder, radius 0.11 cm. Exposure time 2 sec. Frequency of the sound 200 cps. from Holtsmark, et al. (1954) [50].

The work of Holtsmark, et al. was expanded heavily upon, with further analytical models and experiments for oscillating cylinders and other shapes and geometries [46], [51]–[59]. Engevik and Svardal (1975) showed analytically that the results for a cylinder oscillating in a quiescent fluid is the same for an oscillating fluid with a fixed obstruction [60]. For all of these cases, it is important to convert the analytical Eulerian flow models to a Lagrangian frame of reference so that they may be accurately compared with experimental images that are generated through use of long-exposure tracer particle streaks (see Figure 1, for example). The need for this conversion in regards to streaming flows was first noted by Skavlem and Tjötta (1955), though the

transformation between the two reference frames has long been known from the work of Stokes relating to drift of particles in deep water waves [61], [62]. The effect of streaming flows on the motion of particles is a main subject throughout this thesis, and as such, this motivates a brief discussion of inertial and non-inertial particle dynamics in general.

Eulerian and Lagrangian flow specifications

Before discussing the physics of inertial particle motion, a brief primer on the common description of fluid motion will be given. Much of the following comes from textbooks on the subject of fluid mechanics and hydrodynamics (e.g. Batchelor (1973), Lamb (1945), Bird, Stewart, and Lightfoot (2002), Landau and Lifshitz (1959), and Kim and Karrila (1991) [7], [63]–[66]). Analytical expressions and models for a range of physics problems are often defined in terms of fixed coordinates, or what is known as the Eulerian specification. With fixed Eulerian coordinates, a general fluid velocity $\mathbf{U}(\mathbf{x}, t)$ is defined by a location $\mathbf{x}$ in the fluid at a given time t. An equation such as the Navier-Stokes equation for incompressible Newtonian fluids,

$$\rho \frac{\mathrm{D}\mathbf{U}(\mathbf{x}, t)}{\mathrm{D}t} = -\nabla p + \mu \nabla^2 \mathbf{U}(\mathbf{x}, t) + \mathbf{f}, \tag{1.1}$$

defines a force balance on an Eulerian control volume centered at $\mathbf{x}$, where ρ is a constant density (incompressible), p is the pressure, μ is the dynamic viscosity, $\mathbf{f}$ represents other body forces (such as buoyancy). The left hand side of Equation (1.1) describes the inertia of the fluid, while the right hand side describes the divergence of stress and body forces on the fluid. In addition, the material derivative,

$$\mathrm{D}\mathbf{U}/\mathrm{D}t = \partial \mathbf{U}/\partial t + \mathbf{U} \cdot \nabla \mathbf{U}, \tag{1.2}$$

is the sum of the unsteady and convective accelerations (or local inertia and convective inertia). In conjunction with the equation of mass continuity and appropriate boundary and initial

conditions, solutions for a flow field may be found either analytically or numerically with the Navier-Stokes equation for a broad range of flow fields and compared easily with fixed Eulerian flow measurements. An example of this type of measurement would be fixed anemometers in the air, measuring wind speed and direction at given **x** as a function of time.

Another way to measure wind speed as a function of space and time would be to track neutrally buoyant weather balloons released from various locations, allowing them to follow the wind. While equally representative of the state of the air currents, these flow measurements are an example of a completely different description of the flow field known as the Lagrangian frame specification of the flow. Whereas Eulerian measurements are fixed in space around a control volume, Lagrangian measurements follow paths centered on point masses (i.e. they are tracers with zero inertia). For non-uniform fields, this difference becomes apparent as tracers traverse gradients in the field and thus experience a net displacement.

Comparison of these Lagrangian measurements with analytical models requires either a model also specified in Lagrangian form, or transformation of Eulerian computations to Lagrangian descriptions. The Navier-Stokes equation can be transformed to Lagrangian coordinates, however the expressions are much more complex and algebraic manipulation is more difficult [67]. An easier alternative to compare Lagrangian measurements of a flow field to analytical results is to compute time-dependent Lagrangian paths $\mathbf{X}(t;\ \mathbf{x})$ by iteratively integrating a known Eulerian flow field $\mathbf{U}(\mathbf{x}, t)$,

$$\frac{\mathrm{d}\mathbf{X}(t;\ \mathbf{x})}{\mathrm{d}t} = \mathbf{U}(\mathbf{x}, t), \tag{1.3}$$

from a given starting location and time. The Lagrangian velocity $\mathbf{V}(t;\ \mathbf{x})$ is simply the time-differentiated Lagrangian path position (i.e. $\mathbf{X}'(t;\ \mathbf{x}) = \mathbf{V}(t;\ \mathbf{x})$). For predicting long time tracer trajectories, computations may be impractical because of the sometimes extremely large time and

spatial scales used (i.e. fine resolution required for accuracy with an overall large domain) [68]. Furthermore, these computed Lagrangian paths are based on the assumption of ideal tracer motion (i.e. a point mass with no inertia moving perfectly with the fluid). A new analysis for computation of inertia particle paths will be shown in Ch. 6 for time-periodic flows.

Stokes drift

As an alternative to exact transformation of an Eulerian field to Lagrangian paths, approximation methods for time-periodic flows may be used to drastically speed computation. The study of non-inertial tracer particles in time-periodic flows dates to the work of G. G. Stokes in 1847 [62], where a mean particle "drift" velocity (beyond the mean Eulerian velocity) was noted in the oscillatory motion of deep water waves. This drift is now known as "Stokes drift", and its computation is largely understood and calculable for well described flows [69]–[74]. The water wave illustration in Figure 2 shows a closed circular particle trajectory with zero mean motion on the left. This would occur if the particle circulated through no velocity gradients. However, in real water waves and many other oscillatory flows the particle circulates through a region with velocity gradients, resulting in a net mass transport, or Stokes drift (i.e. the particle orbit does not return to the starting point).

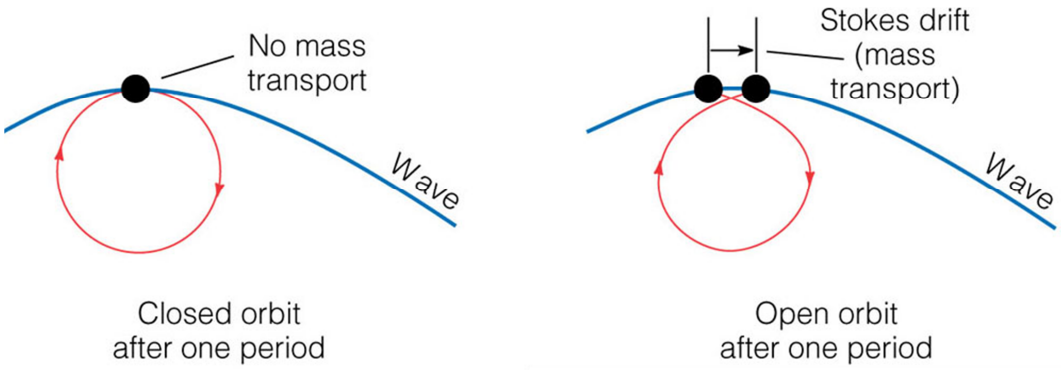

Figure 2. Illustration of effect of Stokes drift on water wave tracer trajectories from [75].

The time-averaged kinematics of non-inertial tracer particles in general time-periodic flow was first approximated by Longuet-Higgins, where mean Stokes drift affecting the Lagrangian motion of a particle causes deviation from the Eulerian mean flow [69], [70]. The analysis starts by assuming a steady-periodic Eulerian velocity $\mathbf{U}(\mathbf{x}, t)$ has a primary *O(ε)* periodic flow and secondary $O(\varepsilon^2)$ steady mean flow

$$\mathbf{U} = \varepsilon\, \mathbf{U}^{osc} + \varepsilon^2\, \mathbf{U}^{st} + \text{H.O.T.}, \tag{1.4}$$

where higher order terms (H.O.T.) are ignored, as are start-up transients prior to the steady-periodic motion. Here, the small parameter $\varepsilon = s/a \ll 1$ is the amplitude of fluid oscillations, s, divided by a characteristic geometric length, a. The time average of the primary oscillating flow, $\mathbf{U}^{osc}$, over one period, is $<\mathbf{U}^{osc}> = 0$. The time-average of $\mathbf{U}^{st}$ is not zero if the primary oscillating flow is non-uniform flow; this non-uniform primary flow drives the secondary steady Eulerian fluid velocity. The Lagrangian particle velocity $\mathbf{V}(t; \mathbf{x}_0)$ follows the dynamical history of a fluid material element at $\mathbf{x}_0$, starting from $t = 0$ [64]. The particle velocity takes a form comparable to fluid velocity perturbation, with a periodic leading order velocity and secondary time averaged motion.

$$\mathbf{V} = \varepsilon\, \mathbf{V}^{osc} + \varepsilon^2\, \mathbf{V}^{st} + \text{H.O.T.}. \tag{1.5}$$

For a non-inertial particle, the instantaneous Eulerian and Lagrangian velocities are equal

$$\mathbf{V}\left(t = 0; \mathbf{x}_0\right) = \mathbf{U}\left(\mathbf{x}_0, 0\right), \tag{1.6}$$

and for a small displacement, $\Delta\mathbf{x}$, the particle velocity can be approximated by Taylor's theorem [76] as

$$\mathbf{V}\left(t\right) = \mathbf{U}\left(\mathbf{x}_0, t\right) + \left(\Delta\mathbf{x}\cdot\nabla\right)\mathbf{U}\left(\mathbf{x}_0, t\right) + \tfrac{1}{2}\left(\Delta\mathbf{x}\cdot\nabla\right)\left(\Delta\mathbf{x}\cdot\nabla\right)\mathbf{U}\left(\mathbf{x}_0, t\right) + \text{H.O.T.}. \tag{1.7}$$

The small displacement is

$$\Delta \mathbf{x} = \int_0^t \mathbf{V}\, \mathrm{d}t, \tag{1.8}$$

where $t = 0$ denotes the beginning of the in-phase periodic motion that drives the flow. Substituting equations and separating by $O(\varepsilon)$ yields,

$$\mathbf{V}^{osc}\left(t\right) = \mathbf{U}^{osc}\left(\mathbf{x_0},\, t\right), \tag{1.9}$$

and at $O(\varepsilon^2)$ one finds

$$\mathbf{V}^{st} = \mathbf{U}^{st}\left(\mathbf{x_0}\right) + \int_0^t \mathbf{U}^{osc}\left(\mathbf{x_0},\, t\right) \mathrm{d}t \cdot \nabla \mathbf{U}^{osc}\left(\mathbf{x_0},\, t\right). \tag{1.10}$$

We ignore solutions of $O(\varepsilon^3)$ and higher. Time-averaging the results from (1.9) and (1.10) over one period yields

$$\left\langle \mathbf{V} \right\rangle\Big|_{\mathbf{x_0}} = \varepsilon^2 \left\langle \mathbf{U}^{st} \right\rangle\Big|_{\mathbf{x_0}} + \varepsilon^2 \left\langle \int_0^t \mathbf{U}^{osc}\, \mathrm{d}t \cdot \nabla \mathbf{U}^{osc} \right\rangle\Big|_{\mathbf{x_0}}. \tag{1.11}$$

The first term on the RHS is the Eulerian steady mean flow; the second term is the mean mass transport or Stokes drift velocity, $\langle \mathbf{V}^{SD} \rangle$. In short, the Stokes drift is the difference between the non-inertial time-averaged Lagrangian particle velocity and the time-averaged Eulerian flow velocity in the oscillatory flow, i.e.

$$\left\langle \mathbf{V} \right\rangle = \left\langle \mathbf{U} \right\rangle + \left\langle \mathbf{V}^{SD} \right\rangle. \tag{1.12}$$

Inertial particle dynamics

The equivalent of Stokes drift for tracer particles with finite inertia has been examined for deep water and capillary water waves [77], [78] but has not been derived for a generalized time-periodic flow, as represented by Eq. (1.4). When a particle has finite inertia, there is a difference between the particle velocity and the local fluid velocity; the tracer is no longer ideal. There are

important cases where naturally occurring oscillatory flows possess usable, though non-ideal, tracers with small but finite inertia, as determined by a small but finite particle Stokes number

$$St = \frac{2U_0 b^2}{9\eta \nu a}, \tag{1.13}$$

where, a is a characteristic length of the undisturbed flow field, b is the particle radius, U_0 is a characteristic fluid velocity, ν is the kinematic viscosity of the fluid, and η is the fluid to particle density ratio. For example, harmful algal blooms in a wavy flow have a diversity of species with a wide range of St where inertia will likely modify the predicted Stokes drift velocity [77], [79]. In our analysis, the particle size ratio is shown to be an important parameter, so we will denote it as $\varphi = b/a$.

Despite a long history of advances, accounting for particle inertia and interactions is an area of active research. A major advance by Maxey and Riley synthesized prior work to derive a general dynamic equation for the velocity, **V**, of a rigid spherical particle in a non-uniform flow field, denoted by the Eulerian-frame velocity **U**,

$$St\frac{\mathrm{d}\mathbf{V}}{\mathrm{d}t} = St(1-\eta)\mathbf{g} + St\,\eta\frac{\mathrm{D}\mathbf{U}}{\mathrm{D}t} - \frac{St\,\eta}{2}\frac{\mathrm{d}}{\mathrm{d}t}\left(\mathbf{V}-\mathbf{U}-\tfrac{1}{10}\varphi^2\nabla^2\mathbf{U}\right) - \left(\mathbf{V}-\mathbf{U}-\tfrac{1}{6}\varphi^2\nabla^2\mathbf{U}\right)$$
$$-\sqrt{\frac{9\eta St}{2\pi}}\int_0^t \frac{\mathrm{d}/\mathrm{d}\tau\left(\mathbf{V}[\tau]-\mathbf{U}[\tau]-\tfrac{1}{6}\varphi^2\nabla^2\mathbf{U}[\tau]\right)}{\sqrt{t-\tau}}\mathrm{d}\tau, \tag{1.14}$$

where **g** is the acceleration due to gravity, and other body forces are not considered. Equation (1.14) holds for weak inertia when St is small compared to unity, resulting in a small difference between the particle and local fluid velocity. As noted in their derivation, the material derivative, Eq. (1.2), follows a fluid element, while the derivative

$$\mathrm{d}\mathbf{U}/\mathrm{d}t = \partial\mathbf{U}/\partial t + \mathbf{V}\cdot\nabla\mathbf{U} \tag{1.15}$$

follows the moving particle [80]. The difference between these two derivatives becomes important with higher-order solutions. For their theory, the particle Reynolds number is assumed to be in the Stokes flow regime (i.e. viscous-dominated). Integrating the stresses on the surface of the particle, including Faxén corrections (of the form $\nabla^2\mathbf{U}$) to the drag of a spherical particle in non-uniform Stokes flow, generates the so-called Maxey-Riley Equation (1.14). This equation contains force terms describing the inertia of a particle, buoyancy, the undisturbed flow field, the added mass due to displacement of the fluid, Stokes drag, and augmented Stokes drag due to the history of the particle (i.e. the Basset-Boussinesq-Oseen history force); however, due to the low Reynolds number assumption and the assumption that the particle is small compared to the characteristic dimension of fluid velocity variations, surface rotation, shear, and lift forces have been neglected [80].

When $St = 0$, Eq. (1.14) shows that $\mathbf{V} = \mathbf{U}$, reducing to an ideal non-inertial tracer. The basic form of the Maxey-Riley equation used here to derive a generalized form of the Stokes drift will include forces from the undisturbed flow field, added mass, Stokes drag and the Basset history force. For simplicitiy, we ignore the Faxén corrections and gravitational forces, as well as additional forces (such as Saffman lift forces [80]–[83]) that have been used to modify Maxey-Riley. This provides the basic equation of motion for weakly inertial particles that we use:

$$St\frac{\mathrm{d}\mathbf{V}}{\mathrm{d}t} = St\,\eta\frac{\mathrm{D}\mathbf{U}}{\mathrm{D}t} - \frac{St\,\eta}{2}\frac{\mathrm{d}}{\mathrm{d}t}\left(\mathbf{V}-\mathbf{U}\right) - \left(\mathbf{V}-\mathbf{U}\right) - \sqrt{\frac{9\eta St}{2\pi}}\int_{-\infty}^{t}\frac{\mathrm{d}/\mathrm{d}\tau\left(\mathbf{V}[\tau]-\mathbf{U}[\tau]\right)}{\sqrt{t-\tau}}\mathrm{d}\tau. \qquad (1.16)$$

The terms we ignore can be important for specific regions of a flow field (e.g. near solid surfaces or other highly non-uniform regions), but they are rarely the dominant terms [81]–[84]. We also follow the common practice of setting the lower limit of integration for the history force $t = -\infty$ rather than $t = 0$, implying the steady periodic motion of the particle and fluid has extended for all time, making the integration of the history force much simpler [85]–[88].

Motivation for our studies

Steady streaming flows have a general form comprised of a primary oscillating motion with superimposed secondary mean flow; in some cases we have observed these flows can trap particles and cells when used in a microfluidic platform. Particle drift in a non-uniform oscillating flow is a fundamental feature of steady streaming motion, even when the particle is free of any inertia. Stoke drift calculations are an efficient method for estimating this time-averaged drift motion for non-inertial particles. However, the role of particle inertia on this drift motion is not well understood in these flows. This thesis seeks to synthesize a general approach for inertial particle dynamics in steady streaming flows that incorporates key physics and is fast to compute.

Research objectives

The following chapters will describe: in Ch. 2, the method used to simulate and visualize steady streaming flows; in Ch. 3, comparisons of flow simulations with experimental measurements [Lieu, House, and Schwartz, "Hydrodynamic tweezers: impact of design geometry on flow and microparticle trapping," *Anal. Chem.*, vol. 84, no. 4, pp. 1963–8, Feb. 2012]; in Ch. 4, a general computation of a time-averaged velocity of an inertial particle in oscillating flows [House and Schwartz, in preparation]; in Ch. 5, a qualitative comparison of predicted trapping locations with experimental trapping in arrays [House, Lieu, and Schwartz, "A Model for Inertial Particle Trapping Locations in Hydrodynamic Tweezers Arrays," in review] and in Ch. 6, a quantitative analysis of how frequency and inertia affect predicted trapping locations for a variety of flows [House and Schwartz, in preparation].

CHAPTER 2 || THEORY AND METHODS

In this chapter, a method for simulating steady streaming flow is described. Using the standard Navier-Stokes equations as a starting point, we approximate the solution using a regular perturbation series with a primary oscillating motion and a second-order steady streaming flow superimposed over the oscillating flow. This assumed solution form leads to a new set of time-independent governing differential equation that are solved numerically using COMSOL finite element method code, where both the computation and visualization are performed. The necessary task of converting Eulerian to Lagrangian streamlines is described by means of the Stokes drift correction.

Governing physics

Mathematical modeling of viscous steady streaming flows begins with the time-dependent Navier-Stokes equation for an incompressible Newtonian fluid,

$$\rho\left(\frac{\partial \mathbf{U}(\mathbf{x}, t)}{\partial t}+\mathbf{U}(\mathbf{x}, t)\cdot\nabla\mathbf{U}(\mathbf{x}, t)\right)=-\nabla p+\mu\nabla^2\mathbf{U}(\mathbf{x}, t)+\mathbf{f}, \tag{2.1}$$

and the mass continuity equation,

$$\nabla\cdot\mathbf{U}(\mathbf{x}, t)=0. \tag{2.2}$$

Here, $\mathbf{U}(\mathbf{x}, t)$ is the Eulerian specification of the fluid velocity at a given point $\mathbf{x}$ and time t, ρ is a constant density (incompressible), p is the pressure, μ is the dynamic viscosity, and $\mathbf{f}$ represents

other body forces like gravity, which will be neglected in further analysis. By taking the curl of the two-dimensional Navier-Stokes equation, the pressure is eliminated from the resulting stream function-vorticity form of the governing equation,

$$\frac{\partial \Omega}{\partial t}+\frac{\partial \psi}{\partial y}\frac{\partial \Omega}{\partial x}-\frac{\partial \psi}{\partial x}\frac{\partial \Omega}{\partial y}=\nu \nabla^2 \Omega, \tag{2.3}$$

where ν is the kinematic viscosity. Here, the stream function ψ is defined as

$$U_x=\frac{\partial \psi}{\partial y}, \tag{2.4}$$

$$U_y=-\frac{\partial \psi}{\partial x}, \tag{2.5}$$

and the vorticity Ω is defined as

$$\Omega=-\nabla^2 \psi. \tag{2.6}$$

The dimensionless form of this equation becomes,

$$\frac{\partial \Omega}{\partial t}+\frac{\partial \psi}{\partial y}\frac{\partial \Omega}{\partial x}-\frac{\partial \psi}{\partial x}\frac{\partial \Omega}{\partial y}=\frac{\nabla^2 \Omega}{M^2} \tag{2.7}$$

where ω is angular oscillation frequency, the vorticity $\Omega = \Omega' \omega$, the stream function $\psi = \psi'/\omega a^2$, time t' has been non-dimensionalized by $t = t'\omega$, position $\mathbf{x}'$ has been non-dimensionalized by $\mathbf{x} = \mathbf{x}'/a$, and $M^2 = a^2\omega/\nu$ is the dimensionless frequency. Further analysis is sped by use of perturbation method techniques applied to the time-periodic flow.

Perturbation technique

Following the approach of Bowman and Schwartz (1998) and later Chen (2006), the flow profile is split into a primary oscillating flow, $\mathbf{U}^{osc}(\mathbf{x}, t)$, and a steady flow, $\mathbf{U}^{st}(\mathbf{x})$. The relative magnitude of the two flows is described by the perturbation series for $\varepsilon = s/a \ll 1$,

$$\mathbf{U}\left(\mathbf{x}, t\right)=\varepsilon\, \mathbf{U}^{osc}\left(\mathbf{x}, t\right)+\varepsilon^2\, \mathbf{U}^{st}\left(\mathbf{x}\right)+\text{H.O.T}, \tag{2.8}$$

where s is the amplitude of fluid oscillations, a is a characteristic geometric length, and higher order terms have been neglected [39], [89]. Using this approach, a fast analytic-numeric solution can be found that removes the need to solve both many small time steps within a cycle as well as many cycles to find the long-time solution [89]. Expanding the oscillating component further into cosine, $\mathbf{U}^c(\mathbf{x})$, and sine, $\mathbf{U}^s(\mathbf{x})$, velocities and describing only leading order oscillating and steady streaming components, the final approximation we use for the flow is

$$\mathbf{U}(\mathbf{x}, t) = \varepsilon\left(\mathbf{U}^c(\mathbf{x})\cos t + \mathbf{U}^s(\mathbf{x})\sin t\right) + \varepsilon^2\,\mathbf{U}^{st}(\mathbf{x}). \tag{2.9}$$

Applying the definition of the stream function from Eqs. (2.4) and (2.5) to the perturbed flow definition in Eq. (2.9), the perturbed stream function and vorticity are found to be

$$\psi(\mathbf{x},t) = \varepsilon\left(\psi^c(\mathbf{x})\cos t + \psi^s(\mathbf{x})\sin t\right) + \varepsilon^2\psi^{st}(\mathbf{x}) \tag{2.10}$$

and

$$\Omega(\mathbf{x},t) = \varepsilon\left(\Omega^c(\mathbf{x})\cos t + \Omega^s(\mathbf{x})\sin t\right) + \varepsilon^2\Omega^{st}(\mathbf{x}). \tag{2.11}$$

Applying Eqs. (2.10) and (2.11) to the Navier-Stokes equation (2.7), a new set of coupled ordinary differential equations is generated at $O(\varepsilon)$,

$$\Omega^c = -\nabla^2\psi^c \tag{2.12}$$

$$\Omega^s = -\nabla^2\psi^s \tag{2.13}$$

$$M^2\,\Omega^s = \nabla^2\Omega^c \tag{2.14}$$

$$M^2\,\Omega^c = -\nabla^2\Omega^s \tag{2.15}$$

where independent variables (i.e. $\mathbf{x}$ and t) have been omitted for clarity. At $O(\varepsilon^2)$, equations with higher harmonic time dependence (i.e. $\cos(2t)$, etc.) are ignored, leaving only the equations for the steady streaming components

$$\Omega^{st} = -\nabla^2\psi^{st} \tag{2.16}$$

and

$$\nabla^2\Omega^{st} = \frac{M^2}{2}\left(\frac{\partial\psi^c}{\partial y}\frac{\partial\Omega^c}{\partial x} - \frac{\partial\psi^c}{\partial x}\frac{\partial\Omega^c}{\partial y} + \frac{\partial\psi^s}{\partial y}\frac{\partial\Omega^s}{\partial x} - \frac{\partial\psi^s}{\partial x}\frac{\partial\Omega^s}{\partial y}\right). \tag{2.17}$$

Stokes drift

Following Skavlem and Tjotta (1955) and general Stokes drift discussion in Ch. 1, the transformation from the Eulerian model to a Lagrangian specification is computed everywhere in the domain by adding the Stokes drift velocity to the mean Eulerian velocity [60], [61]

$$\langle \mathbf{V} \rangle = \langle \mathbf{U} \rangle + \langle \mathbf{V}^{SD} \rangle. \tag{2.18}$$

Estimating the velocity to second order as with the perturbation series Eq. (2.8), the transformation can be approximated as in Eq. (1.11)

$$\langle \mathbf{V}^{SD} \rangle = \varepsilon^2 \langle \int \mathbf{U}^{osc} dt \cdot \nabla \mathbf{U}^{osc} \rangle. \tag{2.19}$$

Now, applying Eq. (2.9), the Lagrangian velocity is computed as

$$\langle \mathbf{V}^{SD} \rangle = \varepsilon^2 \frac{1}{2}\left(-U_y^s\frac{\partial \mathbf{U}^c}{\partial y} + U_y^c\frac{\partial \mathbf{U}^s}{\partial y} - U_x^s\frac{\partial \mathbf{U}^c}{\partial x} + U_x^c\frac{\partial \mathbf{U}^s}{\partial x}\right) \tag{2.20}$$

The Lagrangian stream function ψ^L is generated by solving

$$\nabla^2\psi^L = \frac{\partial\langle \mathbf{V} \rangle_x}{\partial y} - \frac{\partial\langle \mathbf{V} \rangle_y}{\partial x}. \tag{2.21}$$

It should be noted that the Lagrangian motion we are describing here for the steady streaming flow assumes an ideal, non-inertial tracer moving with the local instantaneous velocity of fluid.

Boundary conditions and geometry

We convert our generalized flow formulation into specific flows of interest through the geometries and boundary conditions we apply. A representative 2D geometry representing a centered cylindrical post, radius *a*, is shown in Figure 3**.** Here, the channel length is labeled *L* and half channel width is labeled *w*. For the velocity formulation of the system for a representative geometry, all physical walls (black and blue lines) are set as no-slip conditions, or

$\mathbf{U} = 0$, while the inlet and outlet (red) are set as open periodic boundaries. With the stream function formulation developed in the previous section, no slip and no flux are defined at the top and bottom walls (blue) by $\psi^s = \psi^{st} = 0$, with a constant differential in the cosine stream function defining the oscillatory driving flux through the channel such that $\psi^c = w$ at the top and $\psi^c = -w$ at the bottom; no slip and no flux are defined at the post surface (black) by $\psi^s = \psi^c = \psi^{st} = 0$; and periodic Neumann conditions are used at the left and right walls (red) to set no net flux. The vorticity is left unset at physical surfaces because they generate vorticity in the system.

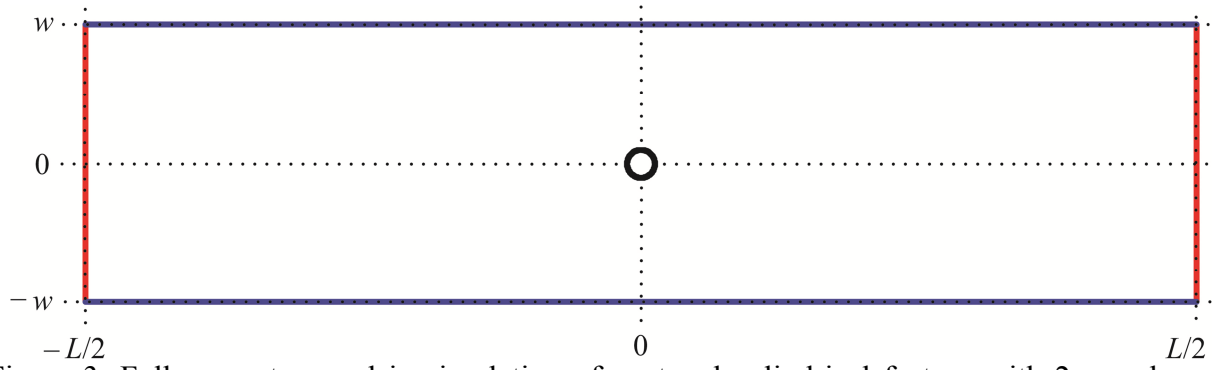

Figure 3. Full geometry used in simulation of centered cylindrical feature with $2w$ = channel width and L = channel length.

Symmetry conditions may be used to simplify the simulation domain and reduce the simulation time as in Figure 4. For this geometry, boundary conditions remain the same for the physical walls at the top (blue) and cylindrical post surface (black). Also open periodic Neumann conditions remain for the inlet and outlet (red). The mid-plane symmetry line (yellow) has stream functions $\psi^s = \psi^c = \psi^{st} = 0$ but also vorticities $\Omega^s = \Omega^c = \Omega^{st} = 0$, indicating that not only is there no flux through the symmetry line, but also that no vorticity is generated at the symmetry line because it does no represent a physical surface.

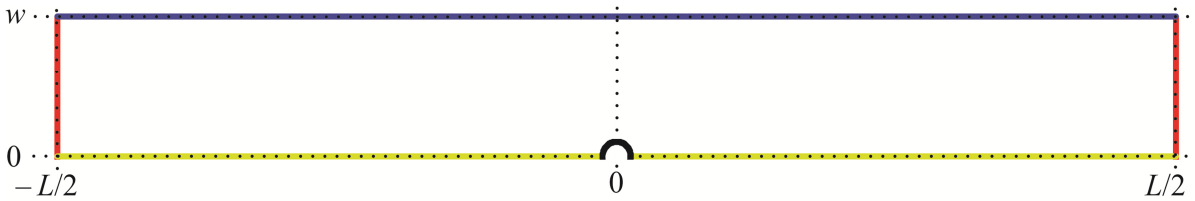

Figure 4. Symmetry geometry used in simulation of centered cylindrical feature with w = channel width and L = channel length.

Modeling steady streaming flows

Simulation setup

With the governing Equations (2.10)-(2.21) through, numerical computation is performed using COMSOL Multiphysics 3.5a by the method of Chen (2006) [39]. COMSOL numerically solves governing physics utilizing finite-element method integration across meshes based on user-defined geometries and boundary conditions. After the geometry over which the governing physics applies, equations and variables are defined as a general form set of partial differential equations across the subdomain with quartic polynomial functions are used as basis functions. Higher polynomial orders in general produce more accurate derivatives, but this must be balanced with increasing degrees of freedoms in the solution phase (i.e. too high of a polynomial order limits the number of mesh elements possible).

After the governing physics and boundary conditions are supplied, a geometry mesh must be generated. The default meshing algorithm supplies finer coverage around geometry boundaries, but this must be refined to provide for the high accuracy needed in our simulations. An automatic mesh was generated with advancing front triangular elements and was further refined to obtain a mesh-independent converged solution. The mesh-independent converged solution was tested by computing boundary integrals at the left and right boundaries and checking for zero net flow. A representative mesh is provided in Figure 5, where an overview of the whole mesh is shown (top) followed magnified sections around the central post (bottom left) and upper right quadrant

of the post (bottom right). The maximum element size in the top right quadrant was reduced to 0.07a for accurate analysis. The appendix of this document describes the general method used to create an appropriately fine mesh. In general, meshes for the following simulations in this chapter average 30,000 to 60,000 elements.

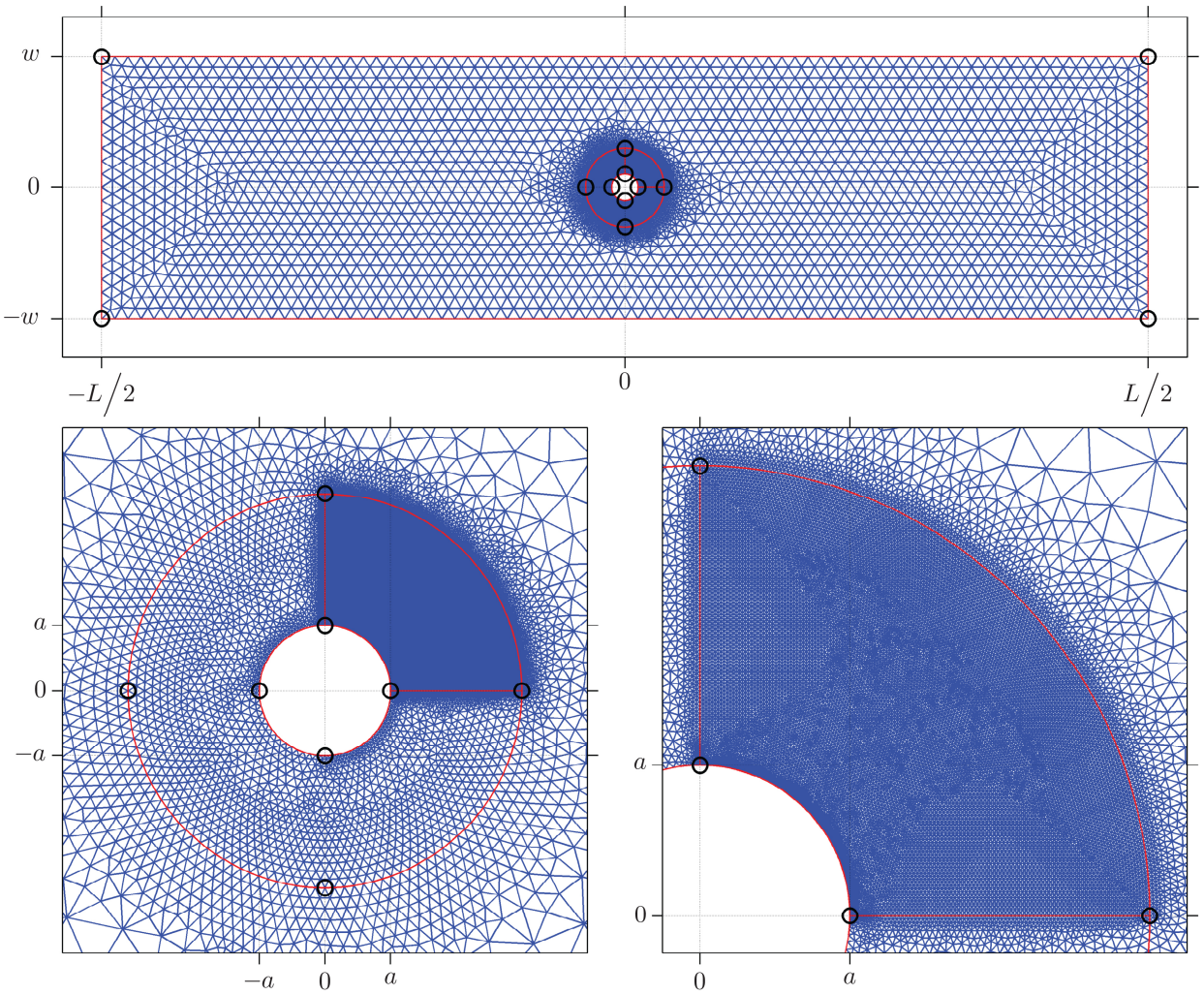

Figure 5. Representative mesh used for computations with 45435 elements (top). Higher mesh refinement is used for the region surrounding the central post (bottom left). Even higher refinement is used for the top quadrant as this area will be used for the majority of analyses (bottom right).

Solution and visualization

Because the Equations (2.12)-(2.15) describing the oscillatory flow are independent of the steady flow Equations (2.16) and (2.17), the coupled linear oscillatory equations can be solved first, reducing the degrees of freedom for simulation of the system. Default settings are chosen

for the UMFPACK solver. Figure 6 shows the visualization of cosine ψ^c (left) and sine ψ^s (right) stream functions for $w = 10$ and $M = 10$. The characteristic length has been normalized to $a = 1$ for this geometry. The shading indicates the magnitude and sign of the stream functions, while the contours depict lines of constant value. Not visualized are the oscillating vorticity amplitudes Ω^s and Ω^c.

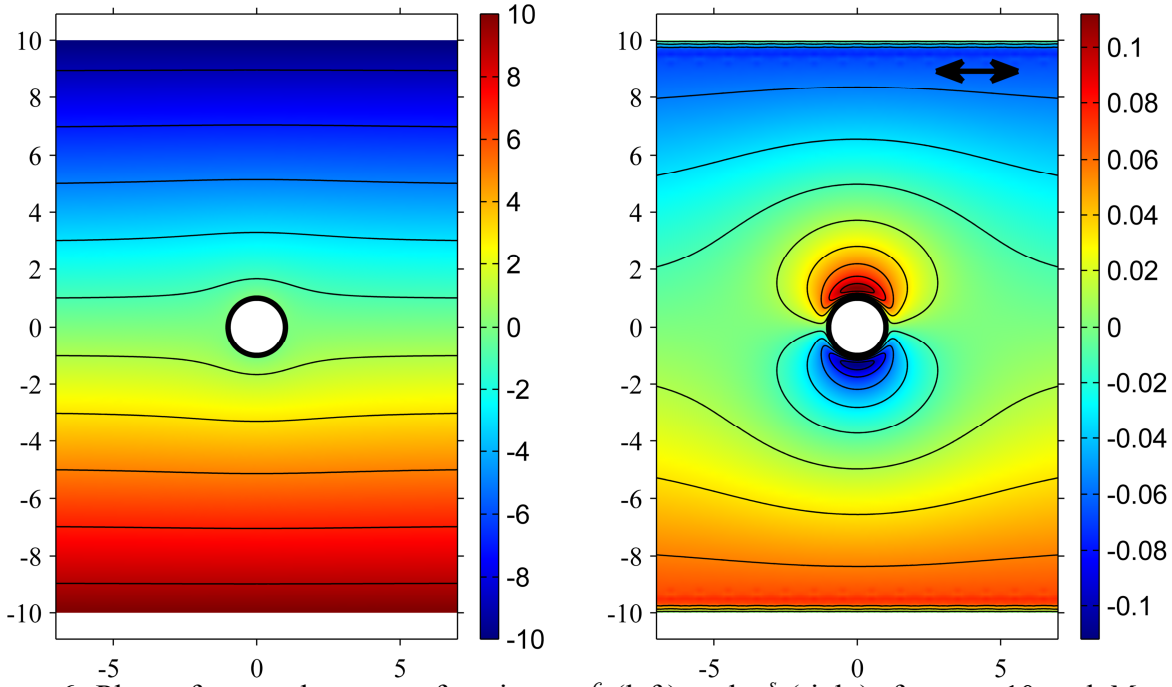

Figure 6. Plots of unsteady stream functions, ψ^c (left) and ψ^s (right), for $w = 10$ and $M = 10$. Shading represents the magnitude of the oscillating stream functions (i.e. amplitude) and the contours depict lines of constant value. The direction of the equivalent oscillatory driving force is left to right for the images.

With ψ^s, ψ^c, Ω^s, and Ω^c known, ψ^{st} and Ω^{st} are computed next for the same conditions as in Figure 6 ($w = 10$ and $M = 10$). In Figure 7, the steady stream function ψ^{st} is visualized. Again, the shading represents the magnitude of the stream function, where the blue areas indicate counter-clockwise flow and the red areas indicate clockwise flow.

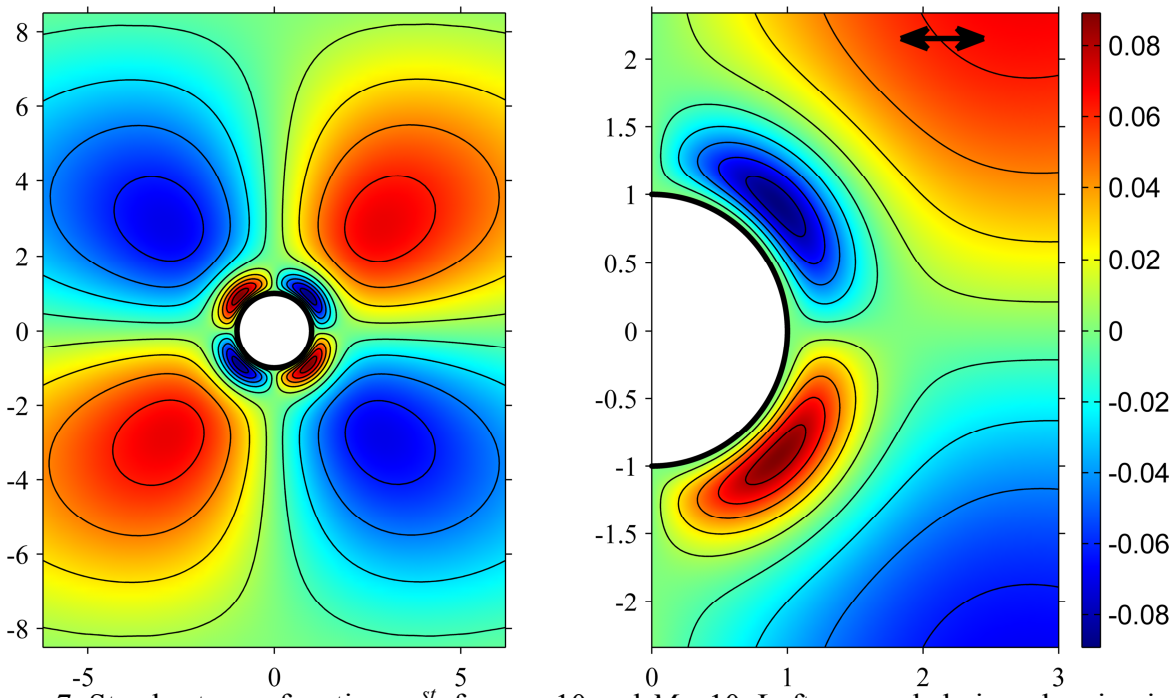

Figure 7. Steady stream function, ψ^{st}, for $w = 10$ and $M = 10$. Left: expanded view showing inner and outer streaming flows. Right: magnified view showing detail of inner eddies. Shading represents the magnitude of the stream function (i.e. amplitude) where blue and red indicate opposite directions of flow. The contours depict lines of constant value. The direction of the equivalent oscillatory driving force is left to right for the images.

The flow shown in Figure 7 looks qualitatively similar to the experimental particle trace images shown earlier, however the steady stream function ψ^{st} is defined from an Eulerian frame of reference, whereas particle trace images are actually depicting a Lagrangian frame of reference. In Figure 8, the Eulerian ψ^{st} and Lagrangian ψ^{L} stream functions are plotted (left and right). It can be easily seen that results are substantially different in total magnitude, while the general shape of the eddies remain predominantly unchanged.

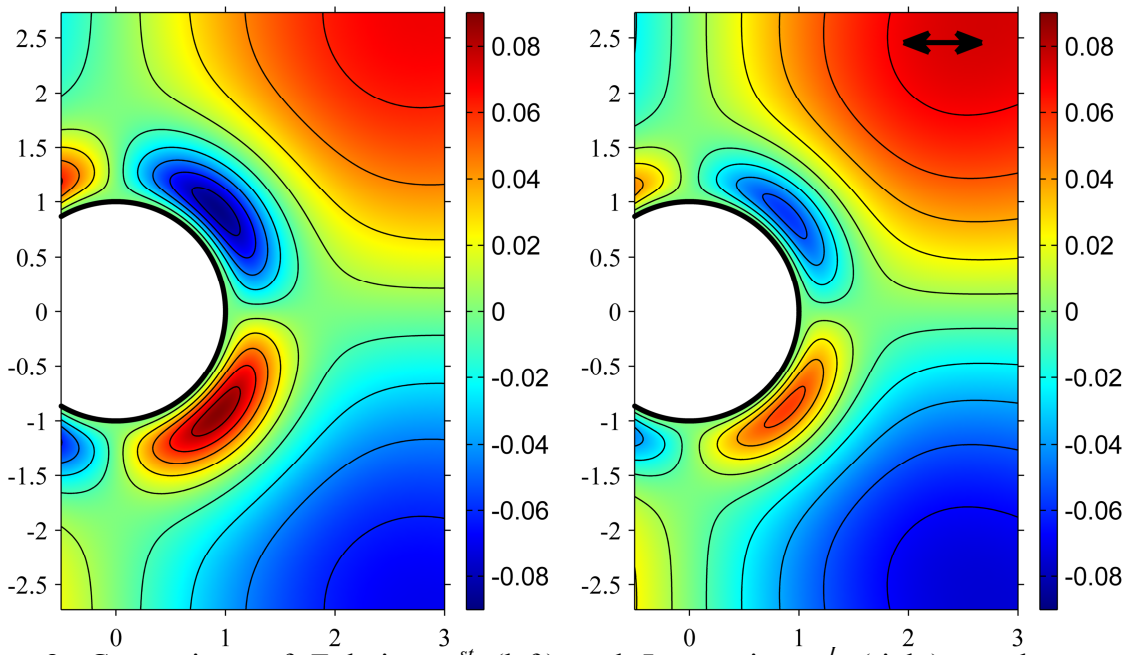

Figure 8. Comparison of Eulerian ψ^{st} (left) and Lagrangian ψ^{L} (right) steady streaming computations, for $w = 10$ and $M = 10$. The shading range is consistent between images, while the contour lines are chosen to best show the flow field.

Conclusion

For a simple means of validation, the previously described analytical work of Holtsmark, et al. 1954 can be compared with simulation results as well. In Figure 9, the distance from an obstruction feature to the center of an eddy over varying Stokes layer thicknesses (i.e. inverse frequency) is plotted for both the Holtsmark, et al. analytical solution and for a COMSOL computation with $w = 10$. Both results have been Stokes drift corrected. As described previously, the Holtsmark, et al. solution is defined for a cylinder in an infinite fluid, with no walls surrounding [50]. The Stokes layer thickness increases as the frequency of oscillation is decreased, causing an increase in the eddy size. It has been seen in experiments and computations that for low frequency steady streaming flows, the eddies can occupy the entire channel width. As such, we would not expect the infinite-fluid solution of Holtsmark to hold under these more realistic circumstances.

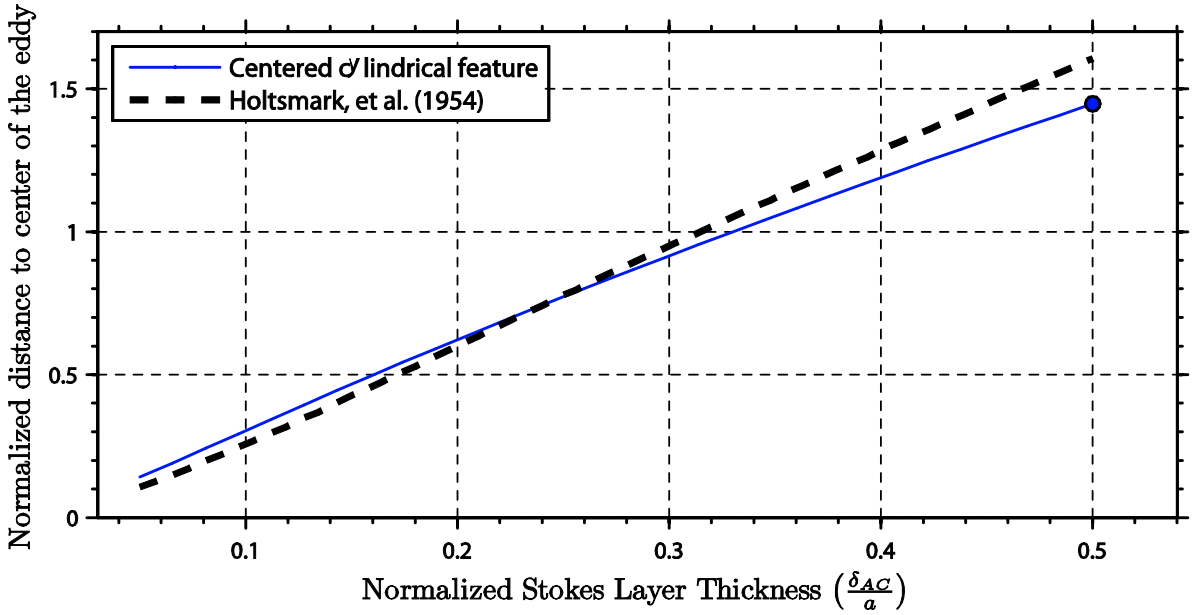

Figure 9. COMSOL computations (w = 10) and Holtsmark, et al. 1954 comparison for non-dimensional distance to center of eddy for varying Stokes layer thickness.

The analytic-numeric approach described in this chapter allows for quick computation of steady streaming flows. Depending on the level of accuracy needed, results can be gained in a matter of minutes. Here, only the simple centered cylindrical post has been simulated to illustrate the process used. Eight new geometries are simulated, fabricated, and compared in detail in Chapter 3. This experimental-computation work serves as an excellent form of validation of the mathematical modeling method and further shows the utility of computation of steady streaming flows as an aid in device design.

CHAPTER 3 || EXPERIMENTAL AND COMPUTED FLOWS

Here we explore the role of microfabricated device geometry on frequency-dependent low Reynolds number steady streaming flow and particle trapping behavior. In our system, flow and particle trapping is induced near an obstruction or cavity located in an otherwise rectilinear oscillating flow of frequency ω and amplitude s in a fluid of kinematic viscosity v. This work expands prior studies to characterize nine distinct obstruction/cavity geometries. The imaged microeddy flows show that the device geometry affects the eddy number, shape, structure, and strength. Comparison of measured particle trap locations with the computed eddy flow structure shows that particles trap closer to the wall than the eddy core. Trapping strength and location are controlled by the geometry and the oscillation frequency. In most cases, the trapping behavior is linearly proportional to the Stokes layer thickness, $\delta_{AC} \sim O((v/\omega)^{1/2})$. We show that steady streaming in microfluidic eddies can be a flexible and versatile method for noncontact microparticle trapping, and hence we call this class of devices "hydrodynamic tweezers".

Experimental device and obstruction geometries

Figure 10a shows a schematic of the 4 layers that make up the microeddy device. The top layer is comprised of two piezo disks that are bonded to the glass coverslip beneath it. The coverslip has two holes that allow fluid to enter the channel of PDMS layer, which is bonded to a glass slide. The region labeled b in the PDMS channel layer is shown as a close-up schematic

view in Figure 10b. Each channel has a series of geometric features that cause the oscillating flow to deviate from a simple unidirectional flow. A series of circular cross-section features are structured, including a cylindrical channel obstruction, a hemi-cylindrical protrusion from the wall, and a hemi-cylindrical cavity on the wall. The channel height is denoted *h*. Fluid oscillations are driven by displacement pumping with the paired piezo-disks. An actual image of the device is shown in Figure 10c, with inlet and outlet fluidic ports attached to the top glass coverslip.

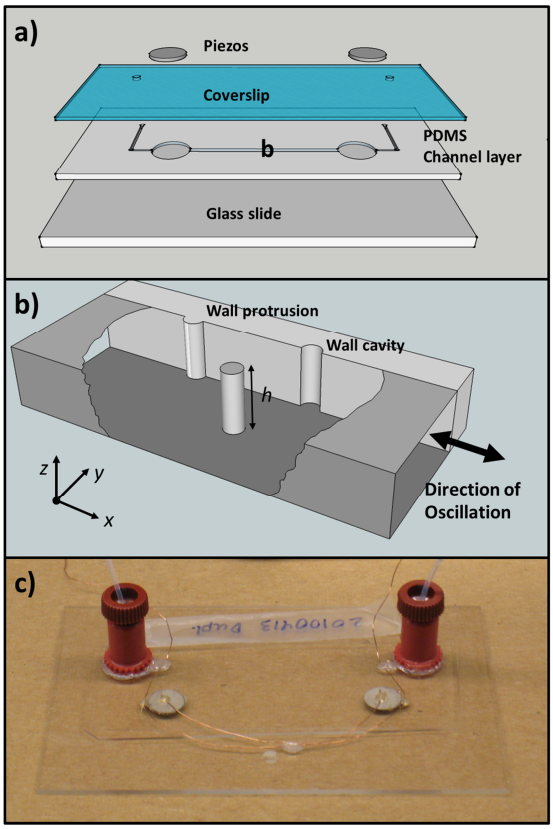

Figure 10. a) Schematic of the microeddy device layers. A thin PDMS microchannel layer is sandwiched between a coverslip and a glass slide. The channel side was bonded to the coverslip. b) Close-up schematic view of the microchannel. A cylindrical channel obstruction lies at the center of the fluid channel, while wall features (protrusion and cavity) are also present. c) Picture of an actual device [42].

As noted, Figure 10b illustrates a channel with obstructions that are circular in cross-section. Figure 11 shows the cross-sections for all the geometries used here. Each cross-section has a

characteristic length denoted a. For example, $2a$ is the diameter of the circular cross-section features or the length of a side on a square or diamond cross-section feature. The first column in Figure 11 shows the cross-sections for freestanding channel obstructions, the second column shows wall protrusions, and the third column denotes cavities on the wall. The actual dimensions of the device were measured using 3D imaging with a laser scanning confocal microscope (LSM 510, Zeiss) The rectangular channel had a height of h = 116 μm, width w = 1000 μm, and length of 30 mm. Typical feature dimensions were a = 25 μm. These physical geometry ratios were used to create corresponding geometries for computation. Device construction details can be found in detail in Lieu, et al. 2012 [42].

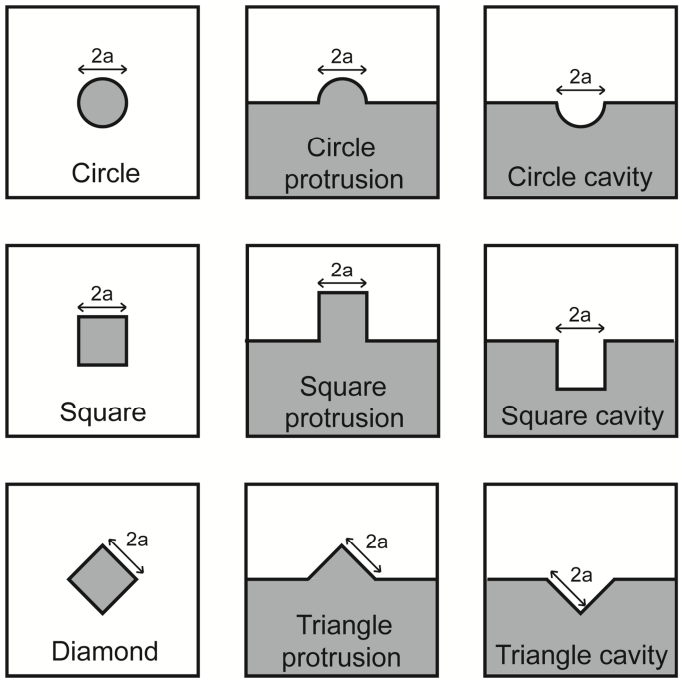

Figure 11. Cross-section view of nine different microchannel feature geometries, placed as illustrated in Fig. 1b. The left column shows free standing channel featured, whereas the other columns show different types of protrusions and cavities on the PDMS walls. The characteristic size is a ≈ 25 μm [42].

Flow conditions and visualization

The device is transparent so flow visualization relied on optical methods such as small fluorescent polystyrene particles of nearly neutral buoyancy (Fluoresbrite® Multifluorescent

Microspheres, d_p=1 μm, ρ_p=1.05 g/cm^3, Polysciences, Inc.) suspended in water (ρ_f = 1.00 g/cm^3, kinematic viscosity ν = 0.0095 cm^2/s). Particles of this size have negligible Stokes number and tend to trace the fluid motion, rather than being trapped. Fluorescence microscopy (TE2000-U, Nikon) with 200-1500 ms exposure time revealed the time averaged particle streak lines. In regions of high streaming flow, particle streaks showed the circulating microeddy motion. When imaged in regions of negligible streaming flow (far from features in the channel or walls), the straight streaks revealed the oscillation amplitude *s*. Amplitude *s* was set by the voltage applied to the piezo oscillation and was limited to (1μm ≤ *s* ≤ 5μm). The piezoelectric disks were driven at audible frequencies from 2 - 20 kHz. All experiments were performed at room temperature.

Flow simulation

Flow in the mid-plane of the microchannel has qualitative and quantitative traits that accurately match 2D steady streaming [38]. To compute the 2-D steady streaming flow, we start with the Navier-Stokes and continuity equations. All experiments employed small amplitude oscillations, $s/a \ll 1$, allowing us to use a regular perturbation approach to separate the periodically oscillating and steady flows. The perturbation parameter was defined as $\varepsilon = s/a$. The primary oscillating flow occurred in the $\sim O(\varepsilon)$ equations and the steady secondary streaming flow equations were $\sim O(\varepsilon^2)$ [39], [89]. The shear stress τ has also been computed from dimensionless values by

$$\tau = \sqrt{\left(\frac{\partial^2\psi^c}{\partial x^2} - \frac{\partial^2\psi^c}{\partial y^2}\right)^2 + \left(\frac{\partial^2\psi^s}{\partial x^2} - \frac{\partial^2\psi^s}{\partial y^2}\right)^2}. \tag{3.1}$$

To convert this to normal units, viscosity of water at room temperature (μ = 0.001 *Pa·s*) is multipled by τ and normalizing variables to find the dimensionalized shear τ'

$$\tau' = \mu\tau\varepsilon\omega. \tag{3.2}$$

Finite-element method computations used COMSOL Multiphysics to sequentially solve the $O(\varepsilon)$ oscillating equations which are then applied to the $O(\varepsilon^2)$ steady streaming equations. All equations were solved in the Eulerian frame of reference. Because flow imaging relied on visualization of particle paths, MATLAB (Mathworks) was used to compute the Stokes drift corrections for the Lagrangian reference frame. For a single cylinder in the center of a wide channel, simulations were validated by comparison with results from analytical solutions [50], [61]. In all simulations shown here, the contours and grey table are identical so that each geometry shows the same absolute range in streaming strength. Lighter colors and low density contours denote weak streaming relative to darker colors and denser contours.

Result and discussion

Oscillating flow and 2D steady streaming

Figure 12-Figure 14 show steady streaming eddies imaged at the midplane of the channel along with comparable 2D simulations. In all of the flows evaluated here, there is no mean flow in or out of the device, so mass conservation requires that any steady flow has closed streamlines. In each case, the oscillation frequency was 4.1 kHz), giving $\delta_{AC}/a = 0.25$. Figure 12 shows the case for obstructions placed in the middle of the channel: 3(a) is a cylindrical post, 3(b) a square cross-section post, and 3(c) a diamond cross-section post. Computed streamlines of these flows are adjacent to each experimental image. The microeddy character of steady streaming is clearly evident in all of the images. Four high symmetry eddies are generated in each quadrants of the cylindrical post. The center of each eddy is located along the 45˚ lines from oscillation axis. Eddies generated by cylindrical obstruction have the highest degree of symmetry (D_4) of all the geometries studied (reflections on the vertical, horizontal, and both 45˚ diagonal lines). For the square posts, eight eddies, two in each quadrant, are observed with D_2 symmetry.

The four major eddies make an angle < 45˚ from the oscillation axis, whereas the four minor eddies are nearly at 90˚ from the oscillation axis. This is particularly evident in the simulation result in Figure 12(b). For the diamond post, four eddies are formed with centers that are > 45˚ from the oscillation axis (Figure 12c). The simulation results suggest that the steady streaming flow gets stronger in going from (a) to (c). Not shown in the experimental images are the complex 3D flow features near the top and bottom channel walls of each obstruction, since our imaging was done at the mid-plane where 2D flow character is expected [38].

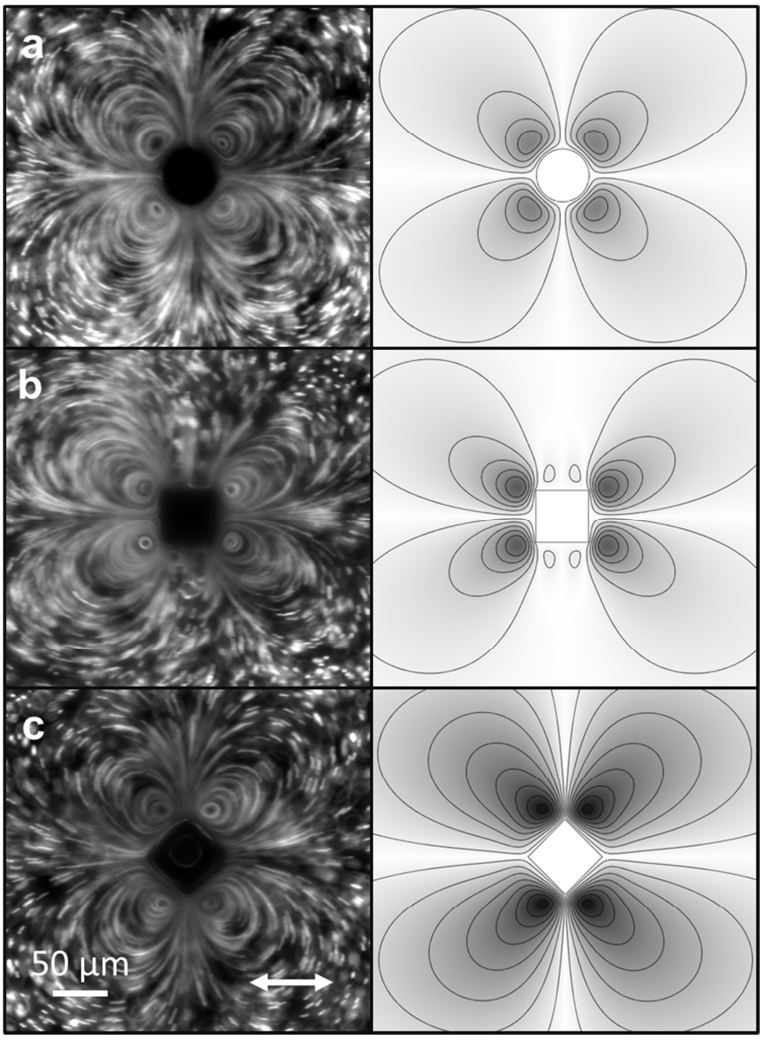

Figure 12. Particle imaging experiments (left column) are compared to the computed Lagrangian streamlines (right column) for channel obstruction geometries: (a) circular cylinder, (b) square post, (c) diamond post. Arrow denotes fluid oscillation direction. Shading and contours for the computed flows are all on the same absolute scale to allow direct comparison of flow strength [42].

Figure 13 shows steady streaming microeddies images generated from protrusion features at the wall, for (a) circular cross-section, (b) square cross-section, and (c) triangle cross-section wall protrusions, with computations of these flows adjacent to each image. All the images reveal an isometric reflection across the vertical line. Compared to freestanding features (Figure 12), the symmetry is somewhat disrupted by the wall. For example, the major eddies for each shape are pushed away from the wall compared to their freestanding counterparts, and are also elongated. The presence of a wall (vs. a symmetry line in Figure 12) results in a weak eddies

adjacent to the wall. These weak eddies are not visibile for these experiments or the selection of simulation stream functions, but the presence of these weak wall eddies are responsible for pushing the major eddies away from the wall. Also note in the experimental image of Figure 13b that a fabrication error to the left of the image has resulted in a nearby eddy that compresses one side of the flow.

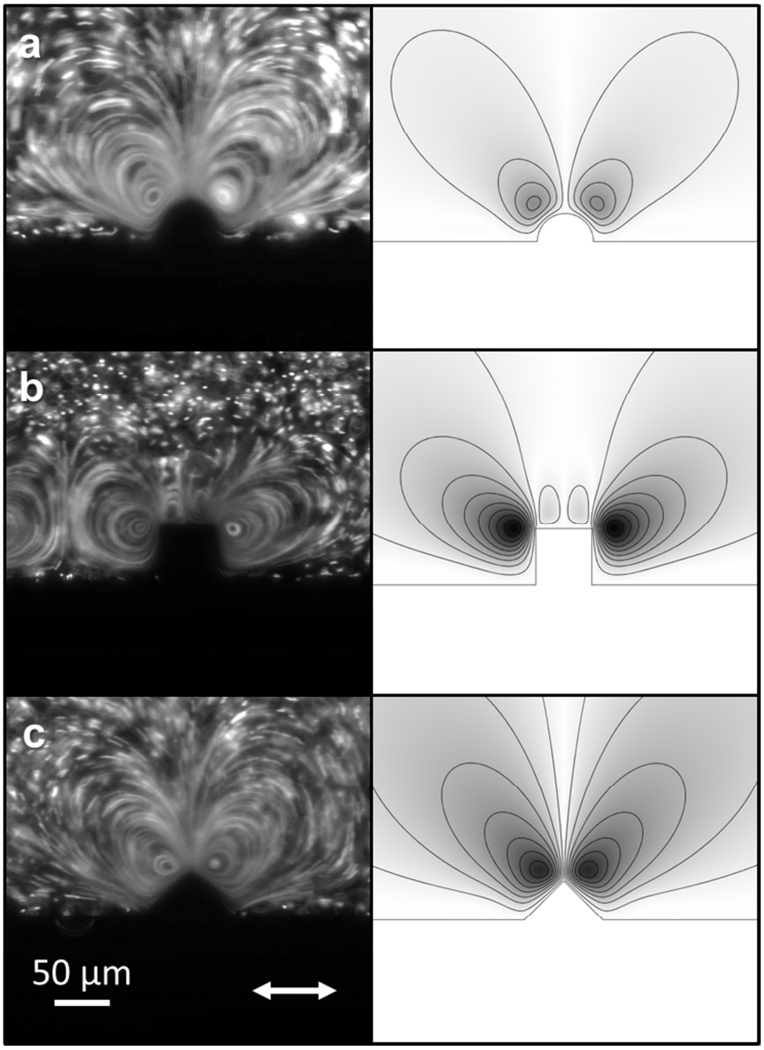

Figure 13. Particle imaging experiments (left column) are compared to the computed Lagrangian streamlines (right column) for protrusion geometries at the channel wall: (a) circle wall protrusion, (b) square wall protrusion, (c) triangle wall protrusion. Arrow denotes fluid oscillation direction. Shading and contours for the computed flows are all on the same absolute scale to allow direct comparison of flow strength [42].

The cylindrical, square, and triangular wall cavities shown in Figure 14 represent the inverse shapes for the wall protrusions in Figure 13. Comparing Figure 13 and Figure 14, we see that the eddy structure for wall protrusions and cavities are decidedly different, aside from isometric reflection symmetry across the vertical line. Each cavity has two moderately strong eddies that penetrate into the cavity, as well as two weak eddies external to the cavity. All of the visible eddies in the experiments and simulation are weaker than those generated from wall protrusions or freestanding structures. In fact, the simulation streamline intervals for the cavities are presented at half the interval of Figure 12 and Figure 13, to reveal the eddy structure.

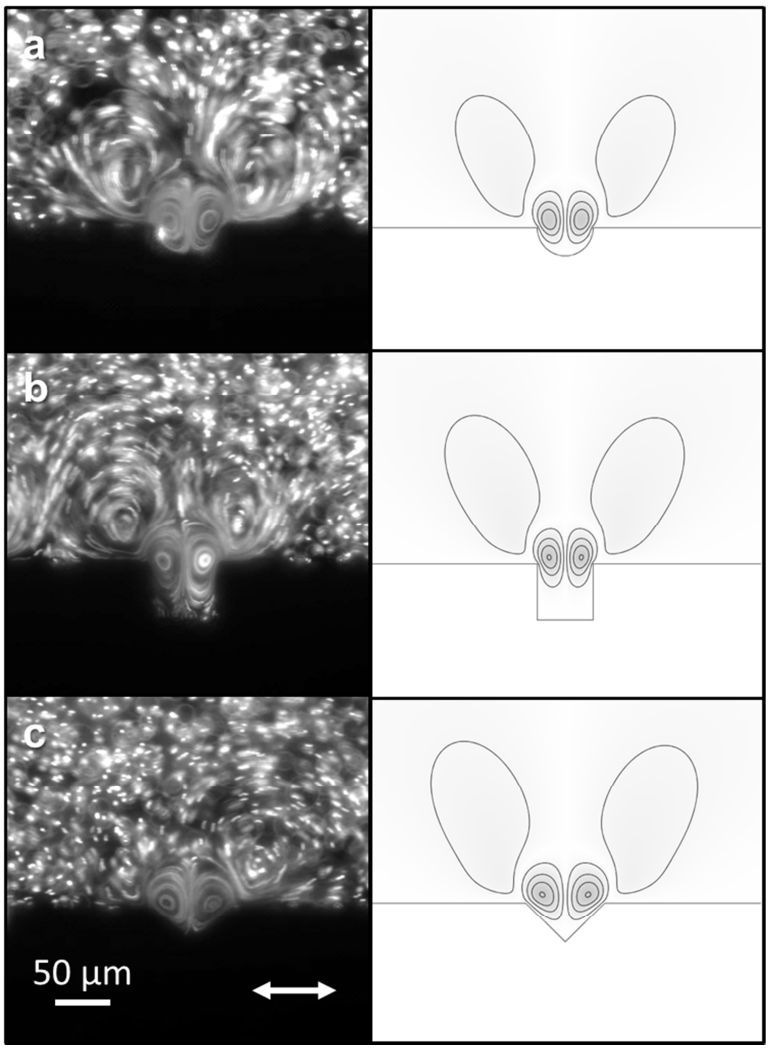

Figure 14. Particle imaging experiments (left column) are compared to the computed Lagrangian streamlines (right column) for wall cavity geometries: (a) circle wall cavity, (b) square wall cavity, (c) triangle wall cavity. Arrow denotes fluid oscillation direction. Shading and contours for the computed flows are all on the same absolute scale to allow direct comparison of flow strength [42].

Frequency dependence of the flow

For the small amplitude oscillations used in these experiments, the steady flow structure (i.e. eddy shape and eddy center) is controlled by the device geometry and the oscillation frequency [50]–[52], [61], [89]. Figure 12Figure 14 show that mid-plane experimental imaging and 2D simulations compare nicely for a single frequency. For each of the 9 device geometries, we evaluate how frequency affects the distance from the strongest eddy's core to the closest wall, to look deeper at the role of device geometry on flow structure.

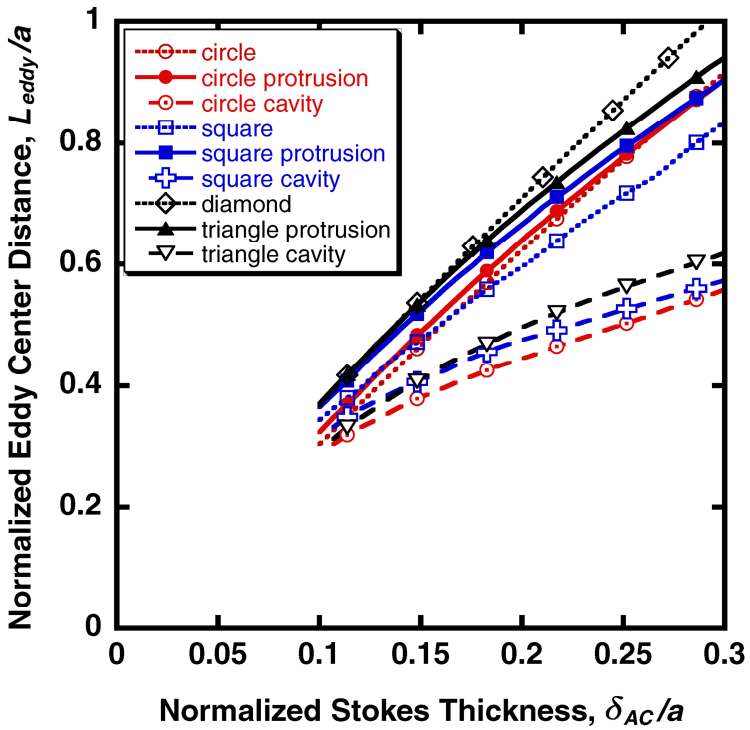

Figure 15. Dimensionless plot of computed eddy center distance as a function of Stokes layer thickness δ_{AC}/a for the 9 geometries evaluated [42].

Figure 15 shows the distance from each major eddy's core to the closes point on the obstruction or wall feature (L_{eddy}), plotted as a function of the inverse root of frequency. The nondimensional eddy size is L_{eddy}/a, and the nondimensional oscillation frequency is represented by the Stokes layer thickness divided by a, δ_{AC}/a. This nondimensionalization shows that the eddy center location has a nearly linear proportionality to the Stokes layer thickness for channel obstructions and wall protrusions. Thus, the scaling relationship between frequency and eddy size that we have seen in previous work on free standing microcylinders holds for other freestanding or protruding obstructions. However, the exact value of the eddy size is geometry dependent. Among the freestanding or protruding geometries, the most dilated eddy centers are found on the diamond post, and the most confined eddies are seen with the freestanding square, though at small Stoke layer thicknesses (high frequency), several of the geometries converge.

The frequency dependence of eddy sizes in cavities is significantly different from the other geometries. Not only are eddies in these experiments significantly closer to the surface because of the geometric constraints inside a cavity, but their sizes also grow at a sub-linear rate with increasing δ_{AC}/a. These geometry dependent eddy sizes have implications for further design of experiments. For example, we have shown previously that large particles are often trapped near the eddy center [38].

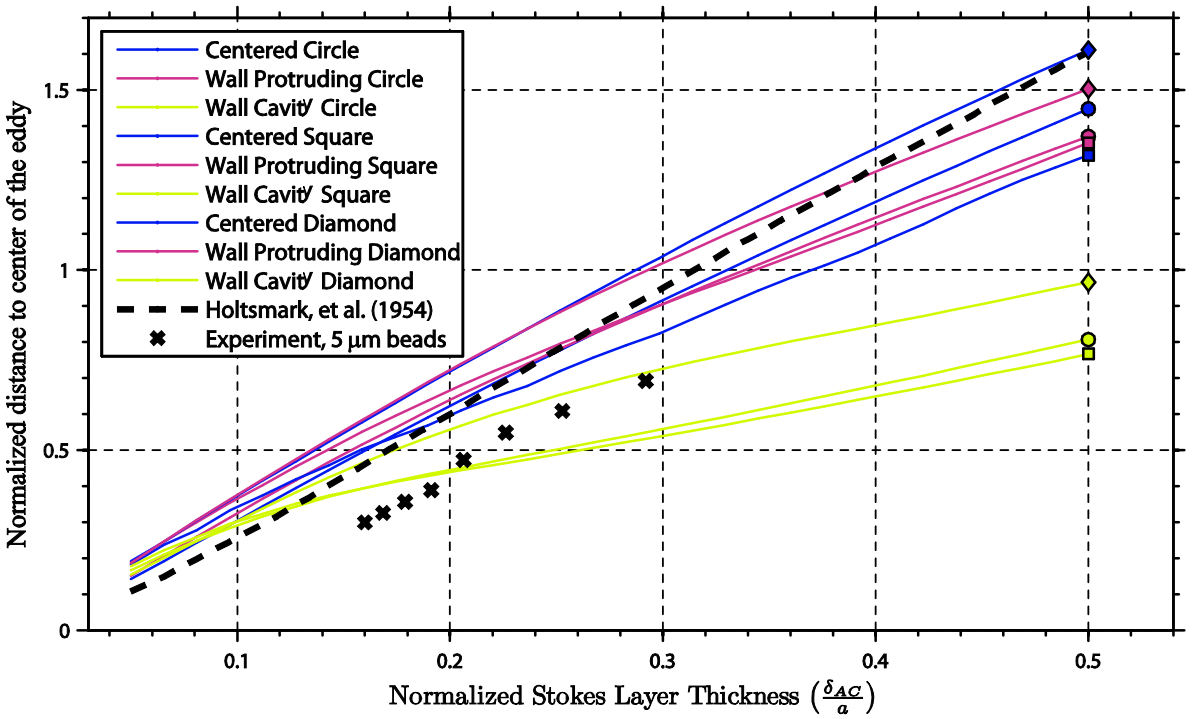

Figure 16. Non-dimensional simulated distance to the center of eddies as a function of the Stokes layer thickness. Final points along line indicate the shape used, while the colors red, yellow, and blue, indicate wall protrusions, centered features, and wall cavities. Small 'x's indicate the trapping of 5 µm particles described in the next section. The dashed line is the analytical solution from Holtsmark, et al. 1954 [50]. This chart was not included in the Lieu, et al. 2012 publication.

As part of the work that was not included in publication of Lieu, et al. 2012, additional simulation work is shown [42]. Figure 16 can be directly compared with Figure 15, in which is shown a non-dimensional plot of the distances to the center of eddies as a function of Stokes layer thickness. Here the general trend and range of values are predicted for each of the

geometries simulated and experimental produced. Most notably, cavity eddies are correctly predicted to be significantly closer in to the walls.

Microparticle trapping in eddies

One of the main functionalities of these low Re steady streaming devices is their ability to trap and hold in one fixed position. We have experimentally observed the trapping of both dense (*e.g.* polystyrene, glass) and buoyant (*e.g.* gas bubbles, oil droplets) particles [38]. Figure 17 shows trapping of 10 μm polystyrene microspheres in the steady streaming flows generated by each device geometry. The trapped spheres are completely suspended within the fluid, not touching walls or moving in x,y or z directions. Trapped particles rotate but do not translate appreciably.

Each panel of Figure 17 shows one trapped particle. All other sites with comparable symmetry are also observed to stably trap particles, so we denoted by the "x". We do not fill all of the traps simultaneously because, to do so, would produce a distribution with some traps containing more than one particle. Qualitatively, Figure 17 shows that stably trapped particles are located at positions similar to the center locations for the main eddies seen in Figure 12-Figure 14. Thus, the symmetry of the trapping is closely reflecting the symmetry of the eddies, as expected. Note that Figure 17(i) has no particle or "x" shown. The eddy flow for a triangular wall cavity is the weakest of all studied (cf. Figure 14c with all others). Apparently, this leads to unstable trapping of particles within those eddies. Though we sometimes see trapping for the triangular cavity, small disturbances cause the trapping to be transient. Similarly, the weak minor eddies associated with square posts and square protrusions also display unstable trapping behavior. Thus, our results show that trapping stability is linked to the strength of the flow generated by a particular geometry.

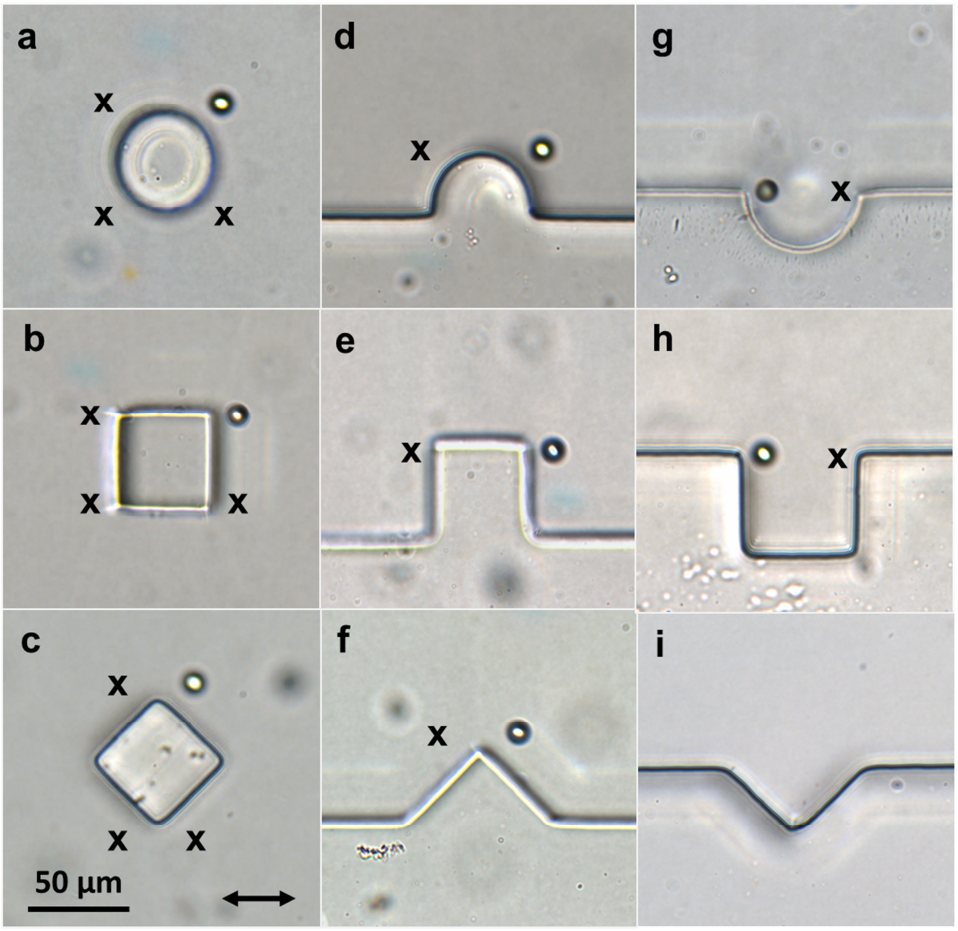

Figure 17. 10 µm polystyrene microspheres trapped in steady streaming eddies generated by different geometries. All trapping was performed at very low particle densities, so we show an "x" to indicate symmetric, but unfilled, trapping locations. Image (i) displayed no stable trapping sites for the range of conditions used here. Arrow denotes fluid oscillation direction [42].

We expect the particle trapping location to be dependent on the device geometry and the dimensionless Stokes layer thickness. See the paper for a plot of the characteristic trapping distance *L/a*, defined as the distance from the trapped particle center to its nearest surface as a function of dimensionless Stokes layer thickness. The particle trapping location has a near linear relationship between the trapping distance and the Stokes layer thickness $\delta_{AC} \sim (\nu/\omega)^{1/2}$ for the nine design geometries. Particles often trap close to the boundary of the Stokes layer, where shear stress in the primary oscillating flow is high. This issue may be important for cell trapping, where shear sensitivity is commonly observed. In Figure 18, the simulated magnitude of the

shear stress for a centered cylindrical post is calculated based on gradients in the oscillating flow and plotted. Here, we see a peak in the shear stress on either side of the post, with a much lower shear calculated (~ 10 *Pa*) near the center of the eddy where particles trap. Simulations of shear may be performed easily for all of the geometries shown and vary greatly. Work of this nature may be beneficial in future studies to help explain trapping behavior for various obstruction shapes and geometries. Thus, it is useful to remember that features like trapping, that we associate with the steady flow field, remain connected to the physics of the fast oscillating flow.

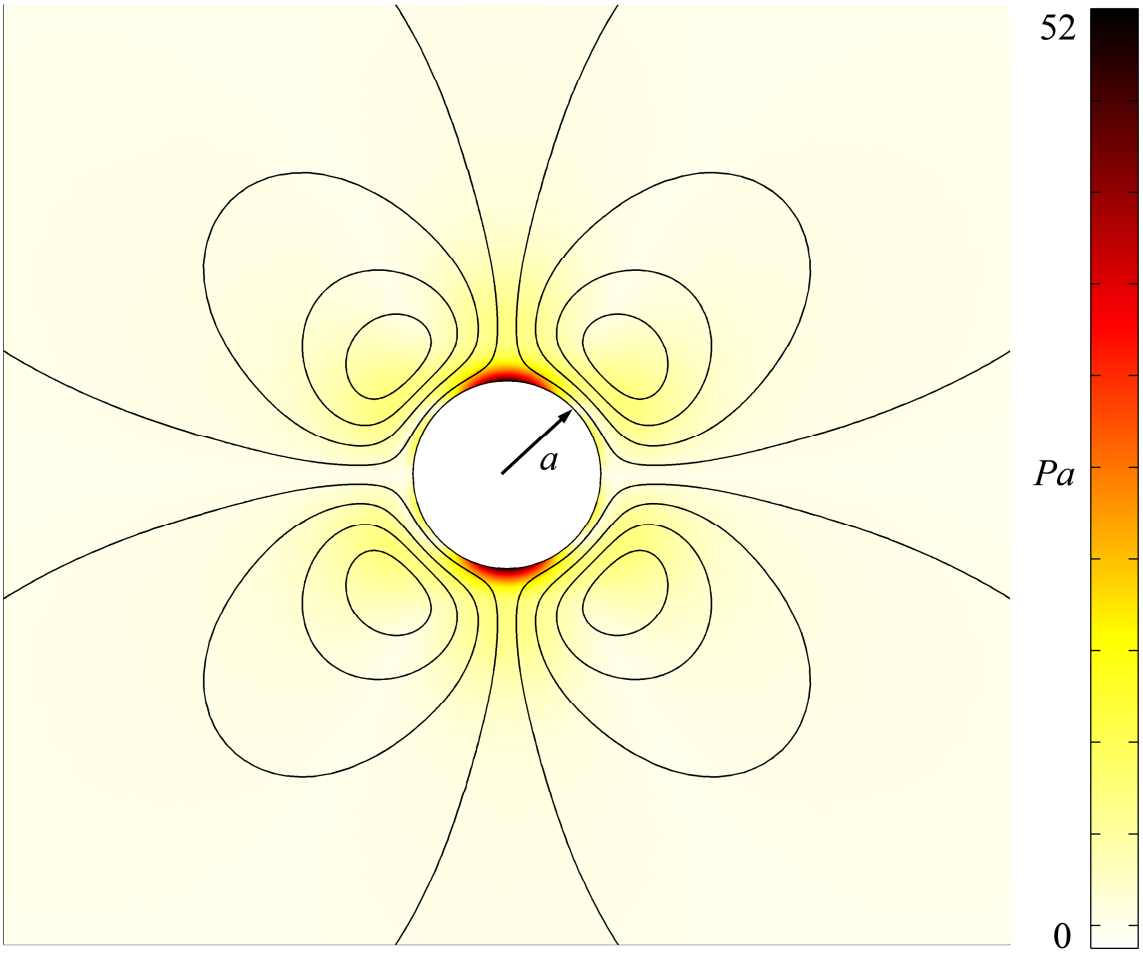

Figure 18. Shear stress magnitude shading for a centered cylindrical post of radius a = 25 μm and frequency f = 4.1 kHz. Contours are plotted for the steady Lagrangian stream function. This chart was not included in the Lieu, et al. 2012 publication.

Our previous work with cylindrical geometries suggested that trapping occurred quite close to the computed eddy center [38]. There are several differences between these experiments and previous results, leading to the following conjectures. Foremost, our current device fabrication is an order of magnitude smaller and uses elastomeric materials rather than rigid materials for construction. Though we non-dimensionalize appropriately to remove size and frequency effects, material compliancy has not been addressed previously. The rubbery PDMS and higher frequencies associated with smaller systems create opportunities for small but observable compliance effects and structural resonance in the device. Moreover, small defects in fabrication will give rise to larger effects as fabrication length scales shrink. We also know that trapping is dependent on the particle size and the surrounding media properties, via the particle Stokes number, $St = d_p^2 \rho_p \omega/(18\mu)$, as described by the Maxey-Riley equation for particle transport [39], [80], [86]. For example, very small particles ($d_p \ll a$) are not observed to trap, but particles comparable in size to a do trap (*cf.* Figure 12Figure 14 with Figure 17). In short, a more quantitative theory for the stability and locations of steady streaming traps, as well as their dependencies on particle Stokes number, is necessary to accelerate our understanding of these scaling effects. At the time of publication, computational work was not finalized enough for print. New computational work regarding particles and trapping will be discussed in detail in the following chapters.

Conclusion

We have explored 9 different steady streaming microdevice geometries to evaluate the connection between geometry, steady streaming flow, and microparticle trapping. The overall features of flow and particle trapping adjacent to wall protrusions and freestanding posts are quite similar among geometric pairs. Cavities have a significantly different steady flow

structure, flow strength, and particle trapping stability. At a finer scale, replacing a flow symmetry line in a freestanding feature with a wall slightly disrupts the symmetry and shape of the eddy. Though we have established a fast and valuable 2D-based computational design methodology for understanding flow near the device mid-plane, we describe the need for more quantitative methods to predict details of the particle trapping physics.

The scale of experiments demonstrated here, along with the ability of these devices to trap and position cell-sized objects at a fixed point in x, y, and z suggests that steady streaming traps are well suited for cell separation, filtering, and single-cell analysis. We are exploring these elements further in on-going research.

CHAPTER 4 || STOKES DRIFT FOR FINITE-INERTIA PARTICLES IN A GENERALIZED STEADY STREAMING FLOW

In this paper we study the effects of inertial on particle motion in general steady streaming flows. The well-known Maxey-Riley equation forms the base equation for the instantaneous velocity of an inertial particle. The time-averaged effects of inertial are elucidated through a novel inertial Stokes drift analysis. For these flows, first order oscillating components and second order streaming components are simulated using a fast analytic-numeric approach given parameters matching experiments for viscous streaming in an array of Hydrodynamic Tweezers. The St-dependent Lagrangian particle paths are compared against ideal tracer paths and time-averaged projections of the location after a period of oscillation given only characteristics of the initial location. The magnitude and angle of deviations from ideal tracer motion is predicted for the entire flow field. The angle of deviation from ideal tracer motion is found to be constant at a given location regardless of characteristics of the inertia of the particle. Furthermore, the magnitude of the deviations at a given location is found to show a linear relationship with increasing product of the particle density ratio and the particle Stokes number.

Introduction

A small tracer particle with no inertia and instantaneous velocity equal to that of the local fluid does not, in general, trace a closed orbit in a non-uniform periodic flow; there is a drift

velocity superposed on the periodic motion. The study of non-inertial tracer particles in time periodic flows dates to the work of G. G. Stokes in 1847 [62], where this particle drift velocity was noted in the oscillatory motion of deep water waves. This drift is now known as "Stokes drift", and its computation is largely understood and calculable for well described flows [69]–[74].

The equivalent of Stokes drift for tracer particles with finite inertia has been examined for deep water and capillary water waves [77], [78] but has not been derived for purely time-periodic flows. When a particle has finite inertia, there is a difference between the particle velocity and the local fluid velocity; the tracer is no longer ideal. There are important cases where naturally occurring oscillatory flows possess usable, though non-ideal, tracers with small but finite inertia, as determined by a small but finite particle Stokes number

$$St = \frac{2U_0 b^2}{9\eta \nu a}, \tag{4.1}$$

where, a is a characteristic length of the undisturbed flow field, b is the particle radius, U_0 is a characteristic fluid velocity, ν is the kinematic viscosity of the fluid, and η is the fluid to particle density ratio. For example, harmful algal blooms in a wavy flow have a diversity of species with a wide range of St where inertia will likely modify the predicted Stokes drift velocity [77], [79].

Likewise, we (and others) have been developing microfluidic devices that utilize secondary steady streaming in a primary oscillating flow to study, transport, and trap a wide range of particles [33], [41], [42]. In these streaming microfluidic systems, particle inertia causes a deviation from the expected fluid-following behavior of an ideal non-inertial tracer.

Here we wish to understand the role of small but finite inertia on modifications to the predicted Stokes drift for a particle in a steady periodic flow. Maxey and Riley [80] derived a

general kinematic equations for the velocity, **V**, of a rigid spherical particle in a non-uniform flow field, denoted by the Eulerian-frame velocity **U**:

$$St\frac{\mathrm{d}\mathbf{V}}{\mathrm{d}t} = St\eta\frac{\mathrm{D}\mathbf{U}}{\mathrm{D}t} - \frac{St\eta}{2}\frac{\mathrm{d}}{\mathrm{d}t}(\mathbf{V}-\mathbf{U}) - (\mathbf{V}-\mathbf{U}) - \sqrt{\frac{9\eta St}{2\pi}}\int_{-\infty}^{t}\frac{\mathrm{d}/\mathrm{d}\tau\,(\mathbf{V}[\tau]-\mathbf{U}[\tau])}{\sqrt{t-\tau}}\mathrm{d}\tau. \qquad (4.2)$$

Equation (4.2) holds for weak inertia when *St* is small compared to unity, resulting in a small difference between the particle and local fluid velocity. As noted in their derivation, the material derivative

$$\mathrm{D}\mathbf{U}/\mathrm{D}t = \partial\mathbf{U}/\partial t + \mathbf{U}\bullet\nabla\mathbf{U} \qquad (4.3)$$

follows a fluid element, while the derivative

$$\mathrm{d}\mathbf{U}/\mathrm{d}t = \partial\mathbf{U}/\partial t + \mathbf{V}\bullet\nabla\mathbf{U} \qquad (4.4)$$

follows the moving particle [80]. The difference between these two derivatives becomes important with higher-order solutions (see later). In the limit $St \rightarrow 0$, equation (4.2) shows that **V** = **U**, resulting in the ideal non-inertial tracer. In this basic form of the Maxey-Riley equation, forces from the undisturbed flow field, added mass, Stokes drag and the Basset history force are included. For clarity in our results, we ignore several additional terms that sometimes modify equation (4.2), including Faxén corrections, gravitational forces, and Saffman lift forces [80]–[82]. These terms can be important for specific regions of a flow, for example, near solid surfaces or other highly non-uniform regions, but they are rarely the dominant terms [81]–[84]. Additional physics may be added when applicable to the flow field characteristics.

Here our goal is to explore the role of weak inertia in the computation of Stokes drift for non-ideal tracers in a generalized non-uniform primary oscillating flow. Stokes drift calculations are involved in transformation of the secondary steady streaming motion between the Lagrangian and Eulerian frames [45], [52], [61], [90]. We illustrate the generally applicable results presented here with a specific example of interest in our group.

Theory and methods

Approximation for the instantaneous particle motion in a generalized oscillating flow

We define a general periodic flow velocity $\mathbf{U}(\mathbf{x}, t)$ at a given Cartesian point $\mathbf{x}$ and time t as

$$\mathbf{U}\left(\mathbf{x},\, t\right) = \varepsilon\left(\mathbf{U}^{c}\left(\mathbf{x}\right)\cos t + \mathbf{U}^{s}\left(\mathbf{x}\right)\sin t\right) + \varepsilon^{2}\,\mathbf{U}^{st}\left(\mathbf{x}\right) + \text{H.O.T.}, \tag{4.5}$$

with first order oscillating components $\mathbf{U}^{c}(\mathbf{x})$ and $\mathbf{U}^{s}(\mathbf{x})$ driving a second order steady motion $\mathbf{U}^{st}(\mathbf{x})$, where the amplitude of fluid oscillations, s, is small compared to a characteristic length, a, such that $\varepsilon = s/a \ll 1$. For compatibility with the flow field formulation and Eq. (4.5), the particle velocity $\mathbf{V}(t; \mathbf{x})$ at time t with center of mass located at $\mathbf{x}$ is similarly defined

$$\mathbf{V}\left(t;\mathbf{x}\right) = \varepsilon\left(\mathbf{V}^{c}\cos t + \mathbf{V}^{s}\sin t\right) + \varepsilon^{2}\,\mathbf{V}^{st} + \text{H.O.T.} \tag{4.6}$$

Examining equation (4.6), one sees an appropriate expansion for small Stokes numbers is

$$\mathbf{V} = \mathbf{V}_{0} + \mathbf{V}_{1}\,St + \mathbf{V}_{3/2}\,St^{\,3/2} + \mathbf{V}_{2}\,St^{\,2} + \text{H.O.T.} \tag{4.7}$$

Furthermore, each of the particle velocity components in Eq. (6)—$\mathbf{V}^{c}$, $\mathbf{V}^{s}$, and $\mathbf{V}^{st}$—can be expanded in the form of Eq. (4.7). Applying Eqs. (4.5)-(4.7) to Eq. (4.2), one can segregate the velocity components by Stokes number orders. Among the $O(\varepsilon)$ primary oscillatory velocity components the non-inertial $St = 0$ solution is

$$\mathbf{V}_{0}^{c} = \mathbf{U}^{c} \tag{4.8}$$

and

$$\mathbf{V}_{0}^{s} = \mathbf{U}^{s}\,. \tag{4.9}$$

Collecting the oscillating components that display inertial effects at $O(St)$ provides

$$\mathbf{V}_{1}^{c} = \left(\eta - 1\right)\mathbf{U}^{s} \tag{4.10}$$

and

$$\mathbf{V}_{1}^{s} = -\left(\eta - 1\right)\mathbf{U}^{c}\,, \tag{4.11}$$

whereas oscillating solutions at $O(St^{3/2})$ are

$$\mathbf{V}^c_{3/2} = \tfrac{3}{2}(\eta - 1)\sqrt{\eta}\left(\mathbf{U}^c - \mathbf{U}^s\right) \tag{4.12}$$

and

$$\mathbf{V}^s_{3/2} = \tfrac{3}{2}(\eta - 1)\sqrt{\eta}\left(\mathbf{U}^c + \mathbf{U}^s\right), \tag{4.13}$$

while the $O(St^2)$ components are

$$\mathbf{V}^c_2 = \left(-4\eta^2 + 5\eta - 1\right)\mathbf{U}^c \tag{4.14}$$

and

$$\mathbf{V}^s_2 = \left(-4\eta^2 + 5\eta - 1\right)\mathbf{U}^s . \tag{4.15}$$

For the physics incorporated in Eq. (4.2), we see that all the oscillating components of flow reduce to the ideal tracer behavior when the density of the particle equals that of the fluid, or $\eta = 1$. This dependence on particle density ratio matches previous analytical results for particles in turbulent flows [91], [92] and wavy flows [77], [78]. For all other densities, the oscillating velocity components for the particle and fluid deviate. The $O(St)$ contributions to this deviation arise from the undisturbed flow field, added mass, and Stokes drag terms of the Maxey-Riley equation, and Eqs. (4.10) and (4.11) show that they produce an out-of-phase oscillatory motion in the particle compared to the fluid. At $O(St^{3/2})$, contributions from the Bassett history term show up in the particle motion, whereas the $O(St^2)$ terms introduce additional contributions from the added mass.

The physics of the secondary steady particle motion at $O(\varepsilon^2)$ has contributions from the steady streaming flow, Stokes drift, and inertial deviations from the non-inertial Stokes drift [93]. Here, we focus only on the time-independent solutions at $O(\varepsilon^2)$, not the higher harmonic motion of the particle. The $St = 0$ steady solution is

$$\mathbf{V}_0^{st} = \mathbf{U}^{st}, \tag{4.16}$$

as expected. The next highest term, at $O(St)$, is

$$\mathbf{V}_1^{st} = \frac{3}{4}\eta\left(U_x^c \frac{\partial \mathbf{U}^c}{\partial x} + U_x^s \frac{\partial \mathbf{U}^s}{\partial x} + U_y^c \frac{\partial \mathbf{U}^c}{\partial y} + U_y^s \frac{\partial \mathbf{U}^s}{\partial y} \right). \tag{4.17}$$

Equation (17) has terms that arise from the drag on the particle, the added mass of moving the fluid from the path of the particle, and the convective inertial terms in the undisturbed flow (i.e., contributions from Eqs. (4.3) and (4.4) of the form $\mathbf{U}\cdot\nabla\mathbf{U}$). The remaining terms up to $O(St^2)$ are

$$\mathbf{V}_{3/2}^{st} = 0 \tag{4.18}$$

and

$$\mathbf{V}_2^{st} = \frac{1}{4}(\eta - 1)\eta\left(U_x^s \frac{\partial \mathbf{U}^c}{\partial x} - U_x^c \frac{\partial \mathbf{U}^s}{\partial x} + U_y^s \frac{\partial \mathbf{U}^c}{\partial y} - U_y^c \frac{\partial \mathbf{U}^s}{\partial y} \right). \tag{4.19}$$

Equations (4.8)-(4.19) can be combined into Eq. (4.7) to approximate the instantaneous velocity of a particle with initial location $\boldsymbol{x}_0$, when the flow field is comprised of a steady-periodic motion with a secondary time-invariant streaming of the form of Eq. (4.6).

It is interesting to note that the influence of inertia on the oscillatory motion of the particle vanishes when $\eta = 1$ in Eqs. (4.10)-(4.15), but Eq. (4.17) shows that inertia influences the mean velocity of the particle even when $\eta = 1$. In short, there are realistic conditions ($\eta = 1$) where the oscillatory velocity of the particle is independent of St, and yet the mean particle motion displays a St-dependency. When St is finite, there is a difference in the relaxation time of the transported particle and the flow. Interestingly, we have previously shown a related effect in oscillatory convection mass transfer systems, where there can be significant secondary mean displacements without significant periodic fluctuations in the transported species, when the mass transfer and hydrodynamic relaxation timescales differ [94].

Inertial Stokes drift

The time-averaged kinematics of non-inertial particles was well described by Longuet-Higgins, where the Lagrangian motion of a particle in a non-uniform oscillating flow field caused Stokes drift deviations beyond the purely Eulerian mean flow [69], [70]. Following that analysis, we investigate time-averaged steady motion of particles using our approximation for the instantaneous particle velocity, derived in the previous section. Our generalized steady periodic flow approximations are expected to be accurate for small modulation amplitudes ($\varepsilon \ll 1$) and weak inertia ($St \ll 1$). When a particle has inertia, the Eulerian velocity of fluid does not generally equal the Lagrangian velocity of the particle at a given point and time, as is evident in the derivation of the previous section, producing a relative velocity, $\mathbf{W}(\mathbf{x}, t; St, \eta)$, between the two, i.e.

$$\mathbf{V} = \mathbf{U} + \mathbf{W} \tag{4.20}$$

Here, as $St \to 0$, the relative velocity $\mathbf{W} \to 0$, providing an ideal tracer motion. Following the basic expansion method of Longuet-Higgins [69], [70], the velocity of the particle after displacement $\Delta\mathbf{x}$ is then

$$\mathbf{V}(t) = \mathbf{U}(\mathbf{x_0} + \Delta\mathbf{x}, t) + \mathbf{W}(\mathbf{x_0} + \Delta\mathbf{x}, t), \tag{4.21}$$

which is approximated by Taylor's theorem [76] as

$$\mathbf{V}(t) = \mathbf{U}(\mathbf{x_0}, t) + (\Delta\mathbf{x}\cdot\nabla)\mathbf{U}(\mathbf{x_0}, t) + \mathbf{W}(\mathbf{x_0}, t) + (\Delta\mathbf{x}\cdot\nabla)\mathbf{W}(\mathbf{x_0}, t), \tag{4.22}$$

and simplifies by Eq. (4.20) to

$$\mathbf{V}(t)\big|_{\mathbf{x}} = \mathbf{V}(t)\big|_{\mathbf{x}_0} + \left(\Delta\mathbf{x}\cdot\nabla\mathbf{V}(t)\right)\big|_{\mathbf{x}_0}. \tag{4.23}$$

The displacement is known from the integrated velocity of the particle from the beginning of an oscillation (denoted by $t = 0$ since the flow is periodic),

$$\Delta\mathbf{x} = \int_0^t \mathbf{V}\,\mathrm{d}t\,. \tag{4.24}$$

Time-averaging equation (4.23) over one period provides the average velocity of an inertial particle

$$\left\langle \mathbf{V} \right\rangle\Big|_{\mathbf{x}} = \left\langle \mathbf{V} \right\rangle\Big|_{\mathbf{x}_0} + \left\langle \Delta\mathbf{x} \cdot \nabla\mathbf{V} \right\rangle\Big|_{\mathbf{x}_0}. \tag{4.25}$$

The time-averaged initial velocity,

$$\left\langle \mathbf{V} \right\rangle\Big|_{\mathbf{x}_0} = \varepsilon^2 \, \mathbf{V}^{st}\Big|_{\mathbf{x}_0}, \tag{4.26}$$

is simply the time-invariant portion of the perturbation definition Eq. (4.6), where solutions for $\mathbf{V}^{st}$ are known from Eqs. (4.16)-(4.19). The *St*-dependent inertial Stokes drift correction is

$$\left\langle \Delta\mathbf{x} \cdot \nabla\mathbf{V} \right\rangle\Big|_{\mathbf{x}_0} = \left(1 + 3\left(\eta - 1\right)\sqrt{\eta}\, St^{3/2} - \left(7\eta^2 - 8\eta + 1\right) St^2 + \text{H.O.T.}\right)\left\langle \mathbf{V}^{SD} \right\rangle\Big|_{\mathbf{x}_0}, \tag{4.27}$$

where the multiplying factor

$$\left\langle \mathbf{V}^{SD} \right\rangle = -\frac{1}{2}\varepsilon^2 \left(U_x^s \frac{\partial \mathbf{U}^c}{\partial x} - U_x^c \frac{\partial \mathbf{U}^s}{\partial x} + U_y^s \frac{\partial \mathbf{U}^c}{\partial y} - U_y^c \frac{\partial \mathbf{U}^s}{\partial y} \right) \tag{4.28}$$

is the traditional non-inertial Stokes drift velocity determined by Longuet-Higgins for this flow [69]. As Stokes number $St \to 0$, our inertial Stokes drift analysis reduces to the standard non-inertial analysis,

$$\left\langle \mathbf{V} \right\rangle\Big|_{\mathbf{x}} = \left\langle \mathbf{U} \right\rangle\Big|_{\mathbf{x}_0} + \left\langle \mathbf{V}^{SD} \right\rangle\Big|_{\mathbf{x}_0}. \tag{4.29}$$

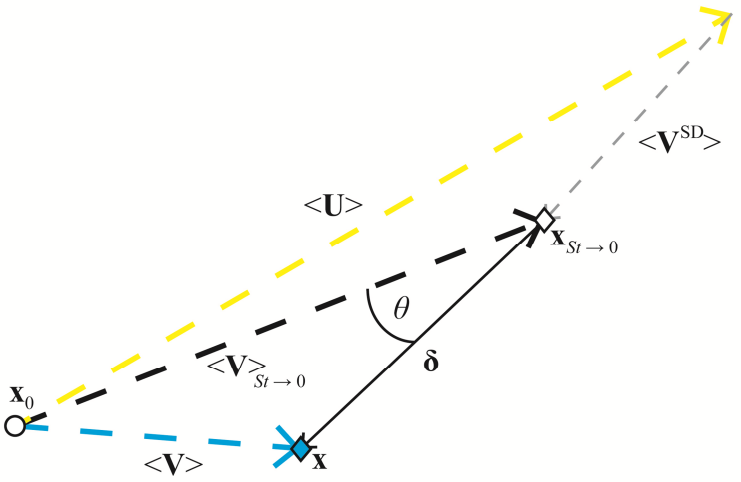

Figure 19. Vector projection from initial starting location $\mathbf{x}_0$ (open circle) of mean fluid velocity $\langle\mathbf{U}\rangle$ (yellow dashed line), non-inertial Stokes drift velocity $\langle\mathbf{V}^{SD}\rangle$ (gray dashed line), ideal tracer velocity $\langle\mathbf{V}\rangle_{St\to 0}$ (black dashed line) projected to final location $\mathbf{x}_{St\to 0}$ (open diamond), interial particle velocity $\langle\mathbf{V}\rangle$ (cyan dashed line) projected to final location $\mathbf{x}$ (cyan diamond), deviatory velocity $\boldsymbol{\delta}$ (solid black line), and angle of deviatory vector θ.

In Figure 19, a diagram of the starting location, final location, and relevant velocity vectors is shown. Summing the average fluid $\langle\mathbf{U}\rangle$ and Stokes drift $\langle\mathbf{V}^{SD}\rangle$ velocities evaluated at the initial location $\mathbf{x}_0$ results in the average Lagrangian velocity of an ideal tracer at location $\mathbf{x}_{St\to 0}$. Similarly, we can define a deviatory vector $\boldsymbol{\delta}$ as the difference average particle velocity $\langle\mathbf{V}\rangle_{St\to 0}$ and the average inertial particle $\langle\mathbf{V}\rangle$ velocity at location $\mathbf{x}$. From the solutions generated above in Eqs. (4.16)-(4.19) and (4.27), we find that the leading order contributions from inertia for deviation from ideal tracer motion is

$$\boldsymbol{\delta} = \tfrac{3}{2}\eta\, St\left\langle \mathbf{U}\cdot\nabla\mathbf{U}\right\rangle\Big|_{\mathbf{x}_0} + \text{H.O.T.}. \tag{4.30}$$

Eulerian flow modeling

The generalized class of flows analyzed above includes steady viscous streaming generated when a fluid is oscillated with small amplitude s and frequency ω past obstructions of characteristic length a. In particular, we are interested in the transport of particles by viscous streaming flows when the oscillating Reynolds number $Re = \varepsilon\omega a^2/\nu$ and streaming Reynolds

number $Re_s = \varepsilon^2 \omega a^2/\nu$ are small or comparable to unity. Particles in these flows have Stokes numbers of the form

$$St = \frac{2\varepsilon\,\omega\, a^2 \varphi^2}{9\eta\nu}, \tag{4.31}$$

where $\varphi = b/a$ is the particle-to-obstruction length ratio. Based on previous experimental work, steady streaming flow in the mid-plane of the microfluidic device we call hydrodynamic tweezers is well described by a two dimensional flow field, so that is what we analyze here [38]. The stream function form of the Navier-Stokes equation for incompressible Newtonian flow,

$$\frac{\partial \nabla^2 \psi}{\partial t} + \frac{\partial \psi}{\partial y}\frac{\partial \nabla^2 \psi}{\partial x} - \frac{\partial \psi}{\partial x}\frac{\partial \nabla^2 \psi}{\partial y} = \frac{\nabla^4 \psi}{M^2}, \tag{4.32}$$

describes the two-dimensional streaming flow and serves as the initial governing equation. Here, the stream function ψ is related to the Eulerian flow $\mathbf{U}(\mathbf{x}, t)$ by

$$\mathbf{U}\left(\mathbf{x}, t\right) = \left[U_x, U_y\right] = \left[\frac{\partial \psi}{\partial y}, -\frac{\partial \psi}{\partial x}\right], \tag{4.33}$$

where the stream function $\psi = \psi'/\omega a^2$, time t' has been non-dimensionalized by $t = t'\,\omega$, position $\mathbf{x}'$ has been non-dimensionalized by $\mathbf{x} = \mathbf{x}'/a$, and $M^2 = a^2\omega/\nu$ is the dimensionless frequency.

Following the approach of Bowman and Schwartz, and later Chen, the stream function is split into a primary oscillating ψ^{osc} and a steady ψ^{st} components,

$$\psi\left(\mathbf{x}, t\right) = \varepsilon\,\psi^{osc}\left(\mathbf{x}, t\right) + \varepsilon^2\,\psi^{st}\left(\mathbf{x}\right) + \text{H.O.T.}, \tag{4.34}$$

where higher order terms (H.O.T.) have been neglected [39], [89]. Using this approach leads to a fast analytic-numeric solution to the oscillating and steady components of flow, to the order of approximation used here [89]. Similar to above, the oscillating portion of the flow are decomposed into cosine $\psi^c(\mathbf{x})$ and sine $\psi^s(\mathbf{x})$ components that describe the leading order oscillations,

$$\psi^{osc}(\mathbf{x},t) = \psi^{c}(\mathbf{x})\cos t + \psi^{s}(\mathbf{x})\sin t\,, \tag{4.35}$$

resulting in a final perturbed stream function form of,

$$\psi(\mathbf{x},t) = \varepsilon\left(\psi^{c}(\mathbf{x})\cos t + \psi^{s}(\mathbf{x})\sin t\right) + \varepsilon^{2}\psi^{st}(\mathbf{x})\,. \tag{4.36}$$

Applying to Eq. (4.32), results in governing equations at $O(\varepsilon)$,

$$M^{2}\nabla^{2}\psi^{s} = \nabla^{4}\psi^{c}, \tag{4.37}$$

and

$$M^{2}\nabla^{2}\psi^{c} = -\nabla^{4}\psi^{s}. \tag{4.38}$$

The steady equation at $O(\varepsilon^2)$ is

$$\nabla^{4}\psi^{st} = \frac{M^{2}}{2}\left(\frac{\partial\psi^{c}}{\partial y}\frac{\partial\nabla^{2}\psi^{c}}{\partial x} - \frac{\partial\psi^{c}}{\partial x}\frac{\partial\nabla^{2}\psi^{c}}{\partial y} + \frac{\partial\psi^{s}}{\partial y}\frac{\partial\nabla^{2}\psi^{s}}{\partial x} - \frac{\partial\psi^{s}}{\partial x}\frac{\partial\nabla^{2}\psi^{s}}{\partial y}\right). \tag{4.39}$$

Numerical solutions of the coupled linear Eqs. (4.37)-(4.39) was performed using COMSOL Multiphysics 3.5a by the method of Chen [39]. COMSOL numerically solves governing physics utilizing finite-element method integration across user-defined geometries and boundary-conditions. Quartic polynomial functions were used as basis functions. Simulation geometry was defined as in Figure 33. Here, a center cell in an array of cylindrical posts was modeled with horizontal oscillations using specific symmetry conditions for the boundaries: periodic Neumann conditions was set at the left and right walls; the cosine stream function of top and bottom boundaries was to a difference of $\psi^{c} = p/2$, with no net flux and no vorticity defined otherwise. An automatic mesh was generated with advancing front triangular elements and was further refined to obtain a mesh-independent converged solution. The mesh-independent converged solution was tested by computing boundary integrals at the left and right boundaries and checking for zero net flow. The mesh consisted of 130,000 triangular elements with a maximum element size of $0.0165a$ in the principal investigation area ($0 \le x \le 2.5a$, $0 \le y \le 2.5a$). Steady

streaming eddies can be seen from the contours of steady Eulerian stream function plotted in Figure 33. Cellular flow structure shows the left and right counter-rotating eddies.

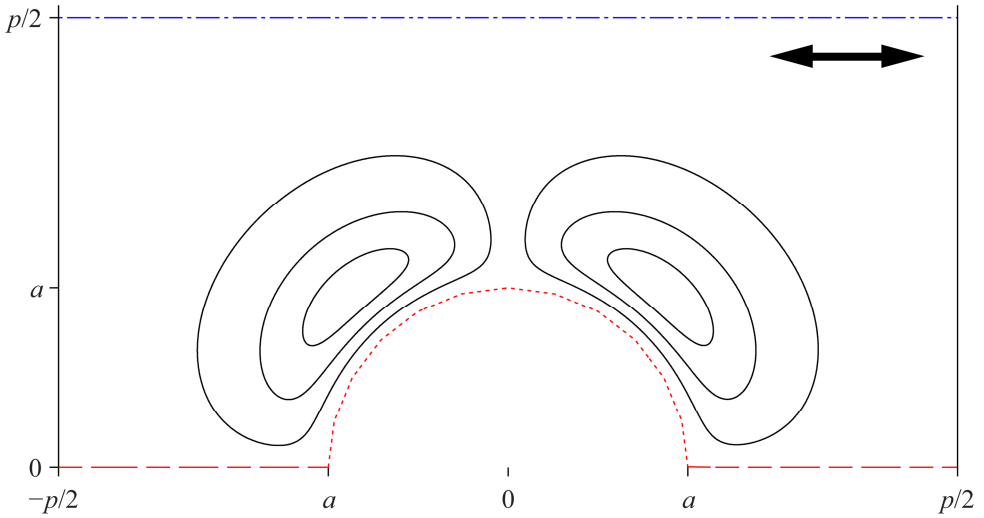

Figure 20. Symmetry geometry used in simulation of array of cylindrical posts. Contours are shown for the stream function with dimensionless oscillation frequency $M = 9.1$, pitch distance $p = 2.5a$, and oscillations occurring horizontally. Red dotted curve indicates solid post boundary; red dashed line and blue dash-dot-dash lines are symmetry conditions indicating no net flux and no vorticity separated by cosine stream function difference of $p/2$. Solid black boundaries (left and right) are periodic no net flux and no vorticity symmetry conditions.

Results and discussion

Visualizing inertial particle motion

Lagrangian paths, denoted $\mathbf{X}(t; \mathbf{x})$, for a non-inertial tracer are found by numerically solving

$$\frac{d\mathbf{X}(t; \mathbf{x})}{dt} = \mathbf{U}(\mathbf{x}, t) \tag{4.40}$$

over a single oscillation cycle (i.e. period of 2π) with a numeric Runge-Kutta(4,5) function method in MATLAB (The Mathworks, Inc.), where $\mathbf{U}(\mathbf{x}, t)$ is defined by Eqs. (4.5) and (4.33) from the stream function components known through the COMSOL solutions described previously. In Figure 21, streaming eddies around a dimesionalized obstruction post of $a = 25$ μm can be seen from the contours of steady stream function ψ. Three Lagrangian paths are computed from the Eulerian flow field with $\varepsilon = 0.1$ and are shown as black semicircles labeled

A, B, and C. The non-inertial tracers move in a clockwise direction and traverse nearly a full circle, but do not, in general, close back on themselves. The tracer path is not closed because there is a mean flow caused by steady streaming flow (i.e. mean flow at a point) and Stokes drift driven by the integrated flow non-uniformity experienced while tracing out the particle path (i.e. drift caused by the path of the particle). At each location, the flow field has significantly different properties. Location A shows nearly completely lateral motion, while B and C show increasing vertical displacement.

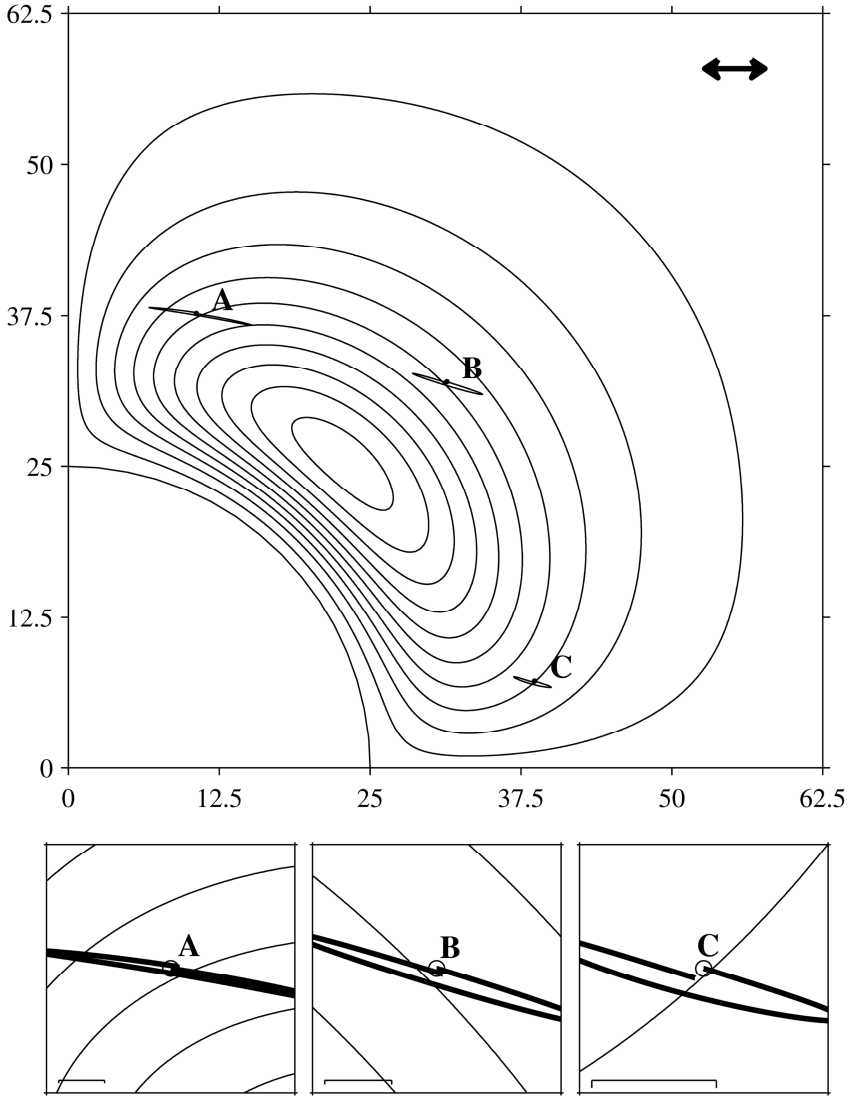

Figure 21. Lagrangian paths of 3 ideal tracers, designated points A, B, and C, with contours of Eulerian steady stream function ψ for $M = 9.1$ and horizontal oscillation direction. Above: Circular obstruction boundary is $x^2 + y^2 = a^2 = 25^2$ μm^2. Below: A, B, and C points are shown enlarged with scale bars $0.05a$.

In Figure 22, point A from Figure 21 is further analyzed and compared to inertial particle motion. In each of the subplots, the path of an ideal non-inertial tracer is plotted as a thick black curve superimposed over contours of the local steady stream function. Inertial particle paths are plotted on top of ideal tracer paths, shown as circular markers placed in equal spaced time increments ($\Delta t = \pi/25$). These are computed as with Eq. (4.40), but where the RHS $\mathbf{U}(\mathbf{x}, t)$ has been replaced by the inertial particle velocities $\mathbf{V}(t)$. The filled circular marker denotes the

starting location, the filled square denotes the mid-time point in the oscillation, and the filled diamond is the final location after 2π. For the top image in Figure 22, a weakly inertial particle is shown with φ = 0.04 and η = 0.95 corresonds to the small polystyrene tracers we use in experimental work when trying to assess the non-inertial Lagrangian flow field [42]. Thus, the small Stokes number (St = 0.003) of particles in our fluid imaging experiments closely follow the ideal non-inertial tracer motion.

In the middle image in Figure 22, the path for a larger heavy particle (such as a glass bead, φ = 0.2 and η = 0.4) is plotted in comparison to an ideal non-inertial tracer path. The corresponding Stokes number (St = 0.185) indicates substantially more particle interia, and we therefore see evidence of deviation between the particle motion and the ideal tracer. As the inertial particle (filled black circle) declerates to round the first bend, inertia propels the particle farther than the ideal tracer. After the bend, the retarded acceleration of inertial particle means the particle at its mid-time in the oscillation (filled black square) has not moved as far as the particle in the top of Figure 22, where inertia is negligible. The fluid then reverses before the inertial particle has gone as far as an ideal tracer, rounds the second bend inside the ideal tracer path, and the final location (filled black diamond) is different from the final location of an ideal tracer.

In the bottom image in Figure 22, the path of a large light particle (such as a hollow glass bead, φ = 0.2 and η = 7.1) is shown. The Stokes number of this particle (St = 0.01) indicates a weakly inertial particle. The path very nearly follows that of an ideal tracer around the first bend, with the mid-time point of the path fairly closely aligned with that of the top image. As the particle rounds the second bend the integrated deviations from an ideal tracer become evident. The final location of the particle appears to be deviated from the final location of a tracer, and is

close to that of the large heavy particle. The final and starting locations will be analyzed further in an enlarged image in Figure 23.

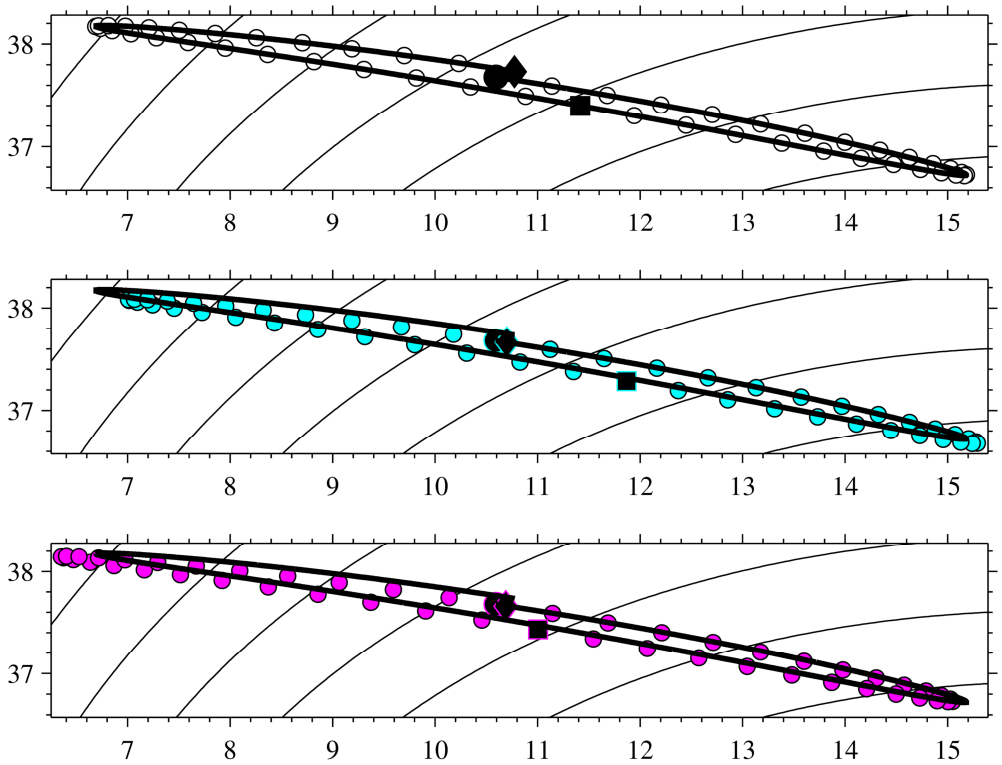

Figure 22. Lagrangian paths for a single oscillation of ideal tracer at point A with contours showing the Eulerian steady stream function. Each plot shows the same starting location and an ideal tracer path (black line). Superimposed is the path of an inertial particle shown as 50 cirular markers separated by time $\pi/25$ with $\varphi = 0.04$, $\eta = 0.95$ (top), $\varphi = 0.2$, $\eta = 0.4$ (middle), and $\varphi = 0.2$, $\eta = 7.1$ (bottom). Starting location ($t = 0$) is shown by a filled black circle, the midpoint ($t = \pi$) shown by a filled square, and end of oscillation ($t = 2\pi$) shown by a filled diamond. Numbers denote position in microns (see Figure 3).

In Figure 23, an enlarged view in the region around the starting and ending points of particle motion from Figure 22 is shown. The solid thick black line shows the beginning and ending of the Lagrangian path of an ideal tracer. The final locations of the three different inertial particles are shown as black diamonds from Figure 22. From these alone, we can see that the small ($\varphi = 0.04$), weakly inertial fluid tracer has nearly the same end point as an ideal tracer, but the larger particles ($\varphi = 0.2$) are deviated signficantly from this location. The yellow dashed line shows the projection of the time-average fluid velocity, projecting only the steady streaming drift velocity

(i.e. the Eulerian projection) as the initial velocity to compute a position one period later (see. The black dashed line shows the time-averaged ideal tracer velocity projection calculated from Eq. (4.29) including the usual Stokes drift computation accounting for the gradient field around the initial location. The black dashed line aligns correctly with the actual end point of the Lagrangian path and the final location of the weakly inertial fluid tracer. The cyan and magenta dashed lines correspond to the time-averaged inertial particle velocity projections computed from Eq. (4.25) for the large heavy and light particles defined previously. These both correspond closely with the final locations found by computing a full Lagrangian path (filled diamonds).

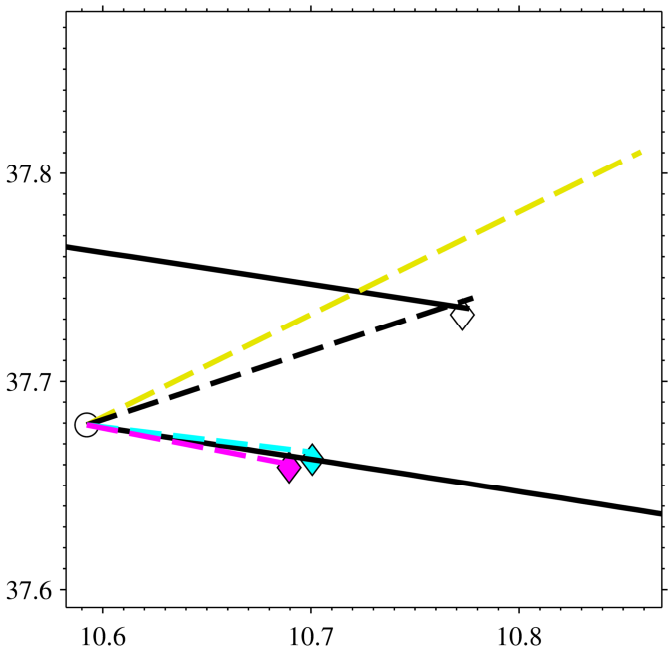

Figure 23. Enlarged view of start and final points for a Lagrangian path at location A with a single Eulerian steady stream function contour shown (thin black line). Four Lagrangian paths are computed from the filled black circle: the thick black line shows the path of an ideal tracer; black, cyan, and magenta filled diamonds show the final particle position for $\varphi = 0.04$, $\eta = 0.95$ (black), $\varphi = 0.2$, $\eta = 0.4$ (cyan), and $\varphi = 0.2$, $\eta = 7.1$ (magenta). Dashed lines show the time-averaged projection from the starting location: steady drift only (yellow); non-inertial Stokes drift (black); inertial Stokes drift for $\varphi = 0.2$, $\eta = 0.4$ (cyan), and inertial Stokes drift for $\varphi = 0.2$, $\eta = 7.1$ (magenta).

We continue the analysis by looking at inertial particle trajectories at locations B in Figure 24. The motion traced by the ideal tracer (solid black lines) appears more elliptical than with

underlying flow field and steady drift are producing motion down and to the right. As before, the top image in Figure 24 shows the path of a weakly inertial fluid tracer (St = 0.003) follows the path of an ideal tracer closely, with no deviation evident in the paths. In the cases of large heavy (St = 0.185, middle) and light (St = 0.01, bottom), deviation throughout the oscillatory motion is evident. The lag experienced in the particle motion is cumulative, to the point where even the light particle with relatively low Stokes number (St = 0.01, bottom) shows increased stopping and turning distances (top left of bottom image). For this location, however, the final positions of the inertial particles do not appear to deviate substantially from the ideal tracer motion.

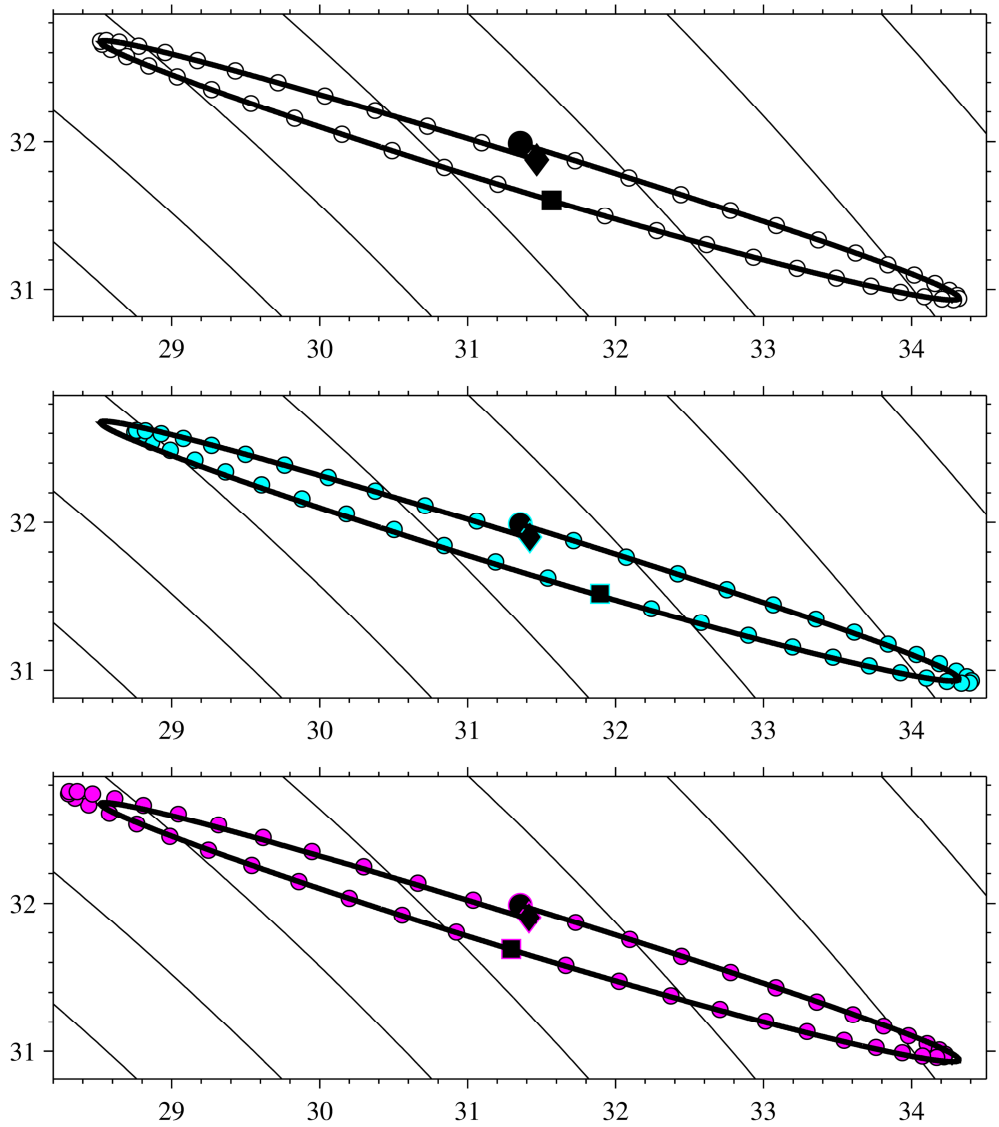

Figure 24. Lagrangian paths for a single oscillation of ideal tracer at point B with contours showing the Eulerian steady stream function. Each plot shows the same starting location and an ideal tracer path (black line). Superimposed is the path of an inertial particle shown as 50 cirular markers separated by time $\pi/25$ with $\varphi = 0.04$, $\eta = 0.95$ (top), $\varphi = 0.2$, $\eta = 0.4$ (middle), and $\varphi = 0.2$, $\eta = 7.1$ (bottom). Starting location ($t = 0$) is shown by a filled black circle, the midpoint ($t = \pi$) shown by a filled square, and end of oscillation ($t = 2\pi$) shown by a filled diamond.

When observing a close-up of the starting location B in Figure 25, we see that the both the end locations of inertial Lagrangian paths (diamond markers) and the time-averaged projections based on the analysis of Eq. (4.25) agree well. In this location, however, we see much less deviation caused by inertial than in the previous location (i.e. $\boldsymbol{\delta}$ is smaller). We also see the angle

of deviation, θ, to be much reduced, indicating a variety of flow field gradients are different at this location.

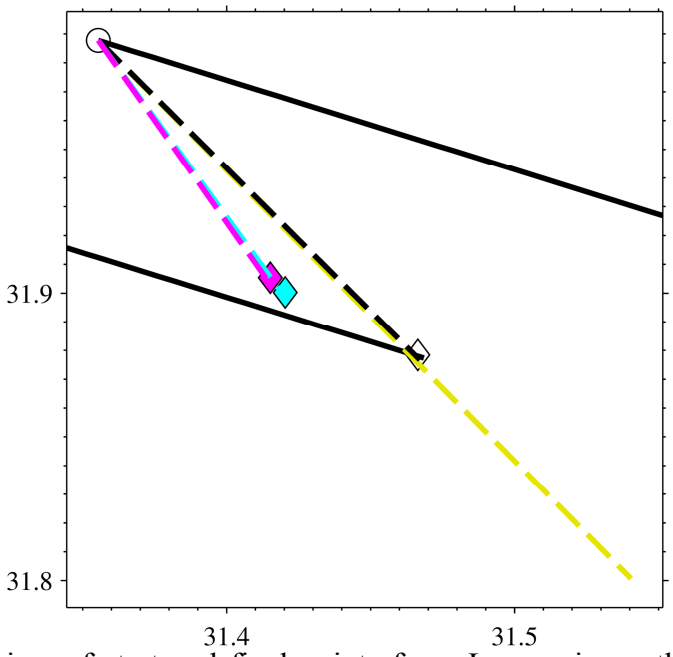

Figure 25. Enlarged view of start and final points for a Lagrangian path at location B with a single Eulerian steady stream function contour shown (thin black line). Four Lagrangian paths are computed from the filled black circle: the thick black line shows the path of an ideal tracer; black, cyan, and magenta filled diamonds show the final particle position for $\varphi = 0.04$, $\eta = 0.95$ (black), $\varphi = 0.2$, $\eta = 0.4$ (cyan), and $\varphi = 0.2$, $\eta = 7.1$ (magenta). Dashed lines show the time-averaged projection from the starting location: steady drift only (yellow); non-inertial Stokes drift (black); inertial Stokes drift for $\varphi = 0.2$, $\eta = 0.4$ (cyan), and inertial Stokes drift for $\varphi = 0.2$, $\eta = 7.1$ (magenta).

In Figure 26, location C from Figure 21 is analyzed with same inertial particles overlayed by an ideal tracer path. Again, we see that the weakly inertial particle ($St = 0.003$) follows an ideal path closely, showing no discernible deviation at this magnification level. In the cases of large heavy ($St = 0.185$, middle), the particle is lagging the motion of the ideal tracer and completes the first turn much slower. In addition, it is forced to make the second turn before moving as far as the ideal tracer. The light inertial particle ($St = 0.01$, bottom), shows similar deviation as with the previous locatinos as well, with the lag of inertia appearing only signficatnly at the the

second bend in the the oscillatory motion. For both of the larger inertial particles, the final location after one period appears deviated from ideal motion.

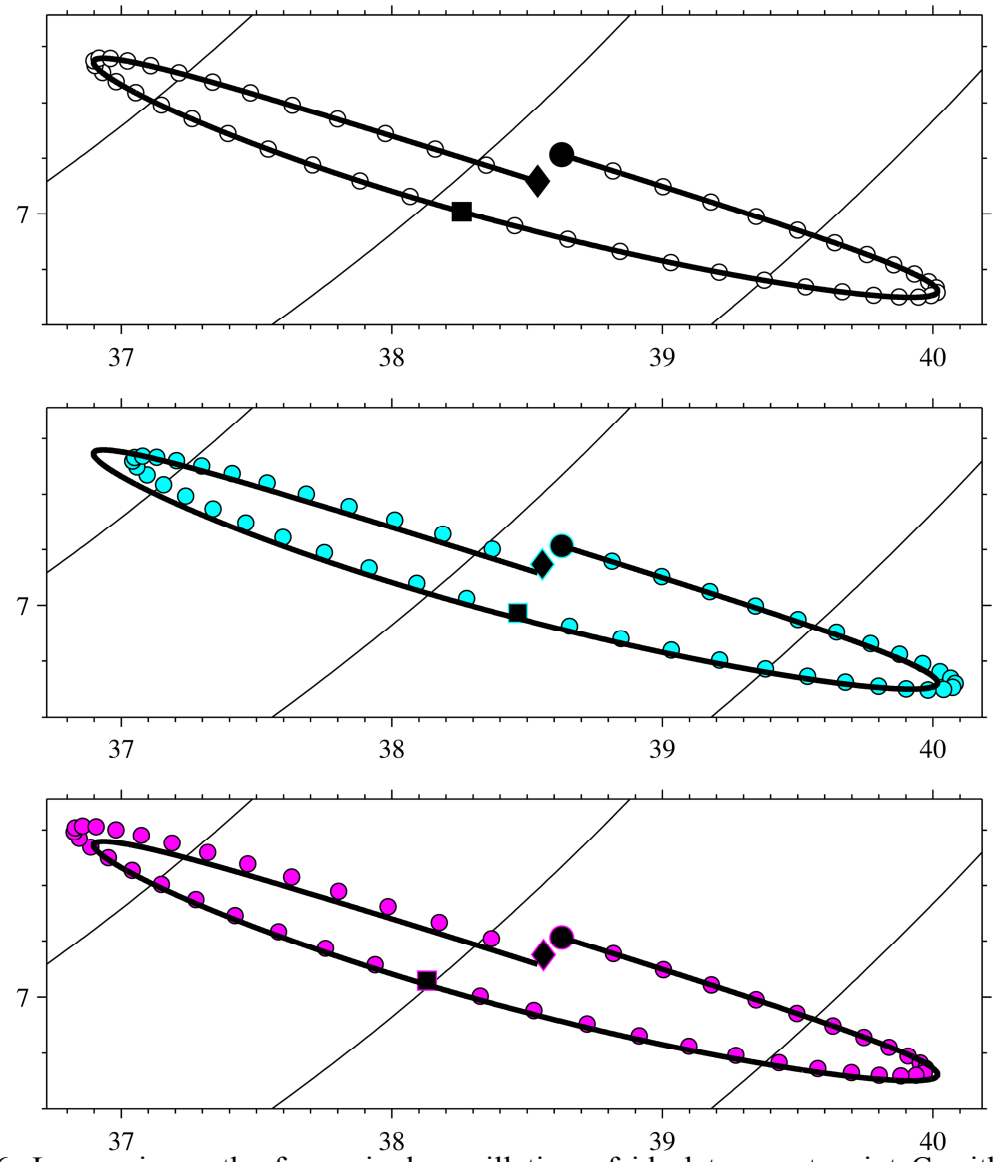

Figure 26. Lagrangian paths for a single oscillation of ideal tracer at point C with contours showing the Eulerian steady stream function. Each plot shows the same starting location and an ideal tracer path (black line). Superimposed is the path of an inertial particle shown as 50 cirular markers separated by time $\pi/25$ with $\varphi = 0.04$, $\eta = 0.95$ (top), $\varphi = 0.2$, $\eta = 0.4$ (middle), and $\varphi = 0.2$, $\eta = 7.1$ (bottom). Starting location ($t = 0$) is shown by a filled black circle, the midpoint ($t = \pi$) shown by a filled square, and end of oscillation ($t = 2\pi$) shown by a filled diamond.

A magnified view of location C is shown in Figure 27. Here, close corespondance is again shown between the time-averaged velocity projections and the final Lagrangian path positions after one period of oscillatory motion. In this location we see a very shallow angle, θ, of inertial

deviation, with a low overall magnitude of displacement. We see for all of the above figures that our time-averaged inerterial particle velocity projections match well with computing full Lagrangian paths.

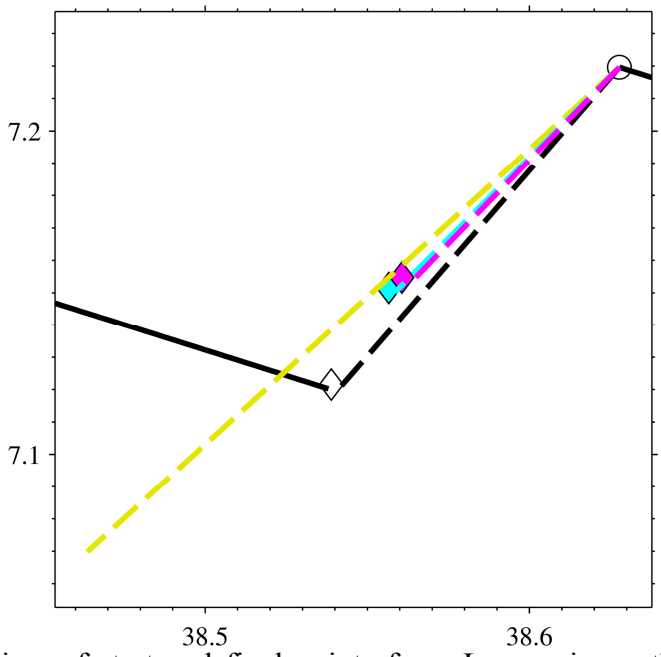

Figure 27. Enlarged view of start and final points for a Lagrangian path at location C with a single Eulerian steady stream function contour shown (thin black line). Four Lagrangian paths are computed from the filled black circle: the thick black line shows the path of an ideal tracer; black, cyan, and magenta filled diamonds show the final particle position for $\varphi = 0.04$, $\eta = 0.95$ (black), $\varphi = 0.2$, $\eta = 0.4$ (cyan), and $\varphi = 0.2$, $\eta = 7.1$ (magenta). Dashed lines show the time-averaged projection from the starting location: steady drift only (yellow); non-inertial Stokes drift (black); inertial Stokes drift for $\varphi = 0.2$, $\eta = 0.4$ (cyan), and inertial Stokes drift for $\varphi = 0.2$, $\eta = 7.1$ (magenta).

Analysis of inertial deviations

As it was pointed out in Figure 33, the deviatory vector **δ** represents the deviation from ideal tracer motion due to inertial of a particle. Equation (4.30) shows the term $\eta\, St$ appearing as the leading order contribution from inertial. Noticing the definition of Stokes number (4.31), we see through subsitution of a dimensionless frequency and rearrangement that

$$\eta\, St = \tfrac{2}{9}\varepsilon M^2 \varphi^2, \tag{4.41}$$

where $\tfrac{2}{9}\varepsilon M^2$ represents a constant for a given set of flow field conditions. From this, it is expected that the leading order inertial effects depend predominantly on the square particle size

ratio, φ. To generalize this, computations over a range of η and St were performed, effectively adjusting particle size from a range of $\varphi = 0.001 - 0.2$, while parametrically sweeping the density of the particle from $\eta = 0.4 - 7.1$. In Eq. (4.41), time-averaged inertial particle and ideal tracer velocities were projected as in Eq. (4.23) (for the given paramedic sweep described) and Eq. (4.25) (for the time-averaged ideal tracer velocity). From these projections, the magnitude of the deviatory vector $\boldsymbol{\delta}$ and angle from ideal tracer motion θ were computed.

In Figure 28, the results of the computations are plotted for location A. At low $\eta \cdot St$ (i.e. small particle sizes), the projected locations for an inertial particle and an ideal tracer are identical, with no significant deviation between the two vectors found. As the product $\eta \cdot St$ is increased, the magnitude of the deviarotory vector grows linearly as predicted by Eq. (4.30). As the product is increased further, however, contributions from the higher order terms begin to to affect the linearity of the deviatory magntidue curve. This is easily explained by the higher order terms in Eqs. (4.19) and (4.27). These deviations from linear behavior are not observed at location A.

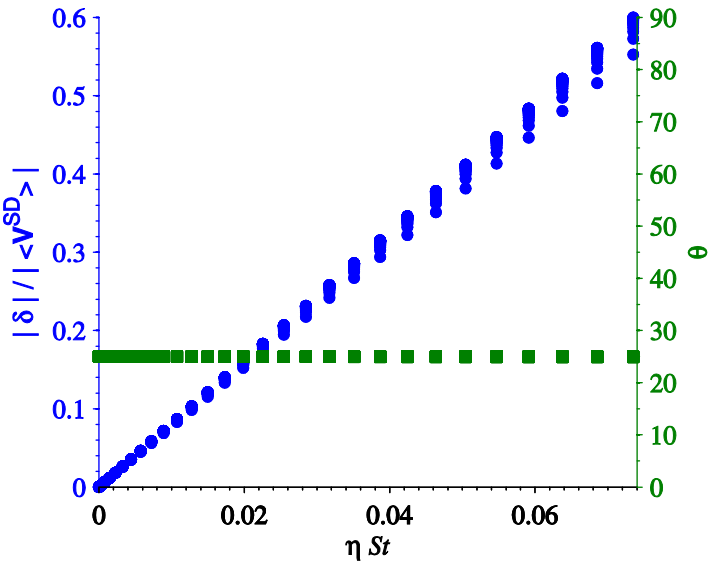

Figure 28. Angle and magnitude of deviation vector of inertial Stokes drift from non-inertial Stokes drift at location A. Angle is plotted with green points (clockwise measurement). Blue points plot the normalized magnitude of the deviation vector.

In Figure 29, point B from Figure 21 is also analyzed. Here, we the same linear increasing deviatory magnitude and increasing divergence from linear behavior. The divergence in the case at the highest η *St* product is signficantly greater for this location. In addition, the angle of the deviatory vector is again mostly constant throughout the range of values tested, though it begins deviating from its average value much sooner than the magnitude. Furthermore, the range of angle values calculated seems to reach a maximum spread and then stays constant through the range of product $\eta \cdot St$.

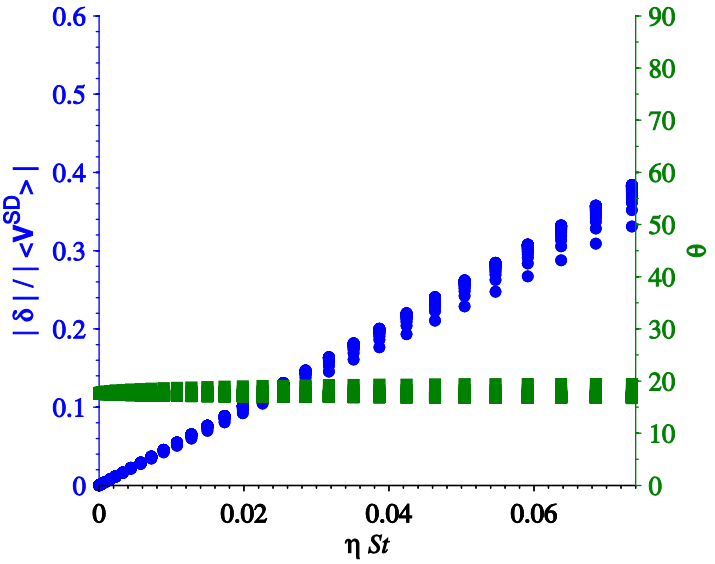

Figure 29. Angle and magnitude of deviation vector of inertial Stokes drift from non-inertial Stokes drift at location B. Angle is plotted with green points (clockwise measurement). Blue points plot the normalized magnitude of the deviation vector.

In Figure 30, point C from Figure 21 is analyzed, and the constant angle with increasing magnitude of the deviatory vector is once again evident. The divergence of both magnitude and angle shows similar behavior to the other two locations analyzed, leading us to the conclusion that the angle of deviation from ideal tracer motion is constant for a given location and small $\eta \cdot St$. The magnitude of this deviation is comparable to the traditional Stokes drift computation that has been known to be necessary for converting an Eulerian field to Lagrangian particle measurements.

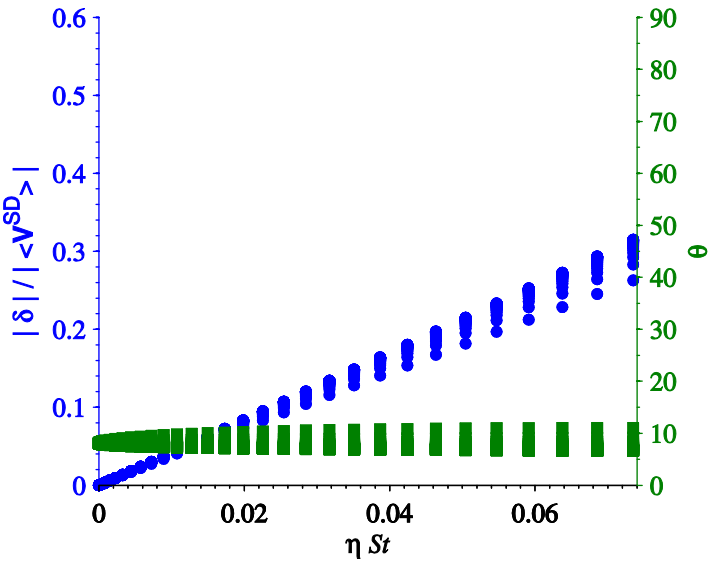

Figure 30. Angle and magnitude of deviation vector of inertial Stokes drift from non-inertial Stokes drift at location C. Angle is plotted with green points (clockwise measurement). Blue points plot the normalized magnitude of the deviation vector.

Based on the analytical expressions derived previously, given a specific η, St, and φ, the angle and magnitude of deviatory vector from ideal Stokes drift can be computed for everywhere in the flow field. In Figure 31, the magnitude of the deviatory vector normalized to the time-averaged Stokes drift velocity for $\varphi = 0.2$ and $\eta = 7.1$ is plotted. Values for the magnitude for the three locations marked in Figure 21 are shown as well, matching analysis in Figs. 10-12. The lightest shading represents a normalized magnitude > 2. The outer region with this white shading has a high overall normalized magnitude by nature of the Stokes drift magnitude being negligible in this area. The bright spot near the center of the eddy however, has significant Stokes drift magnitude, and therefore the deviatory vector magnitude is predicted to be significant here. The area surrounding the cylindrical obstruction is mostly shown with a normalized magnitude of zero, indicating little inertia effect predicted here.

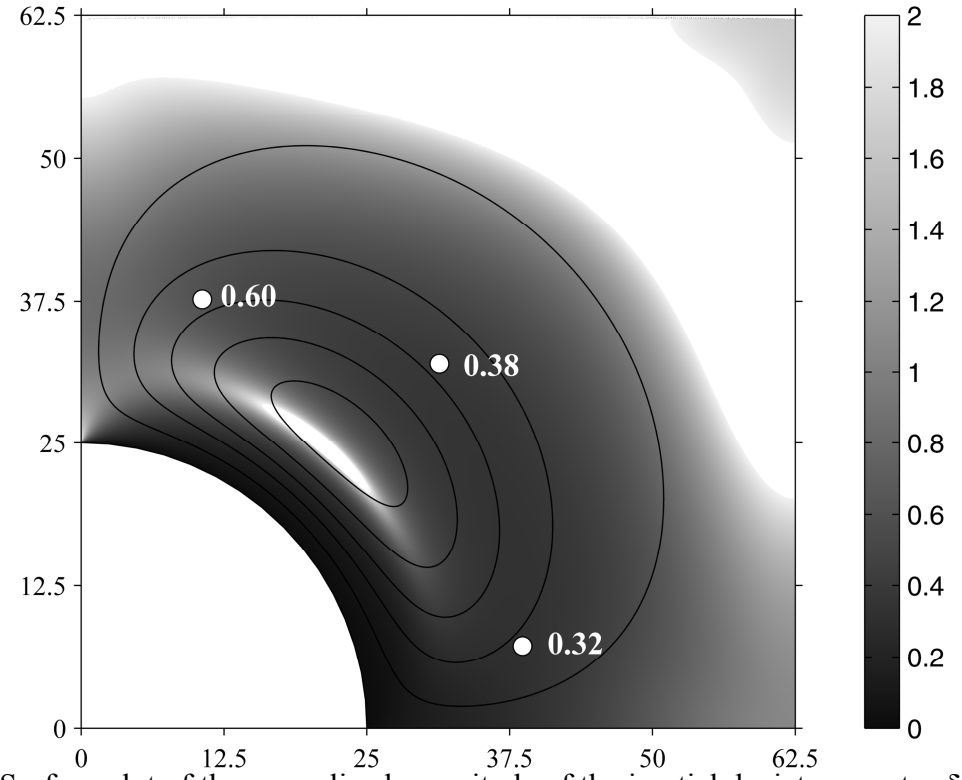

Figure 31. Surface plot of the normalized magnitude of the inertial deviatory vector $\boldsymbol{\delta} / \langle \mathbf{V}^{SD} \rangle$ is overlaid on contours for the steady stream function. Values for the locations A, B, and C are plotted for $\varphi = 0.2$ and $\eta = 7.1$. Regions plotted in white are for normalized magnitudes > 2.

In Figure 32, the angle of the deviatory vector θ is plotted for $\varphi = 0.2$ and $\eta = 7.1$, though previous plots predict a nearly constant angle for a given location regardless of characteristics of the inertial particle. In addition, the angles of the three locations are overlaid, matching results from Figs. 10-12. For much of the flow field, the deviatory vector is aligned in approximately the same direction as the Stokes drift vector (see Figure 19). In the far region ($x > 50$; $y > 50$) numerical aberrations due to negligible deviatory and Stokes drift vector magnitudes lead to angle predictions that are less robust. A clear line can be seen in the inner eddy, showing approximately the location of the Stokes boundary layer generated from the obstruction surface. We expect our results to be not as accurate in the near neighborhood of this boundary layer due to exclusion of Faxén corrections and Saffman lift forces, which have been noted to be important for these flows in regions near rigid surfaces [95].

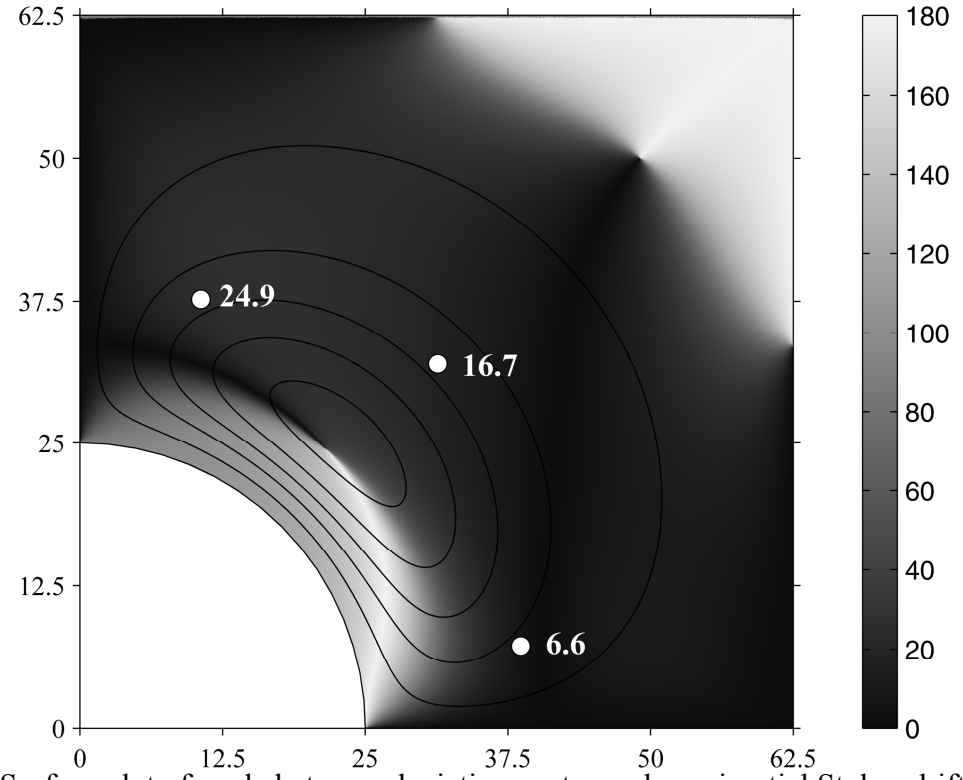

Figure 32. Surface plot of angle between deviation vector and non-inertial Stokes drift is overlaid on contours for the Eulerian steady stream function. Angle values for the locations A, B, and C are plotted for $\varphi = 0.2$ and $\eta = 7.1$.

Conclusion

The goal of this paper was to demonstrate the simplicity of the leading order contributions to the inertial deviations from ideal, non-inertial Stokes drift tracer motion. We have shown that our analytic-numeric approach to simulating steady streaming microeddy flows coupled with inertial-corrected Stokes drift analysis generates significant inertial particle path differences over single periods. Furthermore, our ability to predict these deviations using time-averaging analysis allows for whole flow field predictions of how much deviation, and in which direction, one can expect for a given inertial particle. This novel analysis is valid a wide range of oscillating flows where surface effects are not significant drivers of particle motion. Furthermore, in cases where these surface effects are needed for accurate particle trajectories [95], they may be easily added into the Maxey Riley equation to generate more robust analyses.

CHAPTER 5 || A MODEL FOR INERTIAL PARTICLE TRAPPING LOCATIONS IN HYDRODYNAMIC TWEEZERS ARRAYS

We present a model for the trapping of particles with finite inertia in the microscale viscous steady streaming flow of hydrodynamic tweezers. Devices containing a square array and an offset array of cylindrical posts of radius 25 μm were fabricated. As water is oscillated at small amplitude (s < 5 μm) and audible frequency (5000 Hz), highly symmetric microeddies form causing the fluid and particles suspended in the fluid to transport through the device. We image the flows by using 0.5 μm radius fluorescent polystyrene particles, and demonstrate trapping with larger 5 μm radius polystyrene particles. The streaming flow fields are simulated numerically using a fast analytic-numeric approach, and inertial particle motion is determined using the well-known the Maxey-Riley equation for small Stokes number (St) particle motion. The St-dependent period-averaged particle velocity is used to describe the effects of inertia on particle trapping locations. We find the St-dependence of trapping location depends on the underlying symmetry of the flow. Only traps located near eddy centers are affected by particle inertia.

Introduction

The manipulation of particles and cells, and the mixing of reagents, are central operations of biological and medical microfluidic systems, as recently reviewed [18], [96]. Acoustically driven

microstreaming flows have gathered recent attention in this context [23], [40] owing to their ability to aid in mixing [41], cause vesicle lysis [30], carry-out well-mixed batch reactions [36], and separate and trap micro-objects such as particles and cells [32], [33], [37], [42]–[44]. Viscous steady streaming in an incompressible fluid of kinematic viscosity v is driven by low intensity fluid oscillations past an obstruction of characteristic dimension a. Here we are interested in fluid oscillations with low amplitude (s) and moderate frequency (ω) oscillations, such that $\varepsilon = s/a << 1$, and the streaming Reynolds number $Re_s = \varepsilon^2 \omega a^2/v$ is small or comparable to unity [45], [46]. Viscous streaming is driven by flow within the oscillating Stokes boundary layer $\delta_{AC} \sim O((v/\omega)^{1/2})$ surrounding the obstruction [48]. Based on previous experimental work, steady streaming flows of this character retain many of the key traits of a 2D flow when used in a microdevice, though 3D flow characteristics are present near the walls [38].

Analytical descriptions of the 2D viscous streaming flow for cylinders and spheres has been well-known for decades [46], [50]–[54], [61], [97]–[99]. Despite this theoretical foundation, particle transport in these flows has been limited to the motion of inertia-free ideal tracers that locally follow the flow. An ideal tracer reveals the Lagrangian reference frame motion of the fluid, and the transformation of that motion to the Eulerian frame of reference (normally used in computation) is known as Stokes drift. Interestingly, it has been shown that an ideal tracer particle displays a net time-averaged Stokes drift motion that is comparable in magnitude to the Eulerian frame steady streaming, but added to it [52], [61], [100]. In short, the Eulerian specification describes a spatial distribution of fluid velocity while the Lagrangian specification defines individual material elements that have a dynamical history [64].

Micro-objects that we may want to trap or transport in a streaming flow will have small but finite inertia that is proportional to the particle Stokes number

$$St = \frac{2U_0 b^2}{9\eta\nu a}, \tag{5.1}$$

where b is the particle radius, $U_0 = \omega s$ is a characteristic fluid velocity, η is the fluid-to-particle density ratio, and other variables have been defined. Recent work from Chong et al. provided a model for inertial motion of particles in the streaming adjacent to an oscillating infinite cylinder [95]. They adapted the particle force balance from Maxey and Riley [80] and solved it numerically to show that particles are trapped near the center of the streaming eddies. The original Maxey and Riley force balance is a dynamic equation for the velocity $\mathbf{V}$ of a rigid spherical particle in a non-uniform flow field, where the Eulerian-frame velocity is $\mathbf{U}$:

$$St\frac{\mathrm{d}\mathbf{V}}{\mathrm{d}t} = St\eta\frac{\mathrm{D}\mathbf{U}}{\mathrm{D}t} - \frac{St\eta}{2}\frac{\mathrm{d}}{\mathrm{d}t}(\mathbf{V}-\mathbf{U}) - (\mathbf{V}-\mathbf{U}) - \sqrt{\frac{9\eta St}{2\pi}}\int_{-\infty}^{t}\frac{\mathrm{d}/\mathrm{d}\tau\,(\mathbf{V}[\tau]-\mathbf{U}[\tau])}{\sqrt{t-\tau}}\mathrm{d}\tau \quad . \tag{5.2}$$

Equation (5.2) holds for weak inertia when St is small compared to unity, resulting in a small relative velocity difference between the particle and local fluid velocity. As noted in their derivation, the material derivative

$$\mathrm{D}\mathbf{U}/\mathrm{D}t = \partial\mathbf{U}/\partial t + \mathbf{U}\bullet\nabla\mathbf{U} \tag{5.3}$$

follows a fluid element while the derivative

$$\mathrm{d}\mathbf{U}/\mathrm{d}t = \partial\mathbf{U}/\partial t + \mathbf{V}\bullet\nabla\mathbf{U} \tag{5.4}$$

follows the moving particle. The distinction between these two derivatives becomes important with higher-order solutions. In the limit $St \rightarrow 0$, equation (5.2) shows that $\mathbf{V} = \mathbf{U}$, resulting in the ideal non-inertial tracer. The first correction to account for weak inertial affects occurs in terms of O*(St)*.

In this basic form of the Maxey-Riley equation, forces from the undisturbed flow field, added mass, Stokes drag and the Basset history force are included. For simplicity in our analytical results that follow, we ignore several additional terms that sometimes modify equation (5.2),

including Faxén corrections, gravitational forces, and Saffman lift forces [80]–[84], [101], [102]. These terms can be important for specific regions of a flow, for example, near solid surfaces or other highly non-uniform regions, and that can change the particle trapping dynamics, but they are generally not the dominant terms in the force balance [81]–[84]. In this work, we show some of the basic experimental traits of these flows in a microdevice, and qualitatively note some of their particle trapping traits. We then use the Maxey-Riley equation to derive the leading order inertia-corrected analytical solution for particle trapping in the class of flows we use experimentally. A specific set of experimental flow field conditions are then computed, with trap locations identified.

Methods

Microfluidic hydrodynamic tweezers device

As detailed previously [42], the Polydimethylsiloxane (PDMS) microfluidic devices are comprised of channels with height of 116 μm, width of 1000 μm, and length of 30 mm. Two piezo disks are bonded to a glass coverslip that has two ports allowing fluid to enter the device. This coverslip is bonded to the PDMS channel that makes up the device. The channels were filled with a square array of cylindrical posts of pitch p_1 = 125 μm (device 1) and an offset diamond array of cylindrical posts of pitch p_2 = 177 μm (device 2). In each array configuration, the posts span the channel height. The posts had a nominal radius a = 25 μm. Oscillatory flow of room temperature water (ρ_f = 1.00 g/cm^3, ν = 0.0095 cm^2/s) was driven by the piezo disks with frequencies up to 20,000 Hz, though typical conditions were around 5,000 Hz. The amplitude of the flow oscillations were in the range 1 μm ≤ s ≤ 5 μm. Specific details of the fabrication, *i.e.* PDMS molding from the SU8 master design, are given in [42]. Fluorescence microscopy (TE2000-U, Nikon) with 200 - 1500 ms exposure time revealed the time averaged particle

pathlines of small fluorescent polystyrene particles (Fluoresbrite® Multifluorescent Microspheres, b = 0.5 μm, ρ_p=1.05 g/cm^3, Polysciences, Inc.) that acted as ideal fluid tracers. Larger particles (Polybead® Microspheres, b = 5 μm, ρ_p = 1.05 g/cm^3, Polysciences, Inc.) were readily trapped near the center of the microeddies in the devices and were imaged using light microscopy.

Microeddy flow modeling

The stream function form of the Navier-Stokes equation for incompressible Newtonian flow,

$$\frac{\partial \nabla^2 \psi}{\partial t} + \frac{\partial \psi}{\partial y}\frac{\partial \nabla^2 \psi}{\partial x} - \frac{\partial \psi}{\partial x}\frac{\partial \nabla^2 \psi}{\partial y} = \frac{\nabla^4 \psi}{M^2}, \tag{5.5}$$

describes the two-dimensional streaming flow and serves as the initial governing equation. Here, the stream function ψ and Eulerian fluid velocity $\mathbf{U}(\mathbf{x}, t)$ are related by

$$\mathbf{U}(\mathbf{x}, t) = \left[U_x, U_y\right] = \left[\frac{\partial \psi}{\partial y}, -\frac{\partial \psi}{\partial x}\right], \tag{5.6}$$

for a given Cartesian point $\mathbf{x}$ and time t, where the stream function ψ' has been non-dimensionalized by $\psi = \psi'/\omega a^2$, time t' has been non-dimensionalized by $t = \omega t'$, position $\mathbf{x}'$ has been non-dimensionalized by $\mathbf{x} = \mathbf{x}'/a$, and $M = (a^2\omega/\nu)^{1/2}$ is the dimensionless frequency. Gravitational body forces have been neglected. Following the approach of Bowman and Schwartz (1998) and later Chen (2006), the stream function is split into primary oscillating flow ψ^{osc} and steady flow ψ^{st} components,

$$\psi(\mathbf{x}, t) = \varepsilon \psi^{osc}(\mathbf{x}, t) + \varepsilon^2 \psi^{st}(\mathbf{x}) + \text{H.O.T.}, \tag{5.7}$$

where $\varepsilon \ll 1$ and higher order terms (H.O.T.) have been neglected [39], [89]. Using this approach, a rapid analytic-numeric solution can be found for both the fast oscillating flow and slow steady flow [89]. Expanding the oscillating portion of the flow into in-phase (cosine) and out-of-phase (sine) components of motion provides the leading order stream functions,

$$\psi^{osc}\left(\mathbf{x},t\right)=\psi^{c}\left(\mathbf{x}\right)\cos t+\psi^{s}\left(\mathbf{x}\right)\sin t\ , \tag{5.8}$$

that can be combined into the final perturbation form of the flow field,

$$\psi\left(\mathbf{x},t\right)=\varepsilon\left(\psi^{c}\left(\mathbf{x}\right)\cos t+\psi^{s}\left(\mathbf{x}\right)\sin t\right)+\varepsilon^{2}\psi^{st}\left(\mathbf{x}\right). \tag{5.9}$$

Applying (2.9) to equation (5.5), provides the governing equations for the leading order oscillating flow at O(ε),

$$M^{2}\nabla^{2}\psi^{s}=\nabla^{4}\psi^{c} \tag{5.10}$$

and

$$M^{2}\nabla^{2}\psi^{c}=-\nabla^{4}\psi^{s}, \tag{5.11}$$

while the steady motion equation at O(ε^2) is

$$\nabla^{4}\psi^{st}=\frac{M^{2}}{2}\left(\frac{\partial\psi^{c}}{\partial y}\frac{\partial\nabla^{2}\psi^{c}}{\partial x}-\frac{\partial\psi^{c}}{\partial x}\frac{\partial\nabla^{2}\psi^{c}}{\partial y}+\frac{\partial\psi^{s}}{\partial y}\frac{\partial\nabla^{2}\psi^{s}}{\partial x}-\frac{\partial\psi^{s}}{\partial x}\frac{\partial\nabla^{2}\psi^{s}}{\partial y}\right). \tag{5.12}$$

Boundary conditions for these equations are described below, while no initial conditions are needed since this is limited to the steady periodic state (well after initial start-up transients have decayed).

To properly compare the time-average steady streaming Eulerian-frame computational model to Lagrangian experimental data using particle traces requires a Stokes drift-like correction. The period-averaged transformation from the Eulerian steady streaming velocity <**U**> to a Lagrangian steady streaming particle velocity <**V**> is

$$\left\langle\mathbf{V}\right\rangle=\left\langle\mathbf{U}\left(\mathbf{x}_{0}+\Delta\mathbf{x},t\right)\right\rangle=\left\langle\mathbf{U}\left(\mathbf{x}_{0}\right)\right\rangle+\left\langle\int_{0}^{t}\mathbf{U}\left(\mathbf{x}_{0}\right)dt\bullet\nabla\mathbf{U}\left(\mathbf{x}_{0}\right)\right\rangle \tag{5.13}$$

where $\left\langle\int\mathbf{U}dt\bullet\nabla\mathbf{U}\right\rangle$ is the linear approximation of Stokes drift, and bracketed quantities represent time-averaging over one period, *i.e.* period-averaging over 2π [60], [61], [69], [98]. Estimating the Lagrangian velocity to leading order yields

$$\left\langle \mathbf{V} \right\rangle = \varepsilon^2 \, \mathbf{U}^{st} + \varepsilon^2 \frac{1}{2} \left(U_x^c \frac{\partial \mathbf{U}^s}{\partial x} - U_x^s \frac{\partial \mathbf{U}^c}{\partial x} + U_y^c \frac{\partial \mathbf{U}^s}{\partial y} - U_y^s \frac{\partial \mathbf{U}^c}{\partial y} \right), \tag{5.14}$$

where the velocity component vectors $\mathbf{U}^c$, $\mathbf{U}^s$, and $\mathbf{U}^{st}$ are computed by combining (2.4) and (2.9) . From the individual velocity components, an equivalent Lagrangian steady stream function ψ^L (*i.e.* the lines tangential to the period-averaged particle velocity) is

$$\nabla^2 \psi^L = \frac{\partial \left\langle \mathbf{V} \right\rangle_x}{\partial y} - \frac{\partial \left\langle \mathbf{V} \right\rangle_y}{\partial x} . \tag{5.15}$$

This Lagrangian stream function, when computed and plotted, allows for direct comparison with the steady flow features in experimental images. Comparisons have been performed previously for a range of centered squares, diamonds, and wall cavities and protrusions [42].

Numerical computation of the governing equations (5.10)-(2.17) and (5.14)-(5.15) is performed using finite element method with COMSOL Multiphysics 3.5a (COMSOL, Inc.) with quartic polynomial basis functions by the method of [39]. Figure 33 shows the geometry, boundary conditions, and overview of the Lagrangian steady stream function ψ^L contours used to replicate steady streaming in the center of an array in the microfluidic device. Dimensionless frequency $M = 4.5$, pitches $p_1 = 5a$ and $p_2 = 7.07a$, width $w = 5a$, and length $L = 80a$ were set corresponding to the experimentally observed streaming near the center of our device when operated at a frequency $f = 5000$ Hz, posts of radius $a = 25$ μm, and pitch distances $p_1 = 125$ μm and $p_2 = 177$ μm. Flow is driven by specifying a cosine stream function difference between the top and bottom of the geometry, *i.e.* at $y = w$, $\psi^c = w$ and at $y = 0$, $\psi^c = 0$. This has the effect of specifying the total amount of flow between the top and bottom of the geometry, normalized to the width across. Because eddies form symmetrically, symmetry conditions, *i.e.* no net flux $\psi^s = \psi^{st} = 0$ and no vorticity $\nabla^2 \psi = 0$, at open fluid boundaries were imposed at intervals of w, whereas physical post wall boundaries that generate vorticity are set as no net flux, *i.e.* $\psi^s = \psi^{st} =$

0. The left and right boundaries are set as periodic no net flux conditions. An automatic mesh was generated with advancing front triangular elements and was further refined to obtain a mesh-independent converged solution. Typically, meshes consisted of around 110,000 triangular elements with a maximum element size of $0.04a$ in the principal investigation area ($-2.5a \leq x \leq 2.5a$, $0 \leq y \leq 5a$). Steady streaming eddies can be seen from the contours of steady Lagrangian stream function plotted in Figure 33. These streamlines depict an equivalent image of the flow field as would long-exposure ideal fluid tracers, as examined in further detail in the following section.

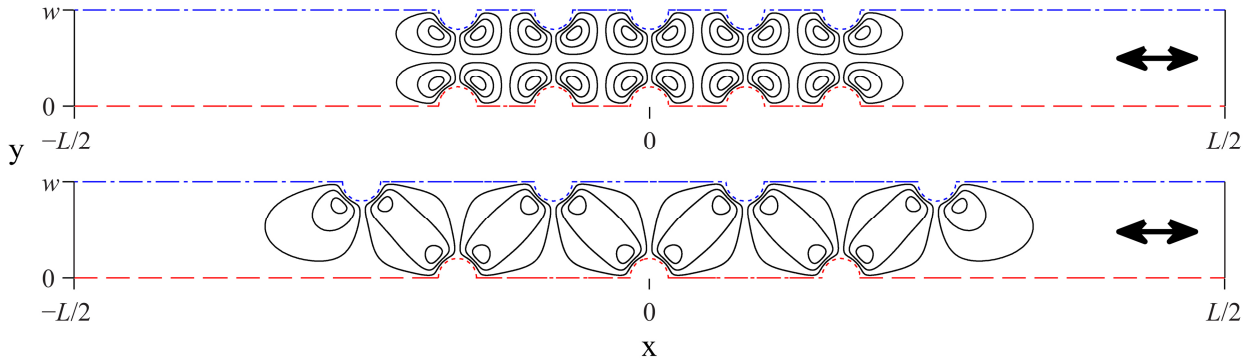

Figure 33. Symmetry geometries used in simulation of square array (top) and offset array (bottom) of cylindrical posts. Contours are shown for the Lagrangian steady stream function solution with horizontal flow oscillation of dimensionless frequency $M = 4.5$, channel width $w = 5a$, and length $L = 80a$. Blue and red lines (top and bottom of each geometry) are separated by a difference in the cosine stream function of w. Blue and red dashed lines (top and bottom, dash-dot-dash and dash-dash) lines indicate no net flux and no vorticity symmetry conditions. Blue and red dotted lines (top and bottom) indicate no net flux physical post boundaries. Left and right black boundaries indicate periodic no net flux conditions.

Results and discussion

Device flow fields and trapping

In Figure 34, the long exposure particle pathline images for both the square array and offset array devices are shown using an oscillation frequency of 5000 Hz. The fluorescent polystyrene tracer particles have a Stokes numbers of $St = 1.9 \times 10^{-4}$ for the frequency, fluids, and geometries used here. At this Stokes number, the tracers behave ideally and follow the fluid motion rather

than crossing streamlines and being collected into trapping sites. In both devices, eddies generated around posts are constrained to the symmetry set by their neighboring posts. In the case of the square array, the dividing streamlines bisects the line between each post in the direction parallel and perpendicular to the oscillating fluid motion, producing four symmetric eddies. For the offset array, we see a flow structure not previously reported in the literature, where the main eddy structure forms diagonally, at 45˚ angles to the oscillating flow, between the posts. Each diagonal eddy is comprised of two separate inner eddies adjacent to the posts and a merged outer set of streamlines producing what we call "peanut" eddies due to their appearance. In some sense, every particle is trapped by both device geometries, since the steady motion is cellular, and dividing streamlines keep each eddy from mixing with their neighbors (given the high Peclet numbers of the flow). However, we have shown before that particles with higher Stokes numbers tend to collect in trapping sites [33], [42]. We demonstrate this behavior experimentally and then use a leading order *St*-dependent analytical solution of the Maxey-Riley equation to show where the trapping locations lie.

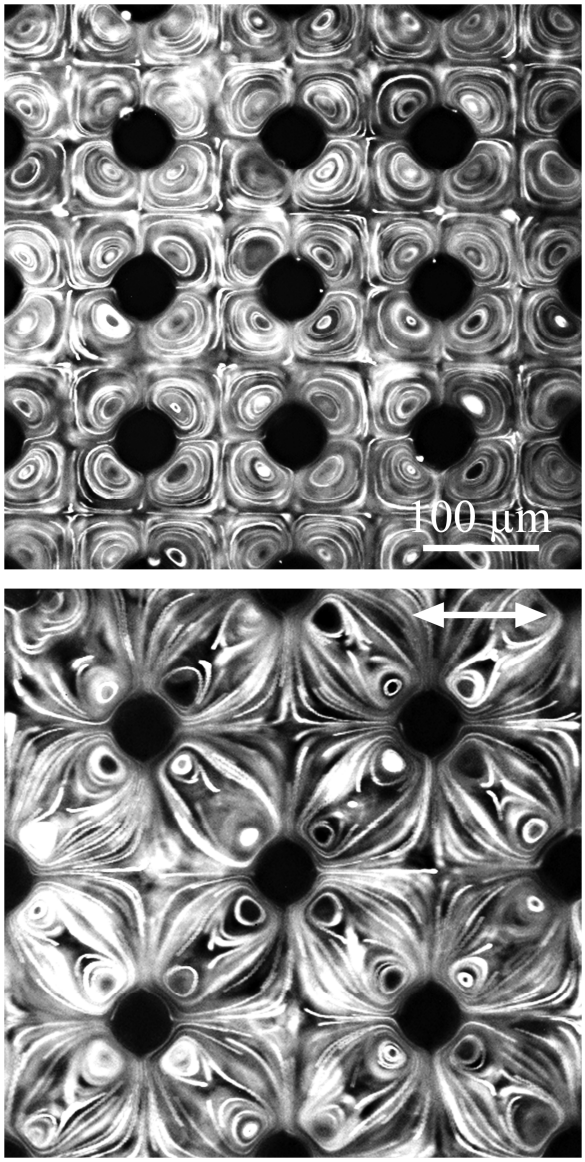

Figure 34. Long-exposure particle imaging for device 1 (top) and device 2 (bottom) for fluorescent polystyrene particles radius b = 0.5 μm and density ρ_p=1.05 g/cm^3 with horizontal oscillations of frequency f = 5000 Hz. The arrow shows the direction of the fluid oscillation, though the magnitude of the oscillation is small compared to each cylinder (the non-fluorescent black circles in each image.

Given the different nature of the two streaming flow fields seen in Figure 34, one might expect the trapping behavior to be markedly different in the different array geometries. This is born out in experiments using the larger polystyrene particles, where the Stokes number is St = 0.019 for the conditions applied here. In the square array, each cylindrical post is surrounded by four eddies that generate four stable trapping locations. The trapping locations are fixed points in

each eddy where particles tend to accumulate (when not crowded out by other particles). Figure 35 is a typical result where the hydrodynamic traps are large enough to trap multiple particles, as shown around posts labeled 1, 3, and 4-7 in the image. When multiple particles are present, the stability of trapping at a single fixed point is diminished due to particle-particle interactions that distort the flow field. We see two kinds of perturbed traps, either where doublets appear attached and rotate around the fixed point at their centers of mass, or where two or more particles orbit continuously in attraction to the trapping point near the center of the eddy, but away from the stable trap. On the other hand, single trapped particles tend to trap roughly along 45° to the direction of oscillation, in line with symmetry of the eddies and near the center of the eddies (see Figure 34). The post labeled number 9 shows what we consider the ideal case for three singly trapped particles, with little to no disturbances arising from other particles in their vicinity. Singlet trapping is this case which we seek to model, *i.e.* the Stokes dependence of trapping location for an undisturbed particle with small but finite inertia.

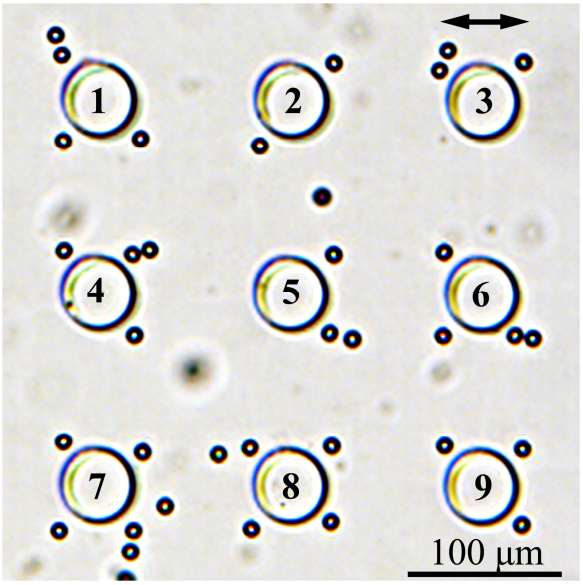

Figure 35. Trapping of polystyrene particles radius b = 5 μm and density ρ_p=1.05 g/cm^3 with horizontal oscillations of frequency f = 5000 Hz in square array (device 1).

As shown in Figure 36, the trapping situation for the offset array had some unexpected features compared to what we have observed previously [42] and with the square array. Near posts labeled 2 and 7 in Figure 36, our $St = 0.019$ particles are trapped in the strongest streaming eddies. However, unlike trapping in the square array, those near-post locations are not the most stable trapping locations found in the offset array. Instead, large particles were found to trap somewhat more stably in areas not associated with stagnation points of flow or the stronger eddies adjacent to each post, *i.e.* near posts labeled 1, 3, 4 and 5. It is important to note that none of the offset-array trapped particles displayed the same robust stability as the square-array trapping of singlets, as seen at the post denoted 9 in Figure 35. An interesting feature of the poor stability trapping in eddies adjacent to each post is that the particle motion implied the flow in the trap had some 3D characteristics that are not easily seen in the plane-view image of Figure 34. This 3D flow nature in Figure 36 became further apparent when it was observed that particles trapped near posts 2 and 7 were trapped in a different focal plane than those trapped near posts 1, 3, 4, and 5. Based on our earlier work with single cylinders of similar geometry, we would not expect this [38], implying that the 3D flow character in the offset geometry is significantly different from single cylinder or square array case. Thus, not all viscous eddy flows trap particles, even at significant particle Stokes numbers where inertia can matter. Though we have not worked with offset arrays previously, we have shown in the past that some steady streaming flows are simply not capable of stable trapping at a fixed point [42].

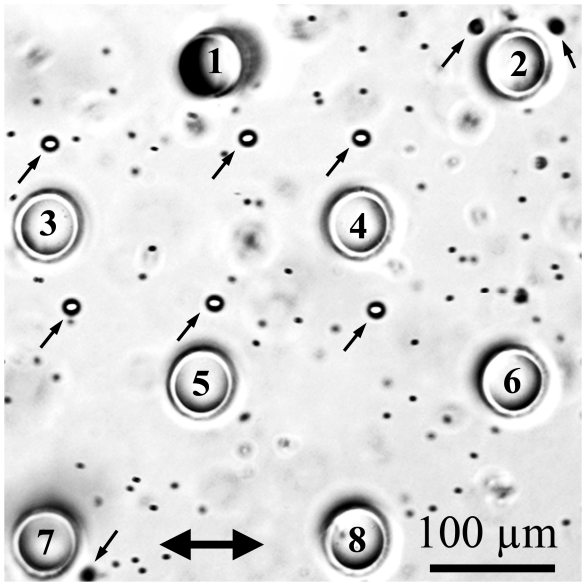

Figure 36. Trapping of polystyrene particles radius b = 5 μm and radius b = 0.5 μm and density ρ_p=1.05 g/cm^3 with horizontal oscillations of frequency f = 5000 Hz in offset array (device 2). Small arrows point to larger b = 5 μm held in traps.

Model for particle motion in hydrodynamic tweezers

A simple model for the trapping location of an inertial particle will compute the period-averaged particle velocity <**V**> and use that to identify areas in the array where motion stops, *i.e.* <**V**> = 0. For compatibility with the flow field formulation and equation (5.8), the particle velocity is defined as

$$\mathbf{V}\left(t;\mathbf{x}\right)=\varepsilon\left(\mathbf{V}^{c}\cos t+\mathbf{V}^{s}\sin t\right)+\varepsilon^{2}\,\mathbf{V}^{st}+\text{H.O.T.}\,. \tag{5.16}$$

Inserting the particle velocity (16) into equation (5.2), and applying definitions (2.4) and (2.9), allows one to solve for the O*(St)* corrections to instantaneous inertial particle velocity that account for small inertial deviations from an ideal (fluid-following) particle, *i.e.*

$$\mathbf{V}=\mathbf{U}+St\left(\varepsilon\left(\eta-1\right)\left(\mathbf{U}^{s}\cos t-\mathbf{U}^{c}\sin t\right)+\varepsilon^{2}\frac{3}{4}\eta\left(U_{x}^{c}\frac{\partial\mathbf{U}^{c}}{\partial x}+U_{x}^{s}\frac{\partial\mathbf{U}^{s}}{\partial x}+U_{y}^{c}\frac{\partial\mathbf{U}^{c}}{\partial y}+U_{y}^{s}\frac{\partial\mathbf{U}^{s}}{\partial y}\right)\right). \tag{5.17}$$

Here, as $St \rightarrow 0$, we find that a particle will have the same instantaneous velocity as the fluid. At finite St, the St-dependent correction terms have time-dependent oscillating components and time-independent steady components. We see for the physics incorporated in Eq. (5.2), the

oscillating components of particle motion reduce to the ideal tracer behavior when the density of the particle equals that of the fluid, or $\eta = 1$. This dependence on particle density ratio matches previous analytical results for particles in turbulent flows [91], [92] and wavy flows [77], [78]. For all other densities, the oscillating velocity components for the particle and fluid deviate at O(*St*). In contrast, for all densities, the steady component of particle motion in (17) deviates from the pure fluid velocity.

With knowledge of the instantaneous velocity of the particle, the period-averaged velocity is easily calculated using a similar principle as defined above in Eq. (5.13), but replacing the standard flow field **U** with the instantaneous particle velocity **V** defined in Eq. (5.17). The results of this approximation is

$$\left\langle \mathbf{V} \right\rangle = \varepsilon^2 \mathbf{U}^{st} + \varepsilon^2 \frac{3}{4} \eta St \left(U_x^c \frac{\partial \mathbf{U}^c}{\partial x} + U_x^s \frac{\partial \mathbf{U}^s}{\partial x} + U_y^c \frac{\partial \mathbf{U}^c}{\partial y} + U_y^s \frac{\partial \mathbf{U}^s}{\partial y} \right)$$

$$+ \varepsilon^2 \frac{1}{2} \left(-U_x^s \frac{\partial \mathbf{U}^c}{\partial x} + U_x^c \frac{\partial \mathbf{U}^s}{\partial x} - U_y^s \frac{\partial \mathbf{U}^c}{\partial y} + U_y^c \frac{\partial \mathbf{U}^s}{\partial y} \right) \tag{5.18}$$

which includes an inertial correction to the classical Stokes drift calculation. Equation (5.18) yields the traditional non-inertial period-averaged velocity, Equation (5.14), as $St \rightarrow 0$. In microtrapping, Equation (5.18) allows us to connect a computed Eulerian frame flow field (**U**) to the particle motion in that flow (**V**), and determine the mean motion without calculating the oscillating motion of the particle. This is computationally very efficient for a complex flow field. Particles come to rest when **<V>** = 0, and for the purposes of this paper, we use this as the definition of a trapping location. Very recently, Maxey-Riley theory has been applied to deep water waves in a similar fashion to our period-averaging approach, in order to incorporate inertial effects into the drift of particles in generalized waves [78]. The details for our inertial

Stokes drift in generalized streaming flows will be the subject of a paper currently in preparation, House and Schwartz, 2013.

Simulation results

Simulated streamlines are shown in Figure 37 for ideal (St = 0) tracers moving under the same conditions used in the square array experimental image shown in Figure 34. Shown is a unit cell with counter-rotating microeddies. Because of symmetry conditions, the unit cell represents all of the interior eddies on the array. These simulated Lagrangian streamlines nicely match the long-time experimental particle images in Figure 34, as has been shown for other geometries [42]. Computing trap locations, *i.e.* $\langle \mathbf{V} \rangle = 0$, for small microparticles allows for deeper understanding of the mechanics involved in trapping of particles. When St = 0, the particles are predicted to stop at the exact center of each eddy, and at the stagnation points in the flow field. In Figure 37, the trapping locations for St = 0.019 particles are computed and marked for the flow field conditions in Figure 35. Owing to symmetry conditions at the stagnation points, equation (18) shows that the predicted particle trapping locations at stagnation points are independent of the Stokes number. On the other hand, particles trapped in the center of the eddies are St-dependent, because the flow field is non-uniform in that region, and thus terms in Equation (5.18) can be significant.

The results for a weakly inertial particle with St = 0.019 are shown in Figure 37, where we see that the particles are predicted to trap slightly off the center of each eddy. This is most easily seen in the lower right hand eddy of Figure 37, where the actual particle size is superimposed over the trapping location. One can compare the traps seen in Figure 37 to those observed experimentally in Figure 35. It is difficult to see the offset in a device at this dimension, though off-center trapping was previously reported for trapping around single cylindrical posts in larger devices [33]. Experimentally, singlet particle trapping near the eddy center is always stable when

the particle is heavy or light compared to water, when we satisfy basic condition for 2D flow laid out previously [38]. Our theory does not let us address the particle-particle interactions we discussed in Figure 35 for eddies possessing two or more particles.

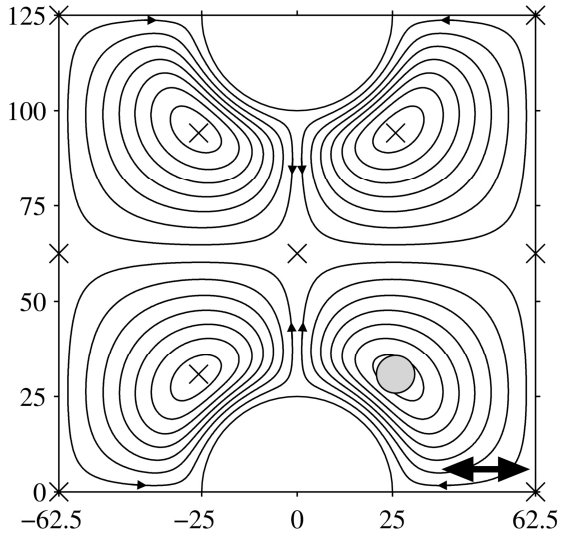

Figure 37. Contours are shown for the Lagrangian steady stream function solution in a square post array with dimensionless frequency $M = 4.5$, $p = 5a$, $L = 80a$, and oscillation occurring horizontally. Units are μm and have been scaled to the corresponding experimental device. The gray circle (lower right eddy) approximates the size of particle in a trap. The black x-marks depict other trapping locations for particles $\varphi = 0.2$, $\eta = 0.95$, and $St = 0.019$.

Simulations of ideal tracer streamlines are shown for the offset post array in Figure 38, when operating under conditions corresponding to the experimental device in Figure 34. There is good agreement between the experiment and simulation. Here the stream function contours are incremented exactly as in Figure 37, so one can see that the peanut eddies have about half the flow strength as the square array eddies. Trapping locations where we calculate $\langle \mathbf{V} \rangle = 0$ from Equation (5.18) are shown as x-marks and as a particle-sized gray disk (lower right eddy), for $St = 0.019$. As with the square array, we see there is no St-dependence for the $\langle \mathbf{V} \rangle = 0$ traps along symmetry lines, owing to the absence of the gradients found in (18). The predicted trap near the eddy center is again slightly moved from the exact center, though even less so than the square-array case.

As noted above, while we do see some evidence of trapping in the expected locations directly adjacent to posts, these eddy traps are easily disturbed and cause particles to trace 3D orbits. The predicted trapping at stagnation points in the flow, *i.e.* at (-125, 0), (0, 125), and (125, 0) in the figure, was not supported by the trapping seen in Figure 36. In addition, unexpected particles traps were found (in Figure 36) at locations not identified by our 2D trapping theory. Experiments and simulations for this type of flow have not been previously reported in the literature, and it warrants further study to fully understand the trapping behavior.

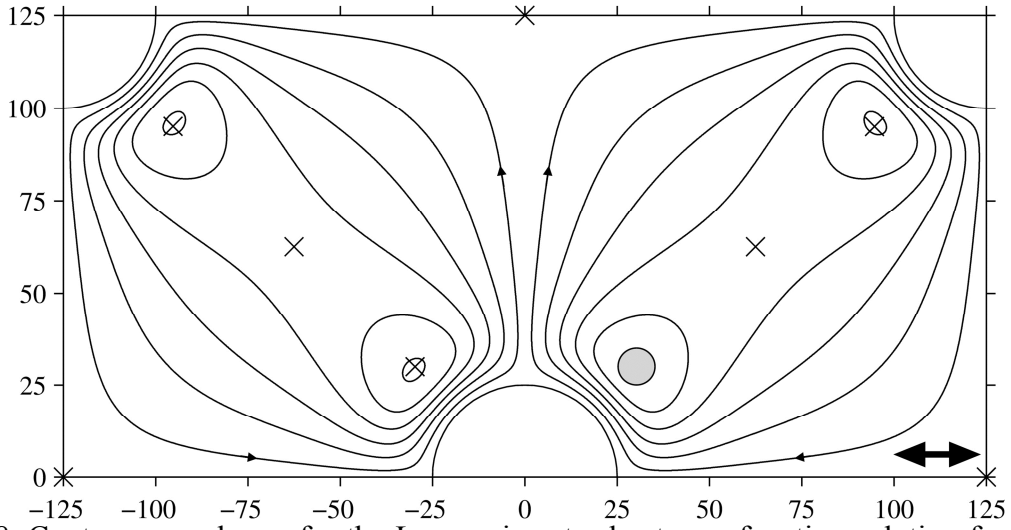

Figure 38. Contours are shown for the Lagrangian steady stream function solution for the inner cell in an offset post array with dimensionless oscillation frequency $M = 4.5$, $p = 7.07a$, $L = 80a$, and oscillation occurring horizontally. Units are μm and have been scaled to corresponding experimental device. Gray circle approximates size of particle and along with black x-marks depicts predicted trapping location for particles $\varphi = 0.2$, $\eta = 0.95$, and $St = 0.019$.

Clearly, trapping stability in these devices is worthy of further study and seems to be linked to the strength of the streaming flow and the local gradients that appear in Equation (5.18). Previous work has carried out linear stability analysis for particle trapping in generalized microvortices [102]. In [102], non-inertial particles were found to be unstably trapped in the center of vortexes and that flow convergence zones can also form stable traps. Furthermore, they found that Faxén corrections to Eq. (5.2) can have significant effect on trapping, corroborating recent work [95] in which Faxén and Saffman lift were identified as key contributions to the

trajectories of particles predicted by the (force-modified) Maxey-Riley equation. Linear and nonlinear stability of predicted trap sites using full particle physics models appears to be warranted for hydrodynamic tweezers. Not all particle trap sites are created equal.

Conclusion

The goal of this paper was to demonstrate the simplicity of the leading order contributions to the inertial deviations from ideal tracer particle motion and trapping location in hydrodynamic tweezers. We have shown that our analytic-numeric approach to simulating steady streaming microeddy flows coupled with inertial particle analysis generates discernible final trapping location differences that depend on the particle Stokes number. This analysis can be extended to wide range of oscillating flows, yielding trapping locations consistent with experiments. Computation of accurate particle trajectories, however, requires contributions from Faxén and Saffman forces, since nearly all particle trajectories into the trapping site pass near the cylinder surface [95]. For full physics analysis, especially when using higher frequencies (which brings particles closer to the surface), these forces may be added to Maxey-Riley used here, and may also be relevant to future stability analysis of trap sites.

CHAPTER 6 || INERTIAL TRAPPING LOCATION ANALYSIS IN HYDRODYNAMIC TWEEZERS

Understanding the trapping behavior of particles is a critical step in the development of hydrodynamic tweezers as a useful analytical technique. Our recent publication (Lieu, House, and Schwartz 2012) in Ch. 3 described the simple frequency-dependence of trap location distance from obstruction for a single particle size [42]. Despite these experimental advances, predicative ability is lacking. In the preceding Ch. 5, some examples were shown of the ability to predict the location of a trap in a hydrodynamic tweezers array by use of the time-averaged inertial particle velocity. In this chapter, the previous work of adding inertial effects to the standard Stokes drift calculation will be implemented with the goal of determining the long-time trapping behavior for a range of particle inertias and fluid oscillation traits.

Introduction and Methods

Micro-objects that we may want to trap or transport in a streaming flow will have small but finite inertia that is proportional to the particle Stokes number

$$St = \frac{2U_0 b^2}{9\eta \nu a}, \tag{6.1}$$

where b is the particle radius, $U_0 = \omega s$ is a characteristic fluid velocity, $\eta = \rho_f / \rho_p$ is the fluid-to-particle density ratio, and other variables have been defined. As we show later, a useful

additional variable is $\varphi = b / a$. The Maxey and Riley force balance is a dynamic equation for the velocity **V** of a rigid spherical particle in a non-uniform flow field, where the Eulerian-frame velocity is **U**:

$$St\frac{\mathrm{d}\mathbf{V}}{\mathrm{d}t} = St\,\eta\frac{\mathrm{D}\mathbf{U}}{\mathrm{D}t} - \frac{St\,\eta}{2}\frac{\mathrm{d}}{\mathrm{d}t}\left(\mathbf{V}-\mathbf{U}\right) - \left(\mathbf{V}-\mathbf{U}\right) - \sqrt{\frac{9\eta St}{2\pi}}\int_{-\infty}^{t}\frac{\mathrm{d}/\mathrm{d}\tau\left(\mathbf{V}[\tau]-\mathbf{U}[\tau]\right)}{\sqrt{t-\tau}}\mathrm{d}\tau \quad . \tag{6.2}$$

Equation (6.2) holds for weak inertia when *St* is small compared to unity, resulting in a small relative velocity difference between the particle and local fluid velocity. A relative velocity, **W**(**x**, *t; St, η*), between the fluid and inertial particle may be defined where

$$\mathbf{V} = \mathbf{U} + \mathbf{W} \tag{6.3}$$

such that as $St \to 0$, the relative velocity $\mathbf{W} \to 0$ and **V** = **U**, resulting in the ideal non-inertial tracer. The first correction to account for weak inertial affects occurs in terms of *O(St)*.

Determination of trapping locations

Particles come to rest when the period-averaged particle velocity **<V>** = 0, and for the purposes of this paper, we use this as the definition of a trapping location. To find this period-average, we will summarize the previous work of Ch. 4 and Ch. 5 where we laid out the instantaneous particle velocity, and then approximated the time average motion by defining and computing an inertial Stokes drift. To find the instantaneous particle velocity, we define a general periodic flow velocity **U**(**x**, *t*) at a given Cartesian point **x** and time *t* as

$$\mathbf{U}\left(\mathbf{x},\,t\right) = \varepsilon\left(\mathbf{U}^{c}\left(\mathbf{x}\right)\cos t + \mathbf{U}^{s}\left(\mathbf{x}\right)\sin t\right) + \varepsilon^{2}\,\mathbf{U}^{st}\left(\mathbf{x}\right) + \text{H.O.T.}, \tag{6.4}$$

with first order oscillating components $\mathbf{U}^{c}(\mathbf{x})$ and $\mathbf{U}^{s}(\mathbf{x})$ driving a second order steady motion $\mathbf{U}^{st}(\mathbf{x})$, where the amplitude of fluid oscillations, *s*, is small compared to a characteristic length, *a*, such that $\varepsilon = s/a \ll 1$. For compatibility with the flow field formulation and Eq. (6.2), the particle velocity **V**(*t*; **x**) at time *t* with center of mass located at **x** is similarly defined

$$\mathbf{V}\left(t;\mathbf{x}\right)=\varepsilon\left(\mathbf{V}^{c}\cos t+\mathbf{V}^{s}\sin t\right)+\varepsilon^{2}\,\mathbf{V}^{st}+\text{H.O.T.}. \tag{6.5}$$

Examining Eq. (6.2), one sees an appropriate expansion for small Stokes numbers is

$$\mathbf{V}=\mathbf{V}_{0}+\mathbf{V}_{1}\,St+\mathbf{V}_{3/2}\,St^{3/2}+\mathbf{V}_{2}\,St^{2}+\text{H.O.T.} \tag{6.6}$$

Furthermore, each of the particle velocity components in Eq. (6)—$\mathbf{V}^{c}$, $\mathbf{V}^{s}$, and $\mathbf{V}^{st}$—can be expanded in the form of Eq. (6.6). Algebraically solving at successive orders of Stokes number, the combined $O(\varepsilon)$ oscillating particle velocities are

$$\mathbf{V}^{c}=\mathbf{U}^{c}+St\left(\eta-1\right)\mathbf{U}^{s}+\text{H.O.T.}, \tag{6.7}$$

and

$$\mathbf{V}^{s}=\mathbf{U}^{s}-St\left(\eta-1\right)\mathbf{U}^{c}+\text{H.O.T.}, \tag{6.8}$$

where higher order terms have been omitted here (see Ch. 4 for additional higher order terms). Following the same process at $O(\varepsilon^{2})$, the steady particle velocity is found to be

$$\mathbf{V}^{st}=\mathbf{U}^{st}+St\frac{3}{4}\eta\left(U_{x}^{c}\frac{\partial\mathbf{U}^{c}}{\partial x}+U_{x}^{s}\frac{\partial\mathbf{U}^{s}}{\partial x}+U_{y}^{c}\frac{\partial\mathbf{U}^{c}}{\partial y}+U_{y}^{s}\frac{\partial\mathbf{U}^{s}}{\partial y}\right)+\text{H.O.T.}. \tag{6.9}$$

Again, additional terms may be found in Ch. 4.

For the physics incorporated in Eq. (6.2), it is interesting to note that the influence of inertia on the oscillatory motion of the particle vanishes when $\eta = 1$ in Eqs. (6.7) and (6.8), but Eq. (6.9) shows that inertia influences the mean velocity of the particle even when $\eta = 1$. In short, there are realistic conditions ($\eta = 1$) where the oscillatory velocity of the particle is independent of *St*, and yet the mean particle motion displays a *St*-dependency. When *St* is finite, there is a difference in the relaxation time of the transported particle and the flow.

With knowledge of the instantaneous velocity of the particle, period-averaged particle velocity can be approximated. To do this, the standard flow field **U** has a small relative particle

velocity **W** added to it such that after a small displacement, $\Delta\mathbf{x}$, the new instantaneous particle velocity is

$$\mathbf{V}(t) = \mathbf{U}(\mathbf{x_0} + \Delta\mathbf{x},\, t) + \mathbf{W}(\mathbf{x_0} + \Delta\mathbf{x},\, t). \tag{6.10}$$

The period-averaged velocity is easily calculated using a similar principle as defined in the inertial Stokes drift section of Ch. 4. The period-averaged inertial particle velocity is

$$\langle \mathbf{V} \rangle = \varepsilon^2 \mathbf{U}^{st} + \varepsilon^2 \frac{3}{4} \eta St \left(U_x^c \frac{\partial \mathbf{U}^c}{\partial x} + U_x^s \frac{\partial \mathbf{U}^s}{\partial x} + U_y^c \frac{\partial \mathbf{U}^c}{\partial y} + U_y^s \frac{\partial \mathbf{U}^s}{\partial y} \right)$$

$$+ \varepsilon^2 \frac{1}{2} \left(-U_x^s \frac{\partial \mathbf{U}^c}{\partial x} + U_x^c \frac{\partial \mathbf{U}^s}{\partial x} - U_y^s \frac{\partial \mathbf{U}^c}{\partial y} + U_y^c \frac{\partial \mathbf{U}^s}{\partial y} \right). \tag{6.11}$$

which includes an inertial correction to the classical Stokes drift calculation. Equation (6.11) yields the traditional non-inertial period-averaged velocity (see Eqs. (2.18) and (2.20)) for this flow field, as $St \rightarrow 0$. In microtrapping, Equation (6.11) allows us to connect a computed Eulerian-frame flow field (**U**) to the particle motion in that flow (**V**), and determine the mean motion without calculating the oscillating motion of the particle. This is computationally very efficient for a complex flow field.

Again, it should be noted that particles come to rest when the period-averaged particle velocity **<V>** = 0, and this will be the definition of a particle trap that we use in the following results. In the preceding chapter, some examples were shown of the ability to predict the location of a trap in a hydrodynamic tweezers array by use of the time-averaged inertial particle velocity. In this chapter, the previous work of adding inertial effects to the standard Stokes drift calculation will be implemented with the goal of determining the long-time trapping behavior for a range of particle inertias and oscillation frequencies.

Steady streaming flow modeling

Numerical solutions of the coupled linear equations were found as described in Ch. 2 and Ch. 4, with the critical non-dimensional parameters of the flow field being $M^2 = a^2\omega/\nu$. These flow parameters allow us to redefine *St* for a particle in this flow as

$$St = \frac{2\varepsilon M^2 \varphi^2}{9\eta}, \tag{6.12}$$

where we define $\varepsilon = 0.1$ for particle calculations. Here, we first model the center cell in an array of cylindrical posts with boundary conditions specifying the symmetry of the system. After thorough analysis of this geometry, we will revisit the 9 geometric shapes used in Ch. 3 and perform trapping location analysis to compare with experimental results published in that article [42]. Mesh-independent converged solutions were tested by computing boundary integrals at the left and right boundaries and checking for zero net flow. The mesh consisted of 130,000 triangular elements with a maximum element size of $0.0165a$ in the principal investigation area ($0 \le x \le 2.5a$, $0 \le y \le 2.5a$). Steady streaming eddies can be seen from the contours of steady Eulerian stream function plotted in Figure 39. Cellular flow structure shows the left and right counter-rotating eddies (counterclockwise and clockwise, respectively). In all subsequent flow plots, we normalize distance by the cylinder radius *a*.

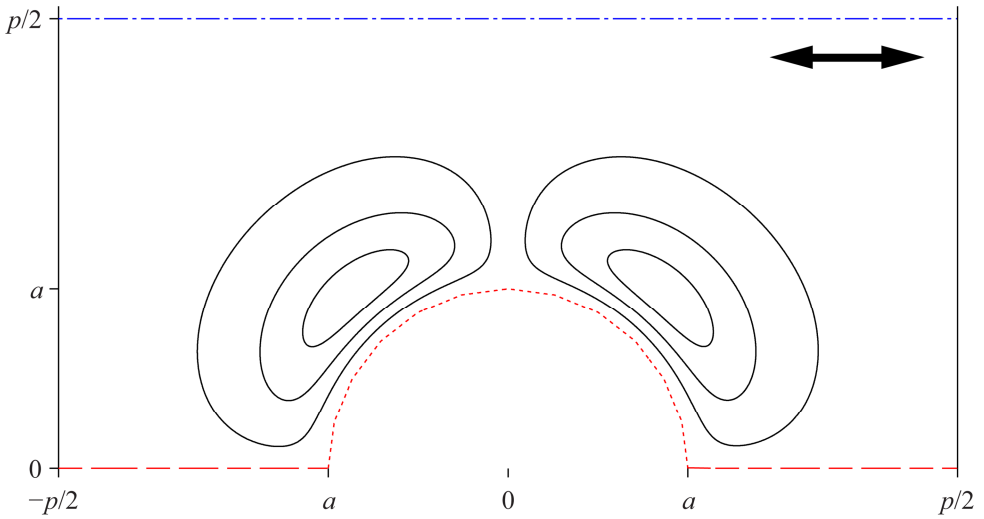

Figure 39. Symmetry geometry used in simulation of array of cylindrical posts. Contours are shown for the stream function with dimensionless oscillation frequency $M = 9.1$, pitch distance $p = 2.5a$, and oscillations occurring horizontally. Red dotted curve indicates solid post boundary; red dashed line and blue dash-dot-dash lines are symmetry conditions indicating no net flux and no vorticity separated by cosine stream function difference of $p/2$. Solid black boundaries (left and right) are periodic no net flux and no vorticity symmetry conditions.

Results and Discussion

To show how inertia and frequency effects the location of a trap location, we will compute trap locations for particles with a range of particle sizes, densities, and overall inertias over a range of frequencies. The trap location will be reduced to a simple distance measurement to the nearest physical wall and normalized by the characteristic length (e.g. radius) of the obstruction feature. We will start by analyzing trapping locations in a square array of cylindrical posts driven at a single oscillation frequency.

In Figure 40, the Lagrangian steady stream function contours are shown as black lines for steady streaming flow of frequency $M = 8.2$, depicting the equivalent image as ideal non-inertial tracers. Superimposed over this depiction of the flow field is the magnitude of the period-averaged particle velocity for a particle with $\eta = 3.77$, $\varphi = 0.02$, and $St = 0.0002$. Physically, this corresponds to a low density particle that is 2% as large as the obstruction. The grayscale shading shows the $\log_{10}$ of the magnitude of the period-averaged inertial particle velocity, where

white denotes a velocity magnitude approaching zero and darker colors indicate higher speeds. This low Stokes number and particle size results in a particle trap very near the center of the Lagrangian eddy, as expected when inertial effects are negligible (as $St \rightarrow 0$).

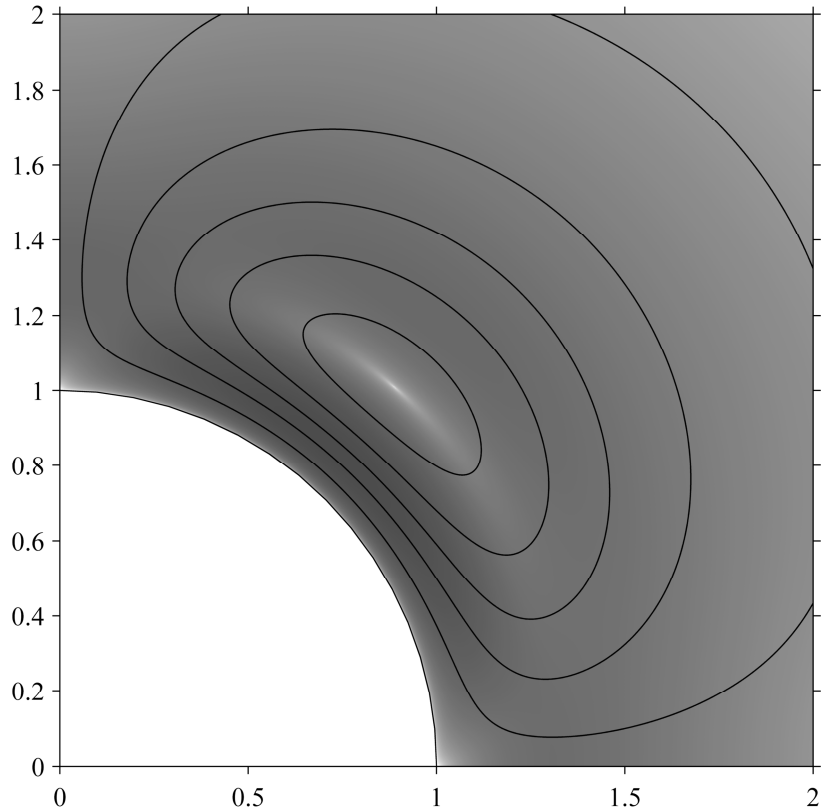

Figure 40. Lagrangian steady stream function contours are black lines with frequency $M = 8.2$. Grayscale shading shows the $\log_{10}$ of the magnitude of the period-averaged inertial particle velocity with $\eta = 3.77$, $\varphi = 0.02$, and $St = 0.0002$, where white shows zero velocity, and darker colors indicate higher speed.

In Figure 41, the Lagrangian steady stream function contours for the same conditions as in Figure 40 are shown. Superimposed over this depiction of the flow field is the magnitude of the period-averaged particle velocity for a particle with $\eta = 3.77$, $\varphi = 0.11$, and $St = 0.005$. These conditions correspond to the same low density particle, but it is now 5 times larger in radius. As before, the grayscale shading shows the $\log_{10}$ of the magnitude of the period-averaged inertial particle velocity. The Stokes number is sufficiently large so that the trapping location is shifted towards positive y and negative x from the center of the Lagrangian eddy.

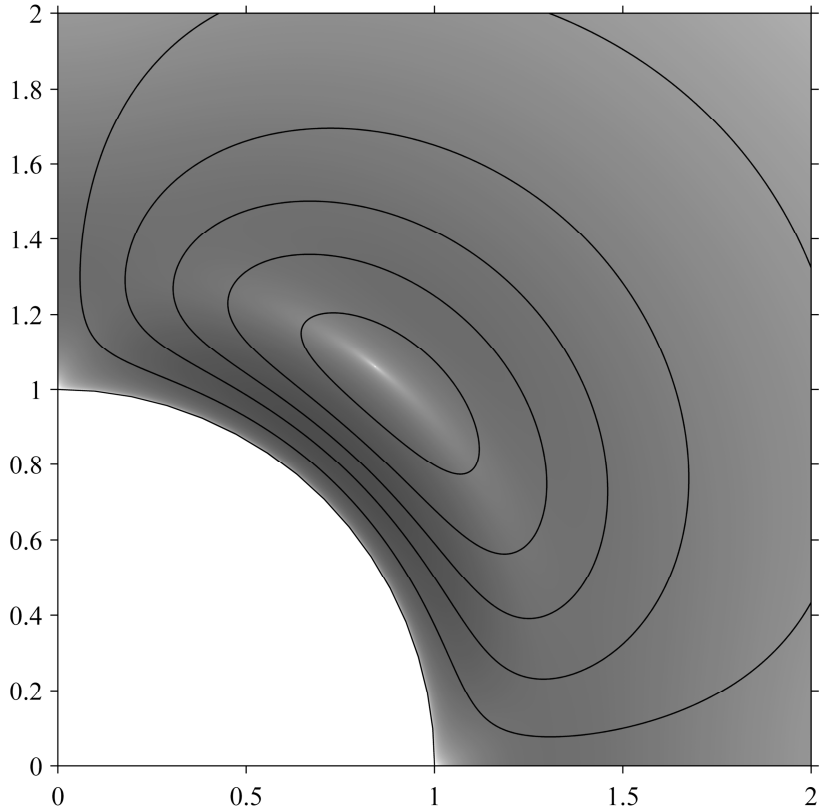

Figure 41. Lagrangian steady stream function contours are black lines with frequency $M = 8.2$. Grayscale shading shows the $\log_{10}$ of the magnitude of the period-averaged inertial particle velocity with $\eta = 3.77$, $\varphi = 0.11$, and $St = 0.005$, where white shows zero velocity, and darker colors indicate higher speed.

In Figure 42, the Lagrangian steady stream function contours are shown for the same conditions as in Figure 40 and Figure 41 (i.e. $M = 8.2$). Superimposed over this depiction of the flow field is the magnitude of the period-averaged particle velocity for a particle with $\eta = 3.77$, $\varphi = 0.2$, and $St = 0.016$. Again, the grayscale shading shows the $\log_{10}$ of the magnitude of the period-averaged inertial particle velocity. The increasingly large Stokes number causes a larger shift of the trapping location away from the center of the Lagrangian eddy.

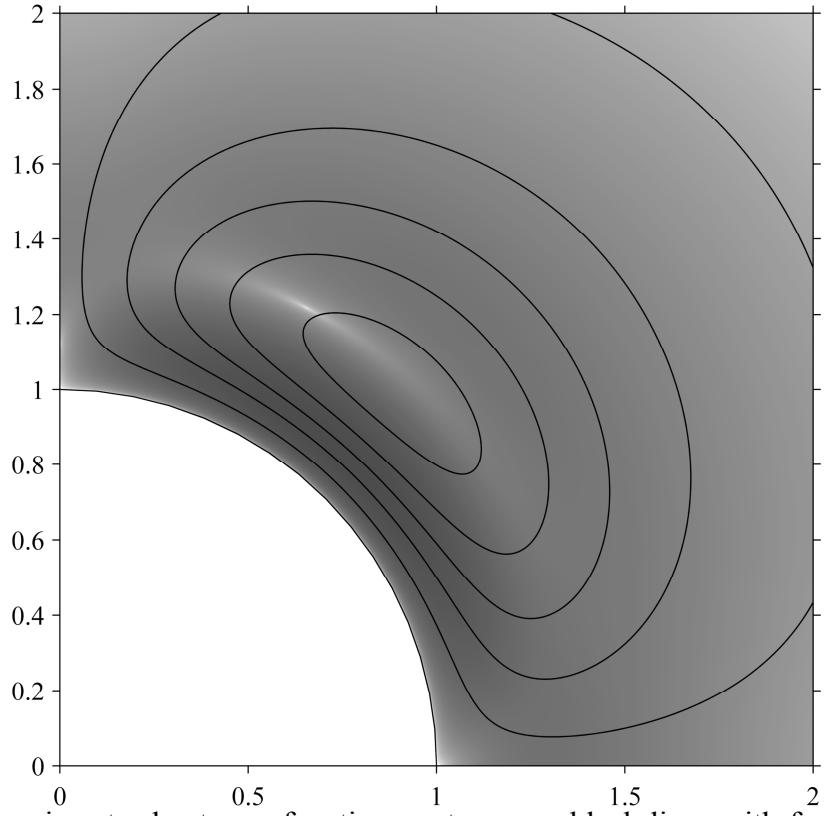

Figure 42. Lagrangian steady stream function contours are black lines with frequency $M = 8.2$. Grayscale shading shows the $\log_{10}$ of the magnitude of the period-averaged inertial particle velocity with $\eta = 3.77$, $\varphi = 0.2$, and $St = 0.016$, where white shows zero velocity, and darker colors indicate higher speed.

There are several additional features of our computations that warrant discussion. Low particle speeds (white regions in the grayscale mapping) are also seen at each stagnation point in the simulation. These do not represent experimentally observed traps. For stagnation points against walls, finite sized particles are excluded. For example, a particle of dimension $\varphi = 0.02$ (Figure 39) will be excluded for that distance from the surface of the cylinder. Likewise, particles with $\varphi = 0.11$ and $\varphi = 0.2$ are excluded a distance of 0.11 and 0.2, respectively, from the wall (Figure 40 and Figure 41). Not shown, but seen in all simulations, is that there is a predicted trap at symmetry-line stagnation points between each periodic cell. Though not as stable as the traps near the eddy center, we sometimes do see particles trapped in those locations. Though not emphasized here, certain types of stagnation points in hydrodynamic flows can be useful for

particle trapping (see Ch. 5 and [102], [103]). It is also worth noting that as the particle gets larger, the Faxén corrections and other forces such as Saffman lift will play an ever increasing role in the trapping physics [80], [81]; our analysis did not include these forces.

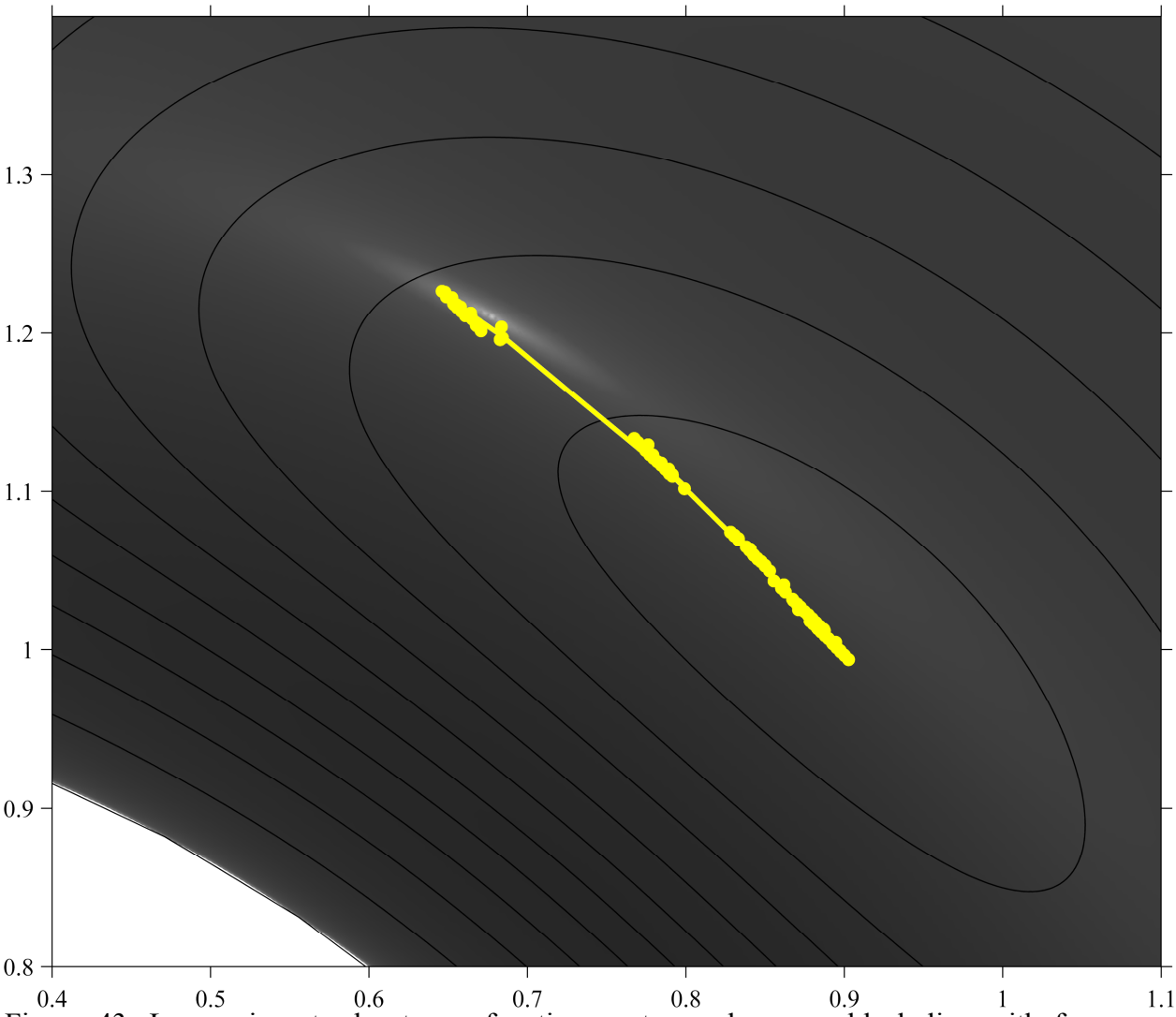

Figure 43. Lagrangian steady stream function contours shown as black line with frequency $M = 8.2$. Grayscale shading shows the $\log_{10}$ of the magnitude of the period-averaged inertial particle velocity for $\eta = 7.1$, $\varphi = 0.2$, and $St = 0.15$, where white shows zero velocity, and darker colors indicate higher speed. Trapping locations (150 yellow points) are for 30 density values $\eta = 0.4$ through $\eta = 7.1$, and five size ratios $\varphi = 0.02$ through $\varphi = 0.2$, giving a range of Stokes number $St = 0.0002$ through $St = 0.15$. The yellow line plots the best fit line between all points.

The case studies in Figure 40 - Figure 42 showed that increasing the particle inertia moves the trapping location away from the Lagrangian eddy center. To explore this idea further, we compute the trap locations for a broad range of particles, from small to large and dense to

buoyant, and compile the results in Figure 43, for same steady streaming flow of frequency $M = 8.2$. Grayscale shading shows the $\log_{10}$ of the magnitude of the period-averaged inertial particle velocity for the extreme case of $\eta = 7.1$, $\varphi = 0.2$, and $St = 0.15$. Trapping locations (150 yellow points) are for 30 density ratio values $\eta = 0.4$ through $\eta = 7.1$, and five particle size ratios $\varphi = 0.02$ through $\varphi = 0.2$, giving a range of Stokes number $St = 0.0002$ through $St = 0.15$. The yellow curve in the figure shows the trend line. For the single set of flow field conditions, the trap locations cluster according the particle size φ, while the variance in particle density η provides a secondary effect. This is accounted for by the previous analysis, that showed that the leading order inertial effect on the Stokes drift of an inertial particle is of $O(\eta \cdot St)$ as in Eq. (6.11), which is directly proportional to phi. In contrast, higher order inertial effects show varying orders of η and St (see Ch. 4), and that gives rise to the spread in each cluster. The highest particle sizes are shown as farthest away from the center of the Lagrangian eddy, while smaller particles sizes approach the center of the eddy as $St \rightarrow 0$.

The flow field interacts with inertia to cause deviation in the trapping location. Steady streaming flow fields for a range of frequencies were computed for the same geometry as above. Dimensionless frequencies between $M = 3.33$ to $M = 10$, corresponding to normalized Stokes boundary layer thicknesses of $\delta_{AC}/a = 0.3$ to $\delta_{AC}/a = 0.1$, were used for the simulations. In Figure 44 trapping distances away from the post wall (L) was normalized by post radius for 150 points determined using ten frequencies $M = 3.33$ to $M = 10$, three density values $\eta = 0.4$ through $\eta = 7.1$, and five size ratios $\varphi = 0.02$ through $\varphi = 0.2$, giving a range of Stokes number $St = 1.4 \cdot 10^{-5}$ through $St = 0.22$, and $\eta \cdot St$ products ranging from $\eta \cdot St = 0.0001$ to $\eta \cdot St = 0.089$. Black line shows normalized distance for center of the Lagrangian eddy.

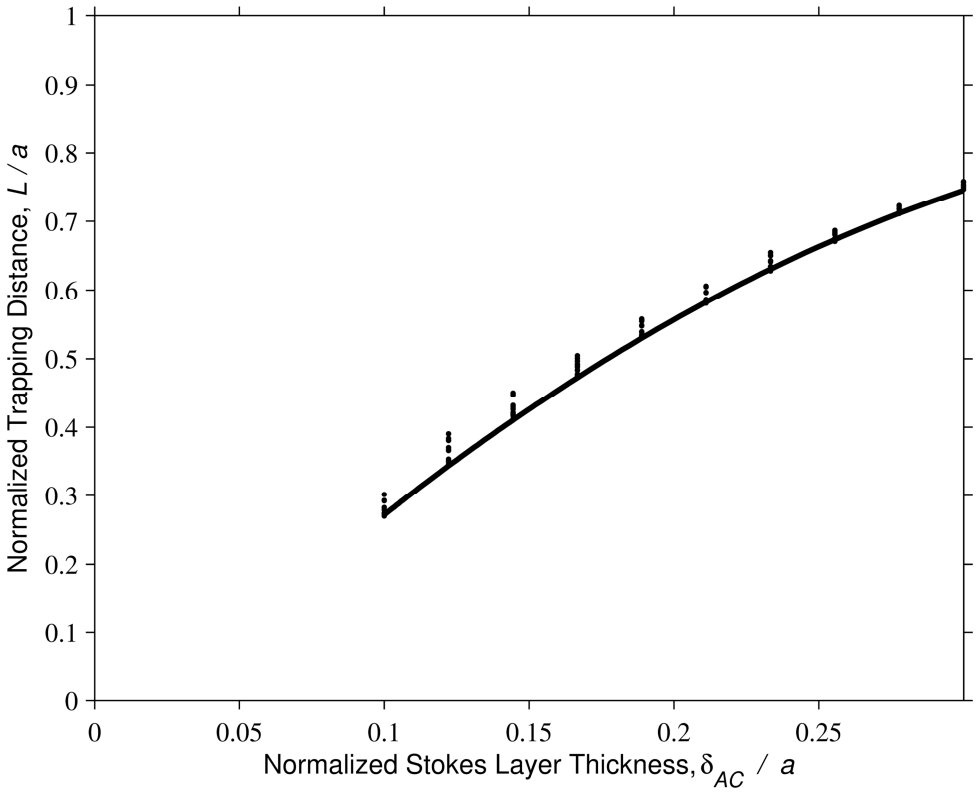

Figure 44. Trapping location distances from post wall normalized by post radius for 150 points with ten frequencies $M = 3.33$ to $M = 10$, three density values $\eta = 0.4$ through $\eta = 7.1$, and five size ratios $\varphi = 0.02$ through $\varphi = 0.2$, giving a range of Stokes number $St = 1.4 \times 10^{-5}$ through $St = 0.22$. The black line plots the best fit line between all points. Black line shows normalized distance for center of Lagrangian eddy.

Figure 44 shows that as the Stokes layer thickness increases (i.e. oscillation frequency decreases), the spread in the trap location distance decreases and all particle approach ideal non-inertial tracer behavior. This makes sense from the definition of the particle Stokes number Eq. (6.1), where inertial effects become less important as the oscillation frequency is decreased. For all values computed, none of the trap locations measured are closer than the center of the Lagrangian eddy. This shift is at odds with previous experiments, where larger particles (i.e. with more inertia) were shown to trap closer to posts than the center of the eddy. This indicates that some of the currently excluded physics in our form of the Maxey-Riley equation may need to be applied for more accurate trapping location prediction [33], [39]. Despite this shortcoming, the

principle analysis and method used to generate and compute trapping locations is applicable to a broad range of inertial particles in oscillating flows.

To show this applicability, we have computed the predicted trapping locations for the 9 geometries used in Ch. 3. Here, we compute trapping locations for a range of oscillation frequencies for particles with the same size $\varphi = 0.2$ and density $\eta = 0.95$ that were used for the trapping experiments. In Figure 45, these trapping locations are plotted for each of the 9 geometries of Ch. 3 over the same range of frequencies originally tested.

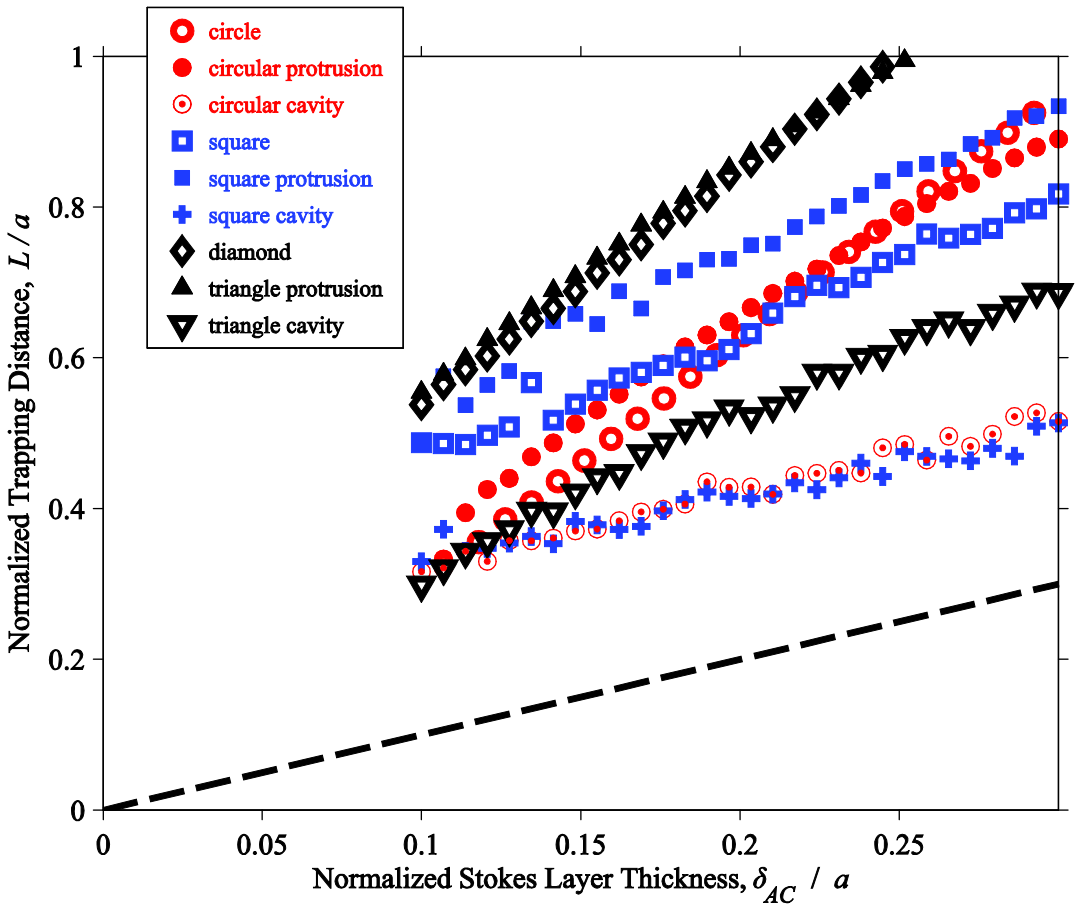

Figure 45. Plot of trapping locations for nine geometries used in Ch. 3 for particles with $\varphi = 0.2$ and density $\eta = 0.95$. Black dashed line indicates trapping at the Stokes layer.

The range in Stokes number for these computations is from $St = 0.01$ at $\delta_{AC}/a = 0.3$ to $St = 0.093$ at $\delta_{AC}/a = 0.1$. This again shows that the inertia of a particle as measured by the Stokes number decreases as the frequency of oscillation decreases. The jaggedness in the images

is a result of small numerical error from our previous flow field computations. If important in the future, the mesh can be further refined to improve these calculations.

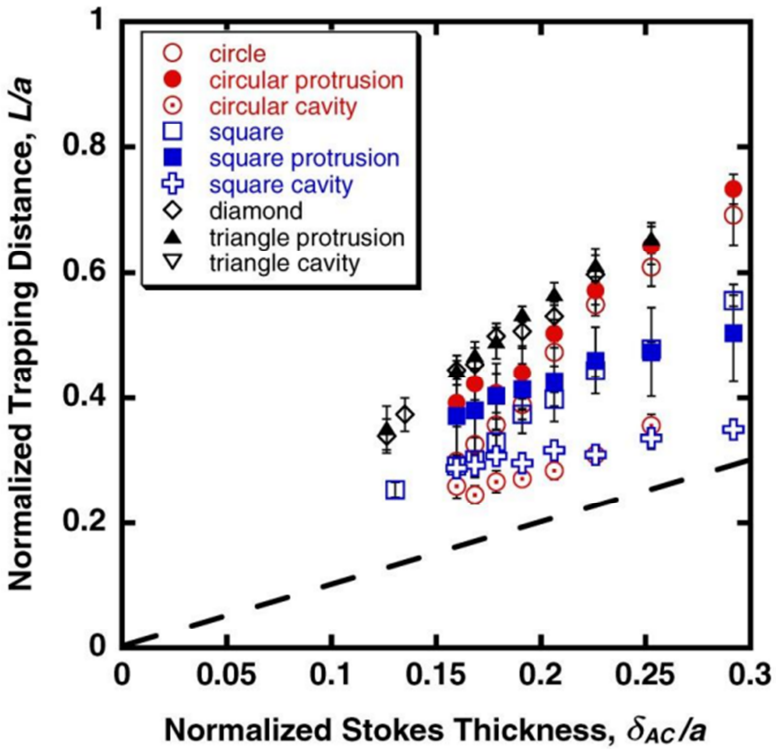

Figure 46. Dimensionless plot of particle trapping distance as a function of Stokes layer thickness for the 9 geometries evaluated. Black dashed line indicates trapping at Stokes layer [42].

Finally, when compared with the equivalent experimental particle trapping distances shown in Figure 46 (from Lieu, House, and Schwartz, 2012), we see important similarities. [42]. For one, the experimental square and circular cavity geometries demonstrated particle trapping that is closest to the cylinder for all the geometries tested. This close trapping is accurately predicted by our period-averaged particle velocity computations. Secondly, the centered diamond and triangular protrusion were the two geometries with the farthest particle trapping – a trend also predicted by our analytics. Similar trends are seen for the other geometries. The predictive ability for our particle motion analytics is qualitatively useful, even though the predicted traps systematically over-predict the distance between the particle and the wall.

Conclusion

The goal of this paper was to apply the broadly explore the parameter space to understand the role of the flow field parameters frequencies and geometries, and particle parameters diameter, denisty, and Stokes number. The leading order contributions to the inertial deviations from ideal tracer particle motion have been shown to predict the trapping location in hydrodynamic tweezers. We extended previous analysis to wide range of oscillating flows, yielding trapping trends consistent with experiments. Computation of accurate particle trajectories, however, requires contributions from Faxén and Saffman forces, since nearly all particle trajectories into the trapping site pass near the cylinder surface [95]. For full physics analysis, especially when using higher frequencies (which brings particles closer to the surface), these forces may be added to Maxey-Riley used here, and may also be relevant to future stability analysis of trap sites.

CHAPTER 7 || CONCLUDING REMARKS

This thesis presented a computationally efficient method to predict inertial particle dynamics and trapping in steady streaming flows. Though much of the work relied on geometries that reflect experiments we carry out in the lab, our approach and solution method was general to a broad range of steady streaming flows.

In Ch. 2, the method used to simulate and visualize steady streaming flows was described. The efficient analytic-numeric approach that was used allowed for quick computation of steady streaming flows without the need to compute time-dependent solutions. Using our methods, results may be obtained in a matter of minutes rather than days for comparable COMSOL solution of the Navier-Stokes equations. The major factor controlling accuracy and solution time is the number of elements used in the mesh and the amplitude of the flow field oscillation. We compared our solutions for a simple case of a centered cylindrical post to the analytical results from Holtsmark, et al. (1954). We find that the Stokes drift-corrected analytic-numeric solutions provide a sound basis for comparison with experiments and subsequent computation of inertial particle motion in the flow.

In Ch. 3, comparisons of flow simulations with experimental measurements were shown. The majority of these results were published as [Lieu, House, and Schwartz, "Hydrodynamic tweezers: impact of design geometry on flow and microparticle trapping," *Anal. Chem.*, vol. 84,

no. 4, pp. 1963–8, Feb. 2012], though additional figures and analysis were added where noted. We have explored 9 different steady streaming microdevice geometries to evaluate the connection between geometry, steady streaming flow, and microparticle trapping. Comparing simulations with experimental flows, we see the overall features of flow adjacent to wall protrusions and freestanding posts are quite similar among geometric pairs. Simulations also confirm that cavities have a significantly different steady flow structure and flow strength. At a finer scale, replacing a flow symmetry line in a freestanding feature with a wall slightly disrupts the symmetry and shape of the eddy.

In Ch. 4, we showed an analytical formulation of the time-averaged velocity of an inertial particle in a generalized oscillating flows. The paper demonstrated, for the first time, the simplicity of leading order contributions to the inertial deviations from an ideal, non-inertial Stokes drift tracer particle motion. This inertial Stokes drift has been computed for wavy flows, but never steady streaming flows. Our analysis of inertial-corrected Stokes drift shows that particle inertia causes significant particle path differences over single periods, and this affects the overall particle motion and trapping. Furthermore, our use of analytical time-averaging lets us predict inertial velocity deviations accurately and with computational efficiency, since we average-out all of the fast motion. This novel analysis is valid a wide range of oscillating flows where surface effects are not significant drivers of particle motion.

In Ch. 5, we showed a qualitative comparison of predicted trapping locations with experimental trapping in arrays, currently in review as House, Lieu, and Schwartz, "A Model for Inertial Particle Trapping Locations in Hydrodynamic Tweezers Arrays." The paper shows how to use the simple, leading order contributions to the inertial deviations of motion to predict the particle trapping location in hydrodynamic tweezers. The particle trapping location is shown to

depend on the particle Stokes number in a manner revealed by the analytical problem formulation. Chapter 6 extends the work of Chapter 5 by analyzing the trapping locations for a wide range of particle traits, flow field variables, and flow geometries [House and Schwartz, in preparation]. It was found that device geometry strongly affects how closely the particles trap to the obstruction. However, systematic deviations from experiments suggest that other forces may need to be added to the particle equations of motion we used here.

For the work shown in Ch. 4 through Ch. 6, we chose to use the Maxey-Riley equation (4.2) as the basis for our inertial particle analysis. For clarity and simplicity in our results, we ignored several additional force terms that sometimes modify the equation, including Faxén corrections, gravitational forces, and Saffman lift forces [80]–[83]. These terms can be important for specific regions of a flow, for example, near solid surfaces or other highly non-uniform regions, but they are rarely the dominant terms [81]–[84]. Particle trajectories normally pass close to wall prior to trapping, meaning the path includes non-uniform, high shear areas of flow. Thus, a natural extension of this work is to consider in some detail contributions from Faxén and Saffman forces. Recent theoretical work from Chong et al. (2013) supports the role of these additional forces in the motion of particles. Chong et al. provided a model for the instantaneous inertial motion of particles in the streaming adjacent to an oscillating infinite cylinder based on the Holtsmark analytical solutions [95]. Similarly to our work, they adapted the particle force balance from Maxey and Riley, including the Saffman lift force

$$\sqrt{\frac{2\eta\, St\, K^2}{9\pi^2}}\left(\left|\mathbf{G}\right|\right)^{1/2} sign\left(\mathbf{G}\right)\left|\mathbf{U}-\mathbf{V}\right|\mathbf{n}\ , \tag{7.1}$$

where **G** is the shear rate defined by

$$\mathbf{G}=\left(\left|\mathbf{W}\right|\right)^{-2}\left(\left(W_x\right)^2\frac{\partial U_x}{\partial y}-\left(W_y\right)^2\frac{\partial U_y}{\partial x}-\left(W_x\right)\left(W_y\right)\left(\frac{\partial U_x}{\partial x}-\frac{\partial U_y}{\partial y}\right)\right)\ , \tag{7.2}$$

K is a constant equal to 1.615, and the normal vector **n** is defined normal to the relative velocity **W** [81], [82], [95]. They solved Maxey-Riley equation numerically (without time averaging) by using the analytical Holtsmark solution to describe the flow field **U**. Like our analysis, they showed that small inertia particles trap near the center of the streaming eddies. Their computation of the particle motion included both the fast and the slow dynamics of the particle motion, and therefore, had none of the computational efficiency time-averaging affords. They found Saffman lift played an important role in trapping, and thus should be incorporated in future work of this nature. Our fast analytic-numeric approach for both the flow field and the particle dynamics allows for a wide range of streaming flows around novel geometries to be computed and particle trapping to be approximated without the need for lengthy time-dependent computations. Clever integration of our analytical approaches with the additional forces Chong et al (2013) identified will transform these two interesting scientific studies into a quantitative design tool for developing optimized hydrodynamic tweezers arrays that can be tuned for trapping strength, trapping density, particle shear stress, etc.

BIBLIOGRAPHY

[1] G. M. Whitesides, "The origins and the future of microfluidics.," *Nature*, vol. 442, no. 7101, pp. 368–73, Jul. 2006.

[2] P. Gravesen, J. Branebjerg, and O. S. Jensen, "Microfluidics-a review," *J. Micromechanics Microengineering*, vol. 3, no. 4, pp. 168–182, Dec. 1993.

[3] A. Manz, N. Graber, and H. M. Widmer, "Miniaturized total chemical analysis systems: A novel concept for chemical sensing," *Sensors Actuators B Chem.*, vol. 1, no. 1, pp. 244–248, 1990.

[4] D. R. Reyes, D. Iossifidis, P.-A. Auroux, and A. Manz, "Micro total analysis systems. 1. Introduction, theory, and technology.," *Anal. Chem.*, vol. 74, no. 12, pp. 2623–36, Jun. 2002.

[5] H. A. Stone, A. D. Stroock, and A. Ajdari, "Engineering Flows in Small Devices: Microfluidics Toward Lab-on-a-Chip," *Annu. Rev. Fluid Mech.*, vol. 36, no. 1, pp. 381–411, Jan. 2004.

[6] D. J. Beebe, G. A. Mensing, and G. M. Walker, "Physics and applications of microfluidics in biology.," *Annu. Rev. Biomed. Eng.*, vol. 4, pp. 261–86, Jan. 2002.

[7] S. Kim and S. J. Karrila, *Microhydrodynamics: principles and selected applications*. DoverPublications. com, 1991.

[8] D. Di Carlo, "Inertial microfluidics.," *Lab Chip*, vol. 9, no. 21, pp. 3038–46, Nov. 2009.

[9] D. J. Laser and J. G. Santiago, "A review of micropumps," *J. Micromechanics Microengineering*, vol. 14, no. 6, pp. R35–R64, Jun. 2004.

[10] K. W. Oh and C. H. Ahn, "A review of microvalves," *J. Micromechanics Microengineering*, vol. 16, no. 5, pp. R13–R39, May 2006.

[11] B. Kuswandi, Nuriman, J. Huskens, and W. Verboom, "Optical sensing systems for microfluidic devices: A review," *Anal. Chim. Acta*, vol. 601, no. 2, pp. 141–155, 2007.

[12] R. C. Hughes, A. J. Ricco, M. A. Butler, and S. J. Martin, "Chemical microsensors.," *Science*, vol. 254, no. 5028, pp. 74–80, Oct. 1991.

[13] N. T. Nguyen, "Micromachined flow sensors—a review," *Flow Meas. Instrum.*, vol. 8, no. 1, pp. 7–16, 1997.

[14] N. T. Nguyen and Z. Wu, "Micromixers—a review," *J. Micromechanics Microengineering*, vol. 15, no. 2, pp. R1–R16, Feb. 2005.

[15] V. Hessel, H. Löwe, and F. Schönfeld, "Micromixers—a review on passive and active mixing principles," *Chem. Eng. Sci.*, vol. 60, no. 8, pp. 2479–2501, 2005.

[16] H. Andersson and A. van den Berg, "Microfluidic devices for cellomics: a review," *Sensors Actuators B Chem.*, vol. 92, no. 3, pp. 315–325, 2003.

[17] P. Cooley, "Applicatons of Ink-Jet Printing Technology to BioMEMS and Microfluidic Systems," *J. Assoc. Lab. Autom.*, vol. 7, no. 5, pp. 33–39, Oct. 2002.

[18] S. A. Vanapalli, M. H. G. Duits, and F. Mugele, "Microfluidics as a functional tool for cell mechanics.," *Biomicrofluidics*, vol. 3, no. 1, p. 12006, Jan. 2009.

[19] Y. Gao, W. Li, and D. Pappas, "Recent advances in microfluidic cell separations," *Analyst*, vol. 138, no. 17, pp. 4714–21, Sep. 2013.

[20] J. Nilsson, M. Evander, B. Hammarström, and T. Laurell, "Review of cell and particle trapping in microfluidic systems.," *Anal. Chim. Acta*, vol. 649, no. 2, pp. 141–57, Sep. 2009.

[21] K.-K. Liu, R.-G. Wu, Y.-J. Chuang, H. S. Khoo, S.-H. Huang, and F.-G. Tseng, "Microfluidic Systems for Biosensing," *Sensors*, vol. 10, no. 7, pp. 6623–6661, Jul. 2010.

[22] A. K. Yetisen, M. S. Akram, and C. R. Lowe, "Paper-based microfluidic point-of-care diagnostic devices.," *Lab Chip*, vol. 13, no. 12, pp. 2210–51, Jun. 2013.

[23] A. Karimi, S. Yazdi, and A. M. Ardekani, "Hydrodynamic mechanisms of cell and particle trapping in microfluidics," *Biomicrofluidics*, vol. 7, no. 2, p. 021501, Apr. 2013.

[24] D. G. Grier, "A revolution in optical manipulation.," *Nature*, vol. 424, no. 6950, pp. 810–6, Aug. 2003.

[25] J. R. Moffitt, Y. R. Chemla, S. B. Smith, and C. Bustamante, "Recent advances in optical tweezers.," *Annu. Rev. Biochem.*, vol. 77, pp. 205–28, Jan. 2008.

[26] E. R. Dufresne and D. G. Grier, “Optical tweezer arrays and optical substrates created with diffractive optics,” *Rev. Sci. Instrum.*, vol. 69, no. 5, p. 1974, 1998.
[27] P. R. C. Gascoyne and J. Vykoukal, “Particle separation by dielectrophoresis.,” *Electrophoresis*, vol. 23, no. 13, pp. 1973–83, Jul. 2002.
[28] R. Pethig, “Review article-dielectrophoresis: status of the theory, technology, and applications.,” *Biomicrofluidics*, vol. 4, no. 2, p. 022811, Jan. 2010.
[29] D. T. Chiu, “Cellular manipulations in microvortices,” *Anal. Bioanal. Chem.*, vol. 387, no. 1, pp. 17–20, Jan. 2007.
[30] P. Marmottant and S. Hilgenfeldt, “Controlled vesicle deformation and lysis by single oscillating bubbles,” *Nature*, vol. 423, no. 6936, pp. 153–156, 2003.
[31] W. Sachse, J. Collis, R. Manasseh, P. Liovic, P. Tho, A. Ooi, K. Petkovic-Duran, and Y. Zhu, “Cavitation microstreaming and stress fields created by microbubbles,” *Ultrasonics*, vol. 50, no. 2, pp. 273–279, 2010.
[32] P. Rogers and A. Neild, “Selective particle trapping using an oscillating microbubble.,” *Lab Chip*, vol. 11, no. 21, pp. 3710–5, Nov. 2011.
[33] B. R. Lutz, J. Chen, and D. T. Schwartz, “Hydrodynamic tweezers: 1. Noncontact trapping of single cells using steady streaming microeddies,” *Anal. Chem.*, vol. 78, no. 15, pp. 5429–5435, 2006.
[34] V. H. Lieu, “Design, Analysis, and Translation of 3D Hydrodynamic Tweezer Microeddies,” University of Washington, 2012.
[35] B. R. Lutz, “Microeddies as microfluidic elements: Reactors and cell traps,” University of Washington, 2003.
[36] B. R. Lutz, J. Chen, and D. T. Schwartz, “Characterizing Homogeneous Chemistry Using Well-Mixed Microeddies,” *Anal. Chem.*, vol. 78, no. 5, pp. 1606–1612, 2006.
[37] B. R. Lutz, J. Chen, and D. T. Schwartz, “Microfluidics without microfabrication,” *Proc. Natl. Acad. Sci.*, vol. 100, no. 8, p. 4395, 2003.
[38] B. R. Lutz, J. Chen, and D. T. Schwartz, “Microscopic steady streaming eddies created around short cylinders in a channel: Flow visualization and Stokes layer scaling,” *Phys. Fluids*, vol. 17, p. 023601, 2005.
[39] J. Chen, “Chemistry and physics in low Reynolds number micro steady streaming devices,” University of Washington, 2006.
[40] A. Hashmi, G. Yu, M. Reilly-Collette, G. Heiman, and J. Xu, “Oscillating bubbles: a versatile tool for lab on a chip applications.,” *Lab Chip*, vol. 12, no. 21, pp. 4216–27, Dec. 2012.
[41] C. Wang, B. Rallabandi, and S. Hilgenfeldt, “Frequency dependence and frequency control of microbubble streaming flows,” *Phys. Fluids*, vol. 25, no. 2, p. 022002, Feb. 2013.
[42] V. H. Lieu, T. A. House, and D. T. Schwartz, “Hydrodynamic tweezers: impact of design geometry on flow and microparticle trapping,” *Anal. Chem.*, vol. 84, no. 4, pp. 1963–8, Feb. 2012.
[43] S. K. Chung and S. K. Cho, “On-chip manipulation of objects using mobile oscillating bubbles,” *J. Micromechanics Microengineering*, vol. 18, no. 12, p. 125024, Dec. 2008.
[44] Y. Xie, D. Ahmed, M. I. Lapsley, M. Lu, S. Li, and T. J. Huang, “Acoustofluidic Relay: Sequential Trapping and Transporting of Microparticles via Acoustically Excited Oscillating Bubbles.,” *J. Lab. Autom.*, p. 2211068213485748–, Apr. 2013.
[45] N. Riley, “Steady streaming,” *Annu. Rev. Fluid Mech.*, vol. 33, pp. 43–65, 2001.
[46] C.-Y. Wang, “On high-frequency oscillatory viscous flows,” *J. Fluid Mech.*, vol. 32, no. 1, pp. 55–68, 1968.
[47] Lord Rayleigh, *Theory of Sound: Volume 1*. Macmillan and Co., 1894.
[48] H. Schlichting and K. Gersten, *Boundary-Layer Theory*. Springer, 2000.
[49] P. J. Westervelt, “Acoustic Streaming near a Small Obstacle,” *J. Acoust. Soc. Am.*, vol. 25, no. 6, p. 1123, 1953.
[50] J. Holtsmark, I. Johnsen, T. Sikkeland, and S. Skavlem, “Boundary layer flow near a cylindrical obstacle in an oscillating, incompressible fluid,” *J. Acoust. Soc. Am.*, vol. 26, no. I, pp. 26–39, 1954.
[51] W. Raney, J. Corelli, and P. Westervelt, “Acoustical streaming in the vicinity of a cylinder,” *J. Acoust.*, vol. 445, no. 1931, pp. 1006–1014, 1954.
[52] A. Bertelsen, A. Svardal, and S. Tjøtta, “Nonlinear streaming effects associated with oscillating cylinders,” *J. Fluid Mech.*, vol. 59, no. 03, pp. 493–511, Mar. 1973.
[53] W. L. Nyborg, “Acoustic Streaming near a Boundary,” *J. Acoust. Soc. Am.*, vol. 30, no. 4, pp. 329–339, 1958.
[54] C.-F. Chang and W. R. Schowalter, “Secondary flow in the neighborhood of a cylinder oscillating in a viscoelastic fluid,” *J. Nonnewton. Fluid Mech.*, vol. 6, pp. 47–67, 1979.

[55] A. F. Bertelsen, "An experimental investigation of low Reynolds number secondary streaming effects associated with an oscillating viscous flow in a curved pipe," *J. Fluid Mech.*, vol. 70, no. 03, pp. 519–527, Mar. 1975.
[56] N. Riley, "The Steady Streaming Induced by a Vibrating Cylinder," *J. Fluid Mech.*, vol. 68, no. 4, pp. 801–812, 1975.
[57] M. Tatsuno, "Circulatory Streaming in the Vicinity of an Oscillating Square Cylinder.PDF," *J. Phys. Soc. Japan*, vol. 36, no. 4, pp. 1185–1191, 1974.
[58] N. Matsunaga, A. Kaneko, and H. Honji, "A numerical study of steady streamings in oscillatory flow over a wavy wall," *J. Hydraul. Res.*, vol. 19, no. 1, pp. 29–42, 1981.
[59] P. Duck and F. Smith, "Steady streaming induced between oscillating cylinders," *J. Fluid Mech.*, vol. 91, no. 1, pp. 93–110, 1979.
[60] L. Engevik and A. Svardal, "The Invariance of the Mean Lagrangian Velocity," *J. Sound Vib.*, vol. 38, no. 4, pp. 510–511, 1975.
[61] S. Skavlem and S. Tjötta, "Steady rotational flow of an incompressible, viscous fluid enclosed between two coaxial cylinders," *J. Acoust. Soc. Am.*, vol. 27, no. 1953, pp. 951–953, 1955.
[62] G. G. Stokes, "On the theory of oscillatory waves," *Trans. Cambridge Philos. Soc.*, vol. 8, p. 441, 1847.
[63] H. Lamb, *Hydrodynamics*, 6th ed. Dover, 1945.
[64] G. K. Batchelor, *An Introduction to Fluid Dynamics*, 1st ed. Cambridge University Press, 1973.
[65] R. B. Bird, W. E. Stewart, and E. N. Lightfoot, *Transport Phenomena*, 2nd ed. Wiley, 2002.
[66] L. D. Landau and E. M. Lifshitz, *Fluid mechanics*, 1st ed. Pergamon Press, 1959.
[67] W. J. Pierson, "Perturbation analysis of the Navier-Stokes equations in Lagrangian form with selected linear solutions," *J. Geophys. Res.*, vol. 67, no. 8, pp. 3151–3160, Jul. 1962.
[68] J. C. McWilliams and J. M. Restrepo, "The Wave-Driven Ocean Circulation," *J. Phys. Oceanogr.*, vol. 29, no. 10, pp. 2523–2540, Oct. 1999.
[69] M. S. Longuet-Higgins, "Mass Transport in Water Waves," *Philos. Trans. R. Soc. A Math. Phys. Eng. Sci.*, vol. 245, no. 903, pp. 535–581, Mar. 1953.
[70] M. S. Longuet-Higgins, "On the transport of mass by time-varying ocean currents," *Deep. Res.*, vol. 16, pp. 431–447, 1969.
[71] J. T. F. Zimmerman, "On the Euler-Lagrange transformation and the stokes' drift in the presence of oscillatory and residual currents," *Deep Sea Res. Part A. Oceanogr. Res. Pap.*, vol. 26, no. 5, pp. 505–520, May 1979.
[72] I. Eames and M. McIntyre, "On the connection between Stokes drift and Darwin drift," *Math. Proc. Cambridge Philos. Soc.*, vol. 126, no. 01, pp. 171–174, 1999.
[73] M. S. Longuet-Higgins, "Eulerian and Lagrangian aspects of surface waves," *J. Fluid Mech*, vol. 173, pp. 683–707, 1986.
[74] E. Larrieu, E. J. Hinch, and F. Charru, "Lagrangian drift near a wavy boundary in a viscous oscillating flow," *J. Fluid Mech.*, vol. 630, p. 391, Jun. 2009.
[75] T. Garrison, *Oceanography: An Invitation to Marine Sciences*. Brooks/Cole, 2010.
[76] F. B. Hildebrand, *Advanced calculus for applications*, 2nd ed. Prentice-Hall Englewood Cliffs, NJ, 1962, p. 354.
[77] I. Eames, "Settling of Particles beneath Water Waves," *J. Phys. Oceanogr.*, vol. 38, no. 12, pp. 2846–2853, Dec. 2008.
[78] F. Santamaria, G. Boffetta, M. Martins Afonso, A. Mazzino, M. Onorato, and D. Pugliese, "Stokes drift for inertial particles transported by water waves," *EPL (Europhysics Lett.*, vol. 102, no. 1, p. 14003, Apr. 2013.
[79] J. Ruiz, C. García, and J. Rodríguez, "Sedimentation loss of phytoplankton cells from the mixed layer: effects of turbulence levels," *J. Plankton Res.*, vol. 18, no. 9, pp. 1727–1734, 1996.
[80] M. R. Maxey and J. J. Riley, "Equation of motion for a small rigid sphere in a nonuniform flow," *Phys. Fluids*, vol. 26, no. 4, p. 883, 1983.
[81] P. G. Saffman, "The lift on a small sphere in a slow shear flow," *J. Fluid Mech.*, vol. 22, no. 02, pp. 385–400, Mar. 1965.
[82] K. Tio and A. L. An, "On the dynamics of buoyant and heavy particles in a periodic Stuart vortex flow," *J. Fluid ...*, pp. 671–699, 1993.
[83] J. Lasheras and K. Tio, "Dynamics of a small spherical particle in steady two-dimensional vortex flows," *Appl. Mech. Rev.*, vol. 47, no. 6, part 2, pp. S61–69, 1994.

[84] J. Leach, H. Mushfique, S. Keen, R. Di Leonardo, G. Ruocco, J. Cooper, and M. Padgett, "Comparison of Faxén's correction for a microsphere translating or rotating near a surface," *Phys. Rev. E*, vol. 79, no. 2, p. 026301, Feb. 2009.
[85] A. J. Dorgan and E. Loth, "Efficient calculation of the history force at finite Reynolds numbers," *Int. J. Multiph. Flow*, vol. 33, no. 8, pp. 833–848, Aug. 2007.
[86] O. A. Druzhinin and L. A. Ostrovsky, "The influence of Basset force on particle dynamics in two-dimensional flows," *Phys. D Nonlinear Phenom.*, vol. 76, no. 1–3, pp. 34–43, Sep. 1994.
[87] E. E. Michaelides, "A novel way of computing the Basset term in unsteady multiphase flow computations," *Phys. Fluids A Fluid Dyn.*, vol. 4, no. 7, p. 1579, 1992.
[88] D. Vojir and E. Michaelides, "Effect of the history term on the motion of rigid spheres in a viscous fluid," *Int. J. Multiph. flow*, vol. 20, no. 3, pp. 547–556, 1994.
[89] J. Bowman and D. Schwartz, "High Peclet number mass transfer in the acoustic streaming flow between two concentric cylinders," *J. Heat Mass Transf.*, vol. 41, pp. 1065–1074, 1998.
[90] H. Kumar, M. H. Tawhai, E. a Hoffman, and C.-L. Lin, "Steady streaming: A key mixing mechanism in low-Reynolds-number acinar flows.," *Phys. Fluids (1994).*, vol. 23, no. 4, p. 41902, Apr. 2011.
[91] A. T. Hjelmfelt and L. F. Mockros, "Motion of discrete particles in a turbulent fluid," *Appl. Sci. Res.*, vol. 2900, no. 206, pp. 149–161, 1966.
[92] R. Mei, "Velocity fidelity of flow tracer particles," *Exp. Fluids*, vol. 22, no. 1, pp. 1–13, 1996.
[93] J. Medina and D. Schwartz, "Nonlinear dynamics of modulated flow between a porous injector and an impermeable substrate," *Phys. Fluids*, vol. 8, no. November, pp. 2895–2905, 1996.
[94] D. Schwartz, "Measurements of steady axial streaming at a rotating disc with torsional oscillations," *Proc. R. Soc. Math. Phys. Sci.*, vol. 442, no. 1915, pp. 397–407, 1993.
[95] K. Chong, S. D. Kelly, S. Smith, and J. D. Eldredge, "Inertial particle trapping in viscous streaming," *Phys. Fluids*, vol. 25, no. 3, p. 033602, Mar. 2013.
[96] A. Schaap, T. Rohrlack, and Y. Bellouard, "Lab on a chip technologies for algae detection: a review.," *J. Biophotonics*, vol. 5, pp. 661–672, Jul. 2012.
[97] N. Riley, "Oscillatory viscous flows. Review and extension," *J. Inst. Math. its Appl.*, vol. 3, pp. 419–434, 1967.
[98] P. J. Westervelt, "The Theory of Steady Rotational Flow Generated by a Sound Field," *J. Acoust. Soc. Am.*, vol. 25, no. 1, pp. 60–67, 1953.
[99] C. A. Lane, "Acoustical Streaming in the Vicinity of a Sphere," *J. Acoust. Soc. Am.*, vol. 27, no. 6, pp. 1082–1086, 1955.
[100] M. S. Longuet-Higgins, "Viscous streaming from an oscillating spherical bubble," *Proc. R. Soc. A Math. Phys. Eng. Sci.*, vol. 454, pp. 725–742, 1998.
[101] P. Tanga and a. Provenzale, "Dynamics of advected tracers with varying buoyancy," *Phys. D Nonlinear Phenom.*, vol. 76, no. 1–3, pp. 202–215, Sep. 1994.
[102] S.-J. Liu, H.-H. Wei, S.-H. Hwang, and H.-C. Chang, "Dynamic particle trapping, release, and sorting by microvortices on a substrate," *Phys. Rev. E*, vol. 82, no. 2, p. 026308, Aug. 2010.
[103] C. M. Lin, Y. S. Lai, H. P. Liu, C. Y. Chen, and A. M. Wo, "Trapping of bioparticles via microvortices in a microfluidic device for bioassay applications.," *Anal. Chem.*, vol. 80, no. 23, pp. 8937–45, Dec. 2008.

APPENDIX || GEOMETRY MESHING AND CONVERGENCE

Overview of meshing methods

The goal of meshing is to provide a grid of elements over which the governing equations are solved. A finer, more detailed mesh provides a higher level of accuracy, and is in some cases necessary to even find a convergent solution. Here, different methods of meshing are shown, along with an evaluation of errors. A "good" mesh is considered one that provides a convergent solution that is mesh-independent at the level of accuracy required while balancing computation time and memory load. As a first approach, the number of elements can simply be increased until the solution no longer changes upon further mesh refinement as in Figure 47. For all the following figures, Top plot shows the mesh generated, the bottom plot shows the resulting steady stream contours.

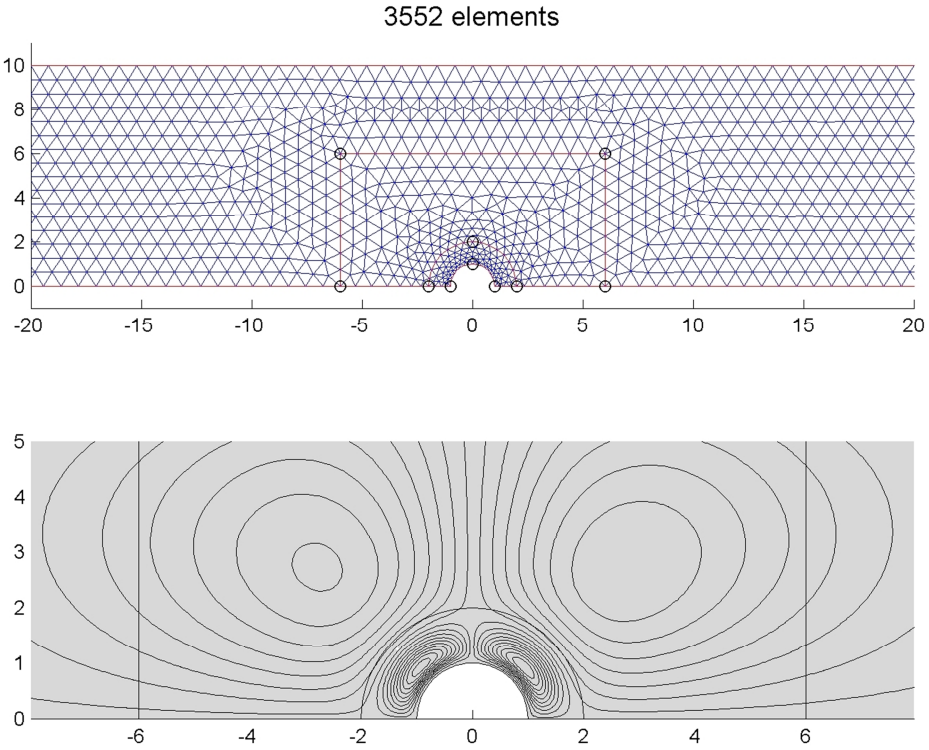

Figure 47. Nonspecific meshing by changing coarseness setting. Top plot shows the mesh generated, the bottom plot shows the resulting steady stream contours.

Subdomains may be defined that do not change the underlying physics but allow for specific control over where meshing should be finer or coarser as in Figure 48 and Figure 49. As can be seen from Figure 48, a finer outer mesh is undesirable because the strong gradients generated by the forces in the fluid are adjacent to obstructions and these physics are not captured unless a fine interior mesh is used.

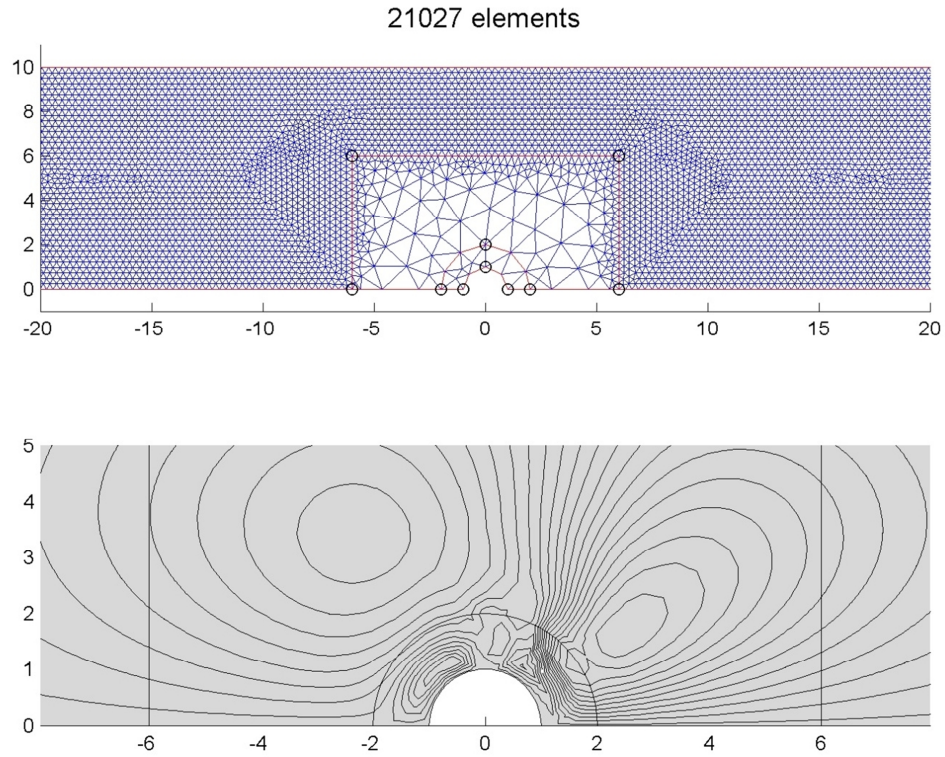

Figure 48. Exterior subdomain refinement. Notice the resulting computation has produced an unacceptable a.

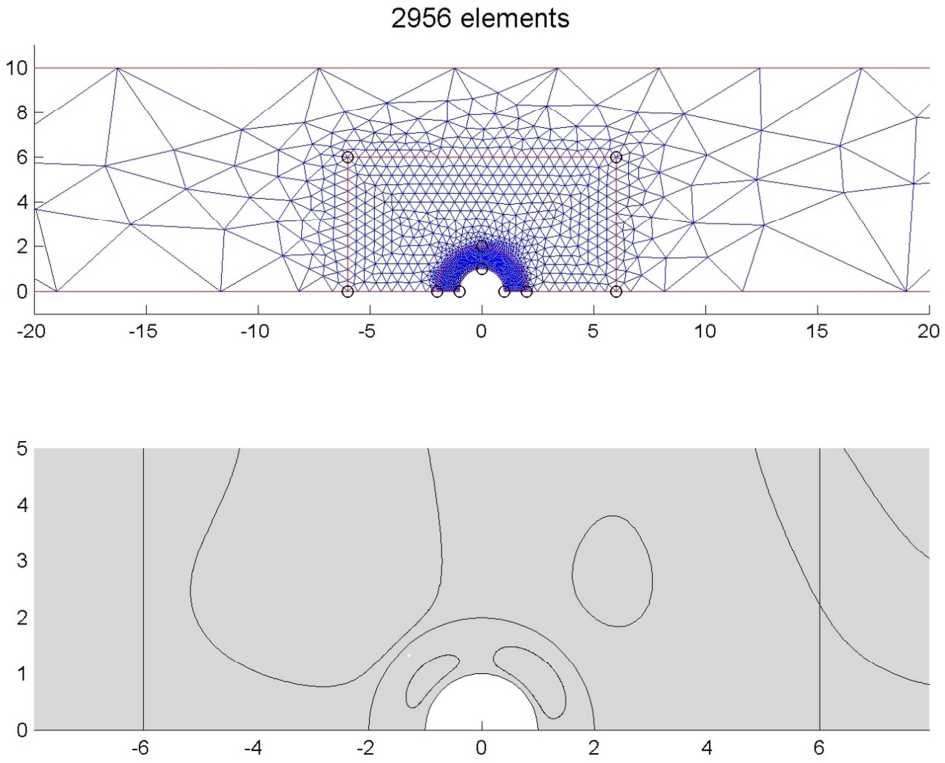

Figure 49. Interior subdomain meshing. The computation result is still not converged to a desirable point. More elements are needed.

In Figure 50, boundary element meshing is shown. As can be seen, meshing the boundaries produces fine details at the gradient sources, but fails to capture how these gradients propogate throughout the rest of the interior system.

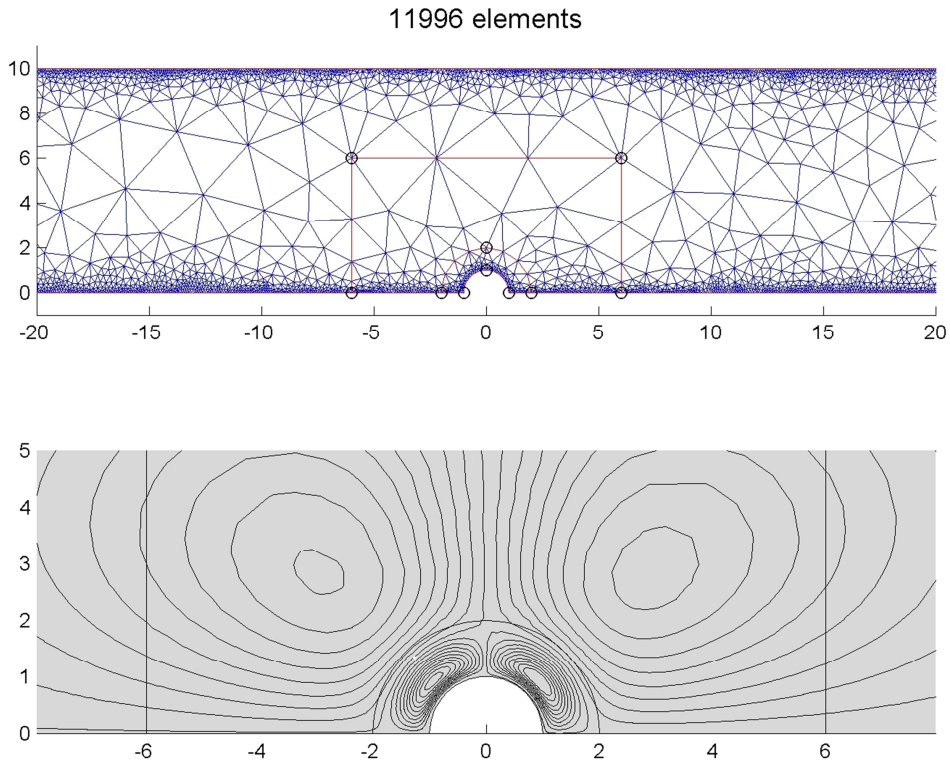

Figure 50. Typical boundary mesh refinement. Interior areas are not refined enough, as evidenced by a lack of symmetry in the outer eddy flows.

In Figure 51, a final composite mesh is shown. Here, boundaries and specific subdomains are refined to a desirable level. The resulting computation produces contours as expected, with no smooth transitions and a symmetrical appearance. For all of the simulations discussed in this research, this type of composite mesh refinement is utilized as it allows for computations that are no longer dependent on the level of mesh refinement, thus producing a truly converged solution. To further quantify these types of errors, some basic error analysis has been performed on each type of meshing to determine, in general, the minimum level of refinement needed to produce a converged solution.

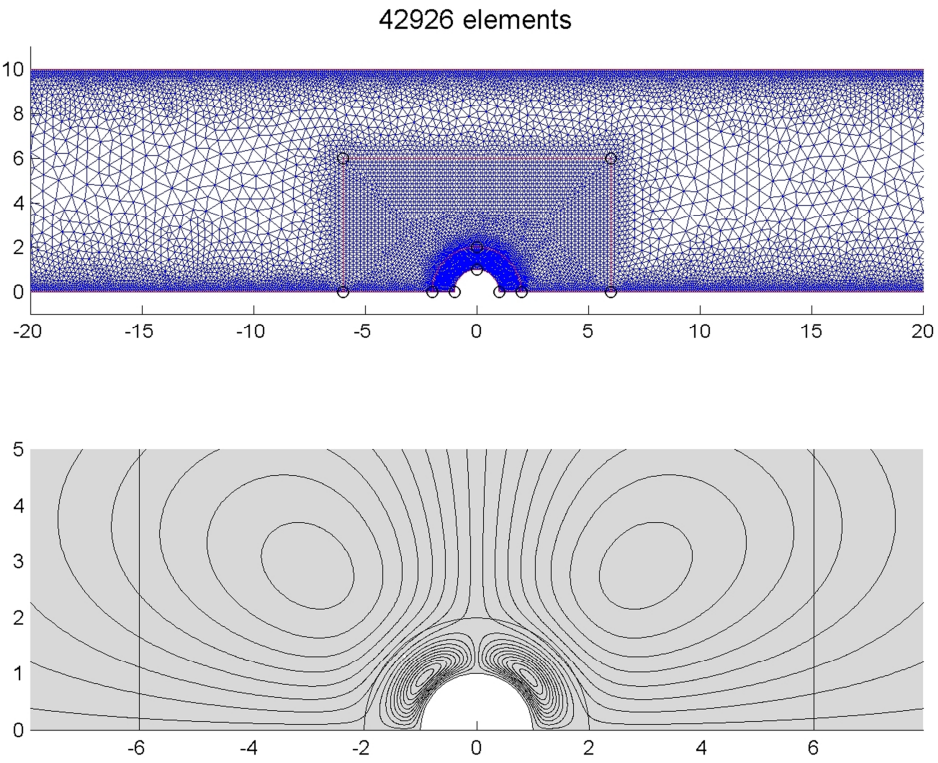

Figure 51. Boundary and subdomain mesh refinement. Note the symmetrical eddy appearance, smooth transitions and lack of jaggedness in the contour lines.

Relative error in computed solutions

To quantify the error of any given mesh refinement, simple metrics were devised. The first metric calculates the flux through the system from the left, and the flux through the system through the right. Figure 52 shows a simple schematic of this metric. The difference between the left and right side fluxes is expected to be zero, because there is no accumulation or depletion of material defined in our governing equations. Any value other than zero is deemed to be an error due to mesh refinement.

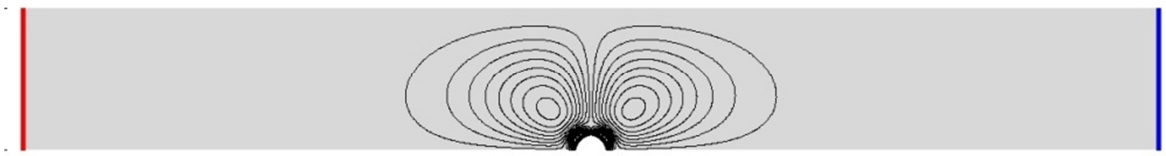

Figure 52. Line integrals at inlet and outlet of channel used to determine net flux into or out-of system. The expected quantity is zero.

In Figure 53, errors for a range of meshing techniques and a range of total element numbers is shown. Errors for all meshing techniques approached the minimum as the total number of elements moved into the the thousands, with the tens of thousands being prefered. Because this metric focuses on errors that are actually far away from the interesting parts of the flow, another metric was developed that more closely measures the errors in the vicinity of the streaming flow.

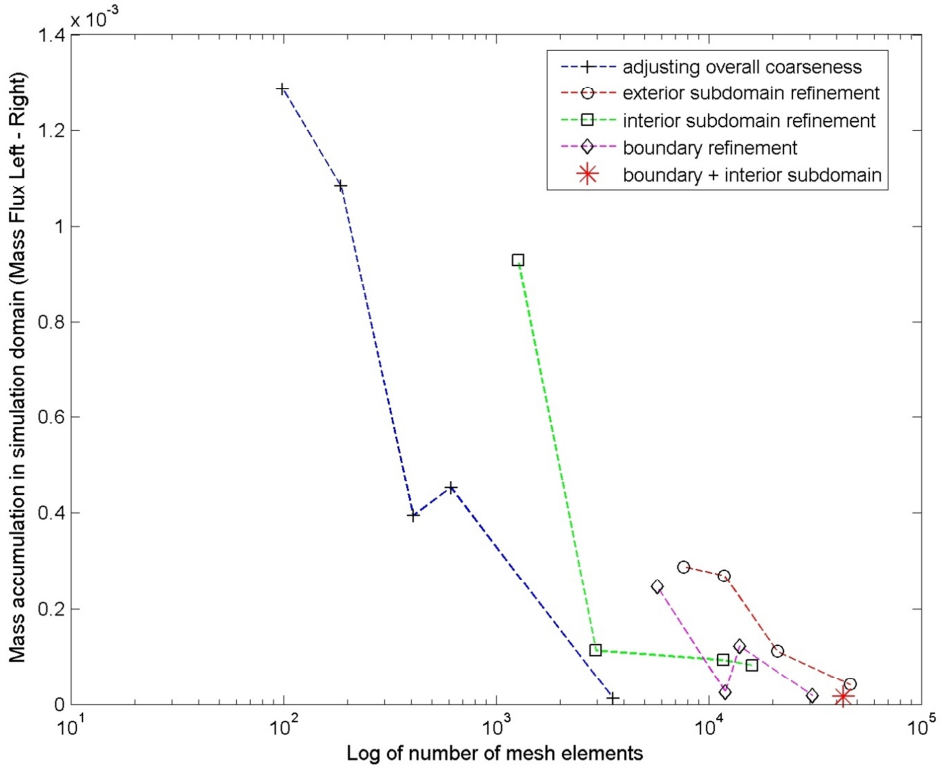

Figure 53. Estimating error due to mesh refinement based on total net flux into/out-of system.

The second mesh error metric computes a line integral at the vertical line of symmetry that splits the left from the right sets of streaming eddies, as shown in Figure 54. As none of the contours cross this boundary, we expect the overall flux across line to be zero.

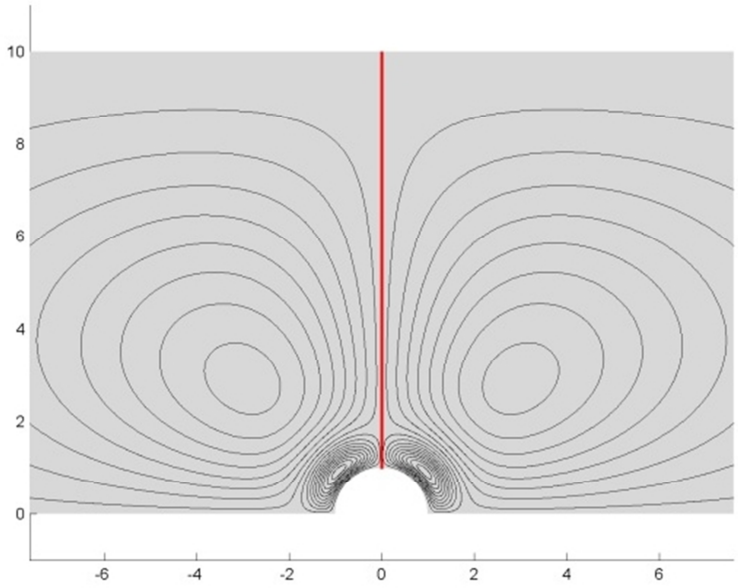

Figure 54. Line integral across vertical line of symmetry used to estimate total computation error. The expected quantity is zero.

As before, the errors for the same mesh samples were computed as shown in Figure 55. Here, a few interesting things are evident. First, by only refining the boundaries, flow through the channel is poorly computed. Second, the overall absolute error drops only for a combination of all the described techniques; that is, defining subdomains and choosing optimum mesh refinement at the boundary and subdomain level. Here, the best mesh generated used around 40,000 elements. It should be noted that in general, more elements means a better mesh. However, memory constraints limit the number of elements in a given simulation.

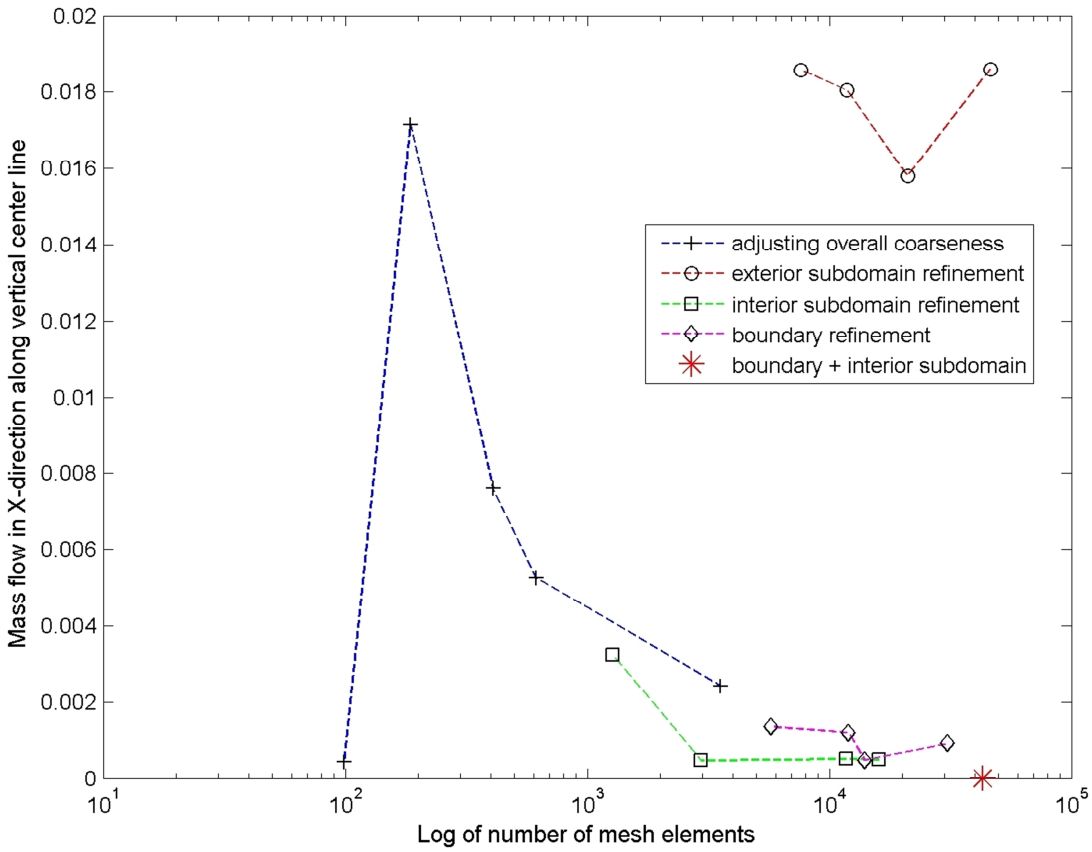

Figure 55. Estimating error due to mesh refinement based on net flux across line of vertical symmetry.